

STRANGE QUARK SUPPRESSION IN 225 GEV/C PI-MINUS
BERYLLIUM INTERACTIONS

BY

PAUL V. SCHOESSOW

B. S., University of Wisconsin-Milwaukee, 1976
M. S., University of Illinois, 1979

THESIS

Submitted in partial fulfillment of the requirements
for the degree of Doctor of Philosophy in Physics
in the Graduate College of the
University of Illinois at Urbana-Champaign, 1983

Urbana, Illinois

PACS 13.90.+i

STRANGE QUARK SUPPRESSION IN 225 GEV/C PI-MINUS
BERYLLIUM INTERACTIONS

Paul V. Schoessow, Ph.D.
Department of Physics
University of Illinois at Urbana-Champaign, 1983

The Chicago Cyclotron Magnet Spectrometer at Fermilab was used to study the production of $\omega(783)$ and $\phi(1020)$ mesons in 225 GeV/c π^- Be interactions via their decays into $\mu^+\mu^-$. Based on the observed ϕ/ω production ratio, the strange quark suppression factor λ was determined to be 0.31 ± 0.05 , in good agreement with a world average of about 0.29.

ACKNOWLEDGEMENTS

I would like to thank my advisor, Prof. Robert D. Sard, for all his assistance during my years at Illinois and especially in the preparation of this thesis. It is difficult to fully express the debt of gratitude which I owe him.

Dr. John W. Cooper has been a constant source of encouragement and enlightenment to me throughout the course of my graduate studies.

Steve Hahn and Howard Budd, my fellow graduate students, contributed in large part to the success of this undertaking.

I am grateful to Dr. Lorella Jones, for many useful discussions on the finer points of high energy theory.

I would like to thank the highly competent support personnel of the U of I high energy physics group, in particular our computer experts Jerry Wray, Dave Lesny, and Keith Nater; and our secretaries, Dorothy Schoeps, Wynemia Wood, and Jeannine Adomaitis.

My wife, Trish, was a major factor in making graduate school a pleasant experience.

[REDACTED]

The work presented in this thesis was supported in part by the people of the United States, through the U.S. Department of Energy under grant DE-AC02-76ER01195.

TABLE OF CONTENTS

1.	INTRODUCTION.....	1
2.	APPARATUS.....	4
2.1	Introduction.....	4
2.2	The Analysis Magnet.....	4
2.3	Beamline and Target.....	6
2.4	The Multiwire Proportional Chambers...	7
2.5	Drift Chambers.....	9
2.6	Hodoscopes.....	13
2.7	Lead Glass.....	18
2.8	The Cherenkov Counter.....	18
2.9	The Main Event Trigger.....	18
2.10	Data Logging.....	21
3.	PRELIMINARY DATA REDUCTION.....	22
3.1	Introduction.....	22
3.2	Upstream Track Reconstruction.....	23
3.3	Tracks in the CCM.....	25
3.4	The Drift Chamber Vernier.....	27
3.5	Trackfitting.....	29
3.6	Extracting the Dimuon Sample.....	32

4.	THEORY AND PHENOMENOLOGY.....	35
4.1	Quarks and Hadron Spectroscopy.....	35
4.2	Quark Dynamics.....	41
4.3	Hadron Production and the Additive Quark Model.....	42
4.4	Strangeness Suppression in Other Processes.....	46
5.	FINAL DATA ANALYSIS AND RESULTS.....	47
5.1	The Dimuon Spectrum.....	47
5.2	Kaon Identification and the $K^+ K^-$ Spectrum.....	56
5.3	Acceptances.....	58
5.4	Search for the $f'(1515)$	62
5.5	Measurement of λ	67
6.	DISCUSSION AND CONCLUSIONS.....	73
	APPENDICES.....	79
A.	The Cherenkov Counter.....	79
A.1	Introduction.....	79
A.2	The E610 Cherenkov Counter.....	80
A.3	Alignment and Calibration.....	86
B.	Neutral Strange Particles.....	93
B.1	Trackfinding.....	93
B.2	Neutral Vee Reconstruction.....	94

B.3	Efficiencies and Yields.....	100
B.4	K_S^0 and Λ Lifetimes.....	104
C.	The Charged-Kaon Trigger.....	108
D.	ρ^0 - ω Interference.....	112
	REFERENCES.....	117
	VITA.....	119

CHAPTER 1

INTRODUCTION

This report is based on data from Fermilab experiment 610 taken during the spring months of 1980. The E610 collaboration consisted of physicists from the University of Illinois, the University of Pennsylvania, Fermilab, Purdue University, and Tufts University, with T. B. W. Kirk of Fermilab as spokesman.

The main purpose of the experiment was the study of particles (photons in particular) produced in association with the $\Psi(3098)$, with the Ψ detected via its decay into $\mu^+\mu^-$. Thus, the presence of a dimuon pair was required by the main event trigger. Detection of additional particles necessitated the use of an open geometry configuration for the spectrometer, which had the additional advantage of giving a much better dimuon mass resolution compared to the closed geometry ("beam dump") systems ordinarily employed in studies of Ψ production using the $\mu^+\mu^-$ decay channel.

The trigger was biased towards accepting dimuon pairs with a large proper mass. Nevertheless, the spectrometer did have some acceptance for lower mass dimuons, and it is an investigation of this region of the spectrum that is the subject of this thesis. A

discussion of the Ψ physics is found in the three other theses from E610 (Hahn, 1983; Budd, 1983; Hossain, 1981).

Of particular interest in the low mass region are the $\omega(783)$ and $\phi(1020)$ mesons. Unlike closed geometry experiments, this experiment had small enough mass resolution to permit separation of the ω contribution from that of any $\rho^0(769)$ present.

The extent of the breaking of exact SU(3) symmetry in the hadron spectrum is specified by a phenomenological parameter, the strangeness suppression constant λ (Anisovich and Shekhter, 1973). This has been measured in a variety of processes, which all give nearly the same value for λ of about 0.29. We present here the first measurement of this constant using a comparison of the relative production of ω and ϕ .

A word is perhaps in order here about the serendipitous nature of scientific research. The possibility of studying the physics of the ω and ϕ from the dimuon sample was not even suspected at the time when the experiment was proposed.

Another feature of the spectrometer is the multicell Cherenkov counter, used for π -K discrimination. A limited amount of data was taken with a test trigger incorporating the Cherenkov counter. This trigger was biased towards final states containing a $K^+ K^-$ pair.

In this sample we observed $\phi \Rightarrow K^+ K^-$ decays. A search for the $f'(1515) \Rightarrow K^+ K^-$ was performed, and the results compared with theoretical estimates of its rate of production relative to the ϕ .

CHAPTER 2

APPARATUS

2.1 Introduction

The E610 spectrometer (figure 2.1) was designed to study particles produced in association with high-mass dimuon pairs. The various subsystems which accomplish these functions are described in this chapter.

In order to avoid unnecessary duplication of effort, the discussion of most of the spectrometer components will be brief if more detailed descriptions exist elsewhere. In this case the appropriate references will be given.

2.2 The Analysis Magnet

The Chicago Cyclotron Magnet (CCM) is the dominant feature of the apparatus. With a pole face diameter of 4.32m and a gap of 1.29m, the CCM is to a great extent responsible for the large acceptance of the spectrometer. The magnet was operated at a current of 4200A, corresponding to a field strength at the center of 1.42T. For most purposes, the "hardedge" approximation-- a uniform field out to a

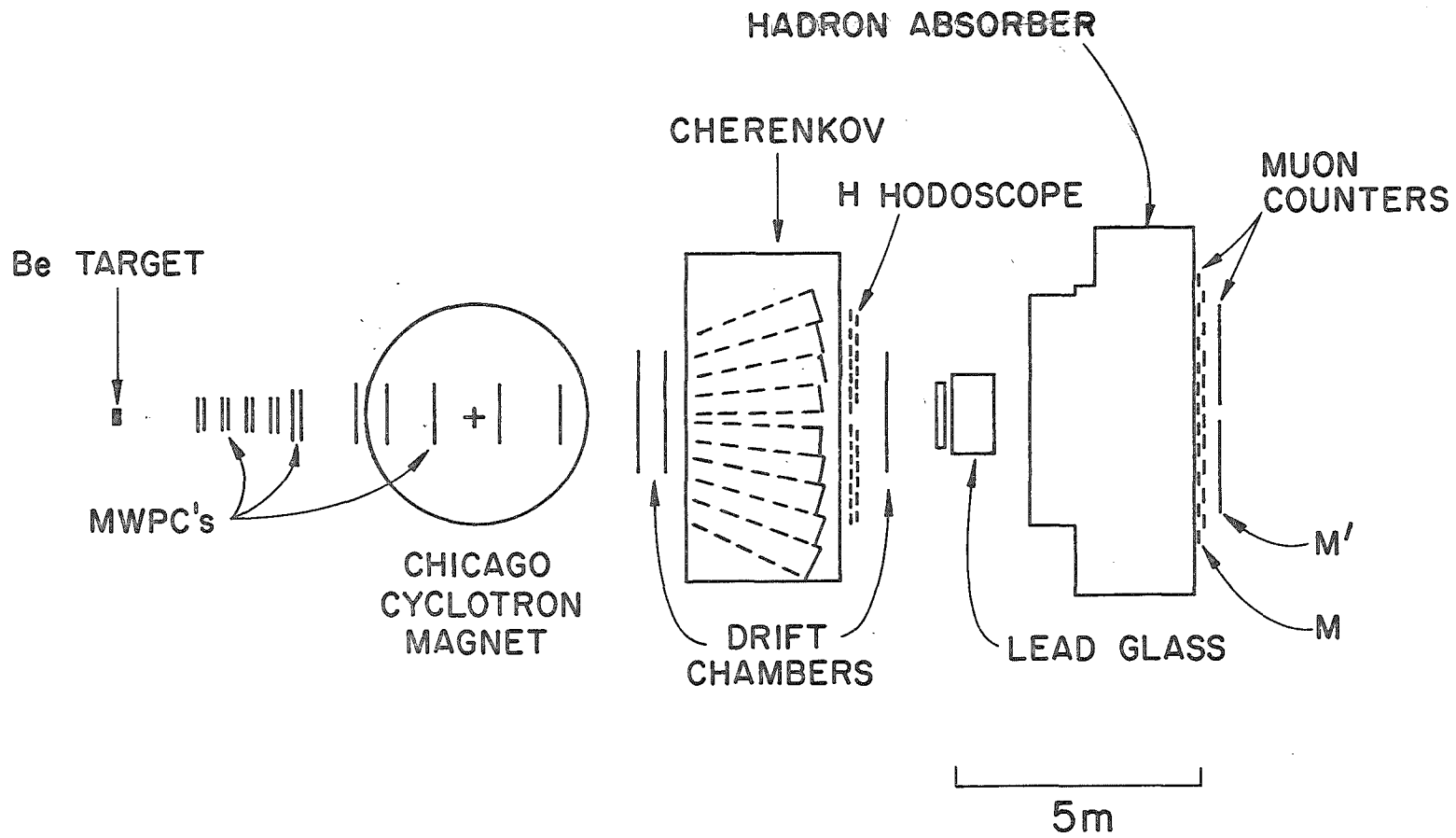


Figure 2.1. The E610 spectrometer.

certain radius, zero beyond— could be used, with the radius of the field equal to 2.46m. The p_{\perp} kick of the magnet for this field was approximately 2.1 GeV/c.

The center of the magnet served as the origin of the (right-handed) lab Cartesian coordinate system. The z axis (beam line, "project north") was positive downstream of the CCM. The x axis ("west") was perpendicular to the axis of the magnet, whose polarity was such that negatively charged particles bent towards -x. The y axis was then vertical and positive upward. In the homogeneous part of the magnetic field the bending was in the x-z plane (x view). To a first approximation the y-z projection of the orbit (y view) was a straight line through the point of origin.

2.3 Beamline and Target

The pion beam was produced by the interactions of main ring protons in a production target 900m upstream of the muon lab. The beam transport system consisted of the magnets used to bring the pions into the lab, as well as perform the final selection of the beam momentum (225 GeV/c). By means of six multiwire proportional chamber (MWPC) planes and six beam hodoscopes, the momentum and orbit of the incident beam particle could be measured. The beam momentum spread

was ± 1 GeV/c, with a width (at the target midplane) of ± 1.4 cm in x, and ± 0.9 cm in y. Details of this system and a discussion of the algorithms used to reconstruct beam tracks can be found in the theses of H. Budd (Budd, 1983), and S. Hossain (Hossain, 1981).

The target consisted of a 3" thick slab of beryllium, located 741cm upstream of the center of the CCM. Three scintillation counters, one immediately upstream (T0) and two immediately downstream (T1, T2) of the target, were used as part of the trigger to determine whether the incident particle had interacted in the beryllium.

2.4 The Multiwire Proportional Chambers

Position information on secondary tracks was provided upstream of and in the magnet by two sets of MWPCs. The so-called 80 cm chambers (10 planes) measured tracks before entering the CCM field, the U of I chambers (15 planes) inside the volume of the field.

The 80 cm chambers, as the name suggests, had an active area of 80 cm x 80 cm. Each of the five chambers contained two parallel sense planes with perpendicular wires, with a wire spacing of 1.59mm. Four of the chambers were used to measure x and y, while the fifth was physically tilted at 45° to facilitate x-y matching of the upstream tracks. Thus there were four x-planes, four y-planes, one u-plane,

and one v-plane. (In chamber jargon, planes are specified by the coordinate measured. Planes whose wires are not parallel to either the x or y axes are denoted u or v.)

These chambers were originally built by R. Hicks and E. Smith at the University of Illinois for the E398 muon experiment. Before their installation in the E610 spectrometer, they were rebuilt at Fermilab by R. Krull. Particulars of the construction and readout electronics of the 80 cm chambers are found in the thesis of R. Hicks (Hicks, 1978).

The five chambers in the magnet, designated U of I, were constructed at the University of Illinois by H. Budd, P. Lukens, and U. Kruse specifically for this experiment. Covering an active area of 120cm x 100cm, the three anode planes (u, y, v) in each chamber had their wires tilted at $+11^\circ$, 90° , -11° with respect to the vertical. The wire spacing for these planes was 2mm. The most upstream of the chambers was so near the edge of the CCM field (figure 2.1) that particles reaching it did not suffer appreciable deflection. For a more detailed description of the U of I chambers see Budd (1983).

2.5 Drift Chambers

The E610 drift chambers were built by the Fermilab Neutrino Department technical staff under the direction of T. Kirk. Their original purpose was to provide sufficient position information to reconstruct charged tracks in the region downstream of the CCM, independently of the upstream chambers. Because of difficulties with the readout, however, the ultimate use of the drift chambers was as a momentum vernier on tracks already found using the 80 cm and U of I MWPCs. The vernier algorithm will be described in chapter 3; for now, the discussion will be limited to the physical configuration and principles of operation of the drift chambers.

Each chamber had an active area of 2.4m x 1.2m. Four chambers were built, but the chamber installed farthest downstream would not hold high voltage and was never used.

The drift chambers were designed by Muzzafar Atac at Fermilab (Atac, 1977; 1978). The novel feature of these chambers was their bi-dimensional readout capability, in which both x and y information is provided by a single plane. Each chamber consisted of 60 drift cells, 4cm in width. Figure 2.2 depicts one such cell. At the center of each cell is a two sided printed circuit delay line. Two anode wires are located at a distance of 2.7mm on either side of the delay line. The drift (cathode) wires and the field shaping wires give a

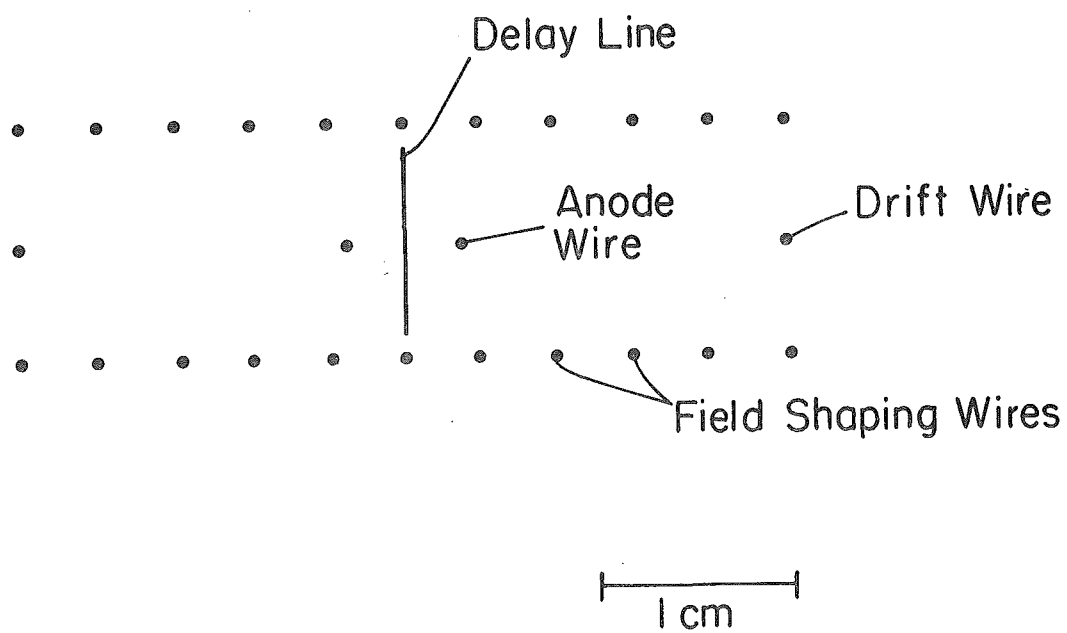


Figure 2.2. Drift cell, x-z view.

uniform electric field within the drift space.

The chambers were filled with a mixture of 50% argon and 50% ethane. The electron drift velocity was determined to be $5.95\text{cm}/\mu\text{s}$.

Upon receiving a signal from the master trigger, a clock is started, while the electrons produced by the passage of a charged particle migrate toward the nearest anode wire. The clock is stopped when an avalanche is detected at the anode, and from this time and the known drift velocity the position of the track relative to the anode is determined. In addition, the avalanche induces a pulse on the delay line. The times at which this signal reaches each of the ends of the delay line are also measured, and from the speed of propagation along the delay line (0.30cm/ns) the y position of the hit can also be determined.

The MUTES (Multihit Time Encoder System) readout for the drift chambers (Kirk, 1978) had the capability of processing four different signals from each drift cell. These were chosen to be (figure 2.3) the anode OR (A), delay line OR (O), delay line L, and delay line R. With all four signals present, both the x and y coordinates of a hit within the cell could be determined.

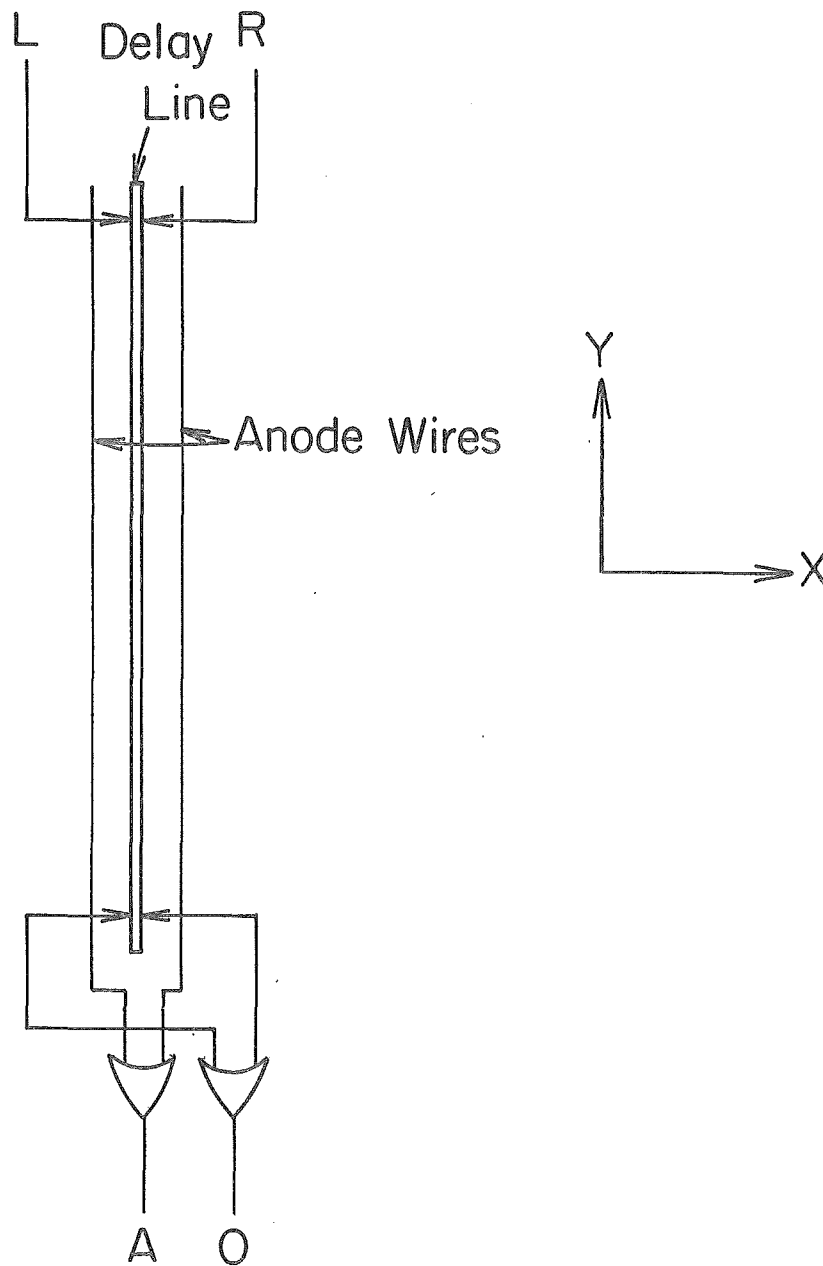


Figure 2.3. Drift cell readout (schematic).

Unfortunately, this scheme relied heavily on the presence of the delay line information. When the drift chambers were installed, however, it was discovered that ferrite cores used in the amplifier boards for the delay line signals saturated in the fringe field of the CCM. Hence only the anode OR was available from each cell. The large two- or fourfold ambiguity present (which the delay line signals were to resolve) made independent trackfinding in the drift chambers impossible, and of course no y information could be obtained.

2.6 Hodoscopes

Additional track position information was provided downstream of the CCM by three hodoscopes, denoted H, M, and M'. More importantly, the hodoscopes were an integral part of the triggers used in this experiment.

The H (hadron) hodoscope was located directly downstream of the Cherenkov counter, and was used as part of the charged-K trigger (see appendix C). It consisted of 54 elements of plastic scintillator configured as depicted in figure 2.4. (Dashed lines indicate the positions of the Cherenkov counter mirrors.) Each scintillator was viewed by an RCA 8575 photomultiplier tube. The discriminated output from every H element was read out using LRS 2228A 11 bit

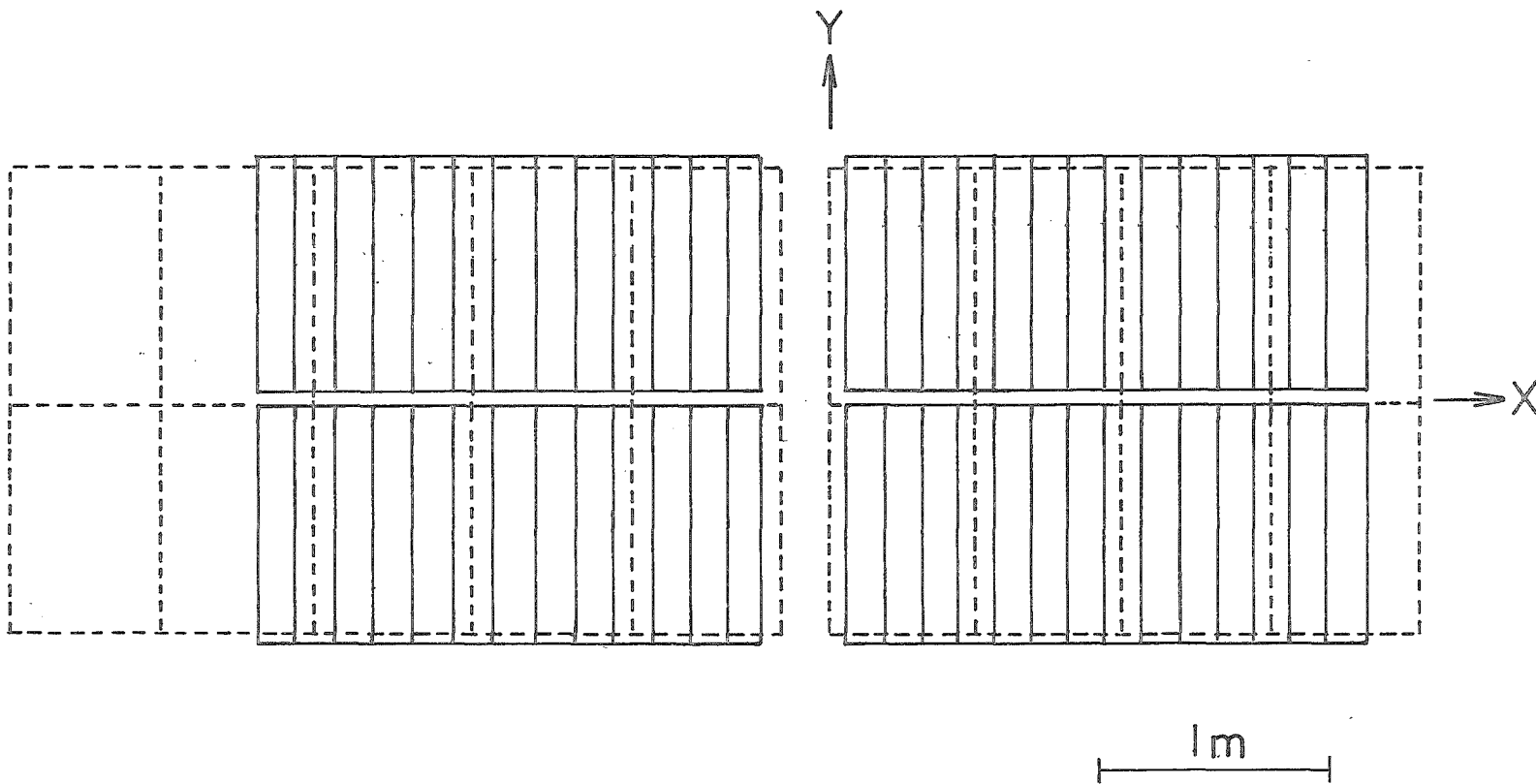


Figure 2.4. The H hodoscope. Dashed lines indicate the positions of the Cherenkov mirrors.

time-to-digital converters (TDCs).

The M (muon) hodoscope (figure 2.5) was positioned downstream of the steel hadron absorber, and was used to form the main event trigger. The "bow-tie" arrangement was designed to bias the single muon acceptance towards large p_{\perp} , in an attempt to eliminate muons from decay and hadron punch-through. Requiring two muons in opposite quadrants served to reduce the acceptance for low-mass pairs. As in the case of the H hodoscope, each element of the M (and M') was viewed by an RCA 8575 phototube. The M elements were read out using TDCs, as in the case of the H hodoscope. In addition, the M elements were latched using LRS 2341A coincidence registers, that is, the presence or absence of hits in the elements in time with the trigger was recorded, independently of the TDC information.

The M' hodoscope (figure 2.6) covered the region downstream of the steel left uncovered by the gaps in the M. Unlike the H and M, the eight M' elements were placed horizontally, thus setting limits on y rather than x. The readout was similar to the M (TDCs and latches), except that the M' was not included in the trigger.

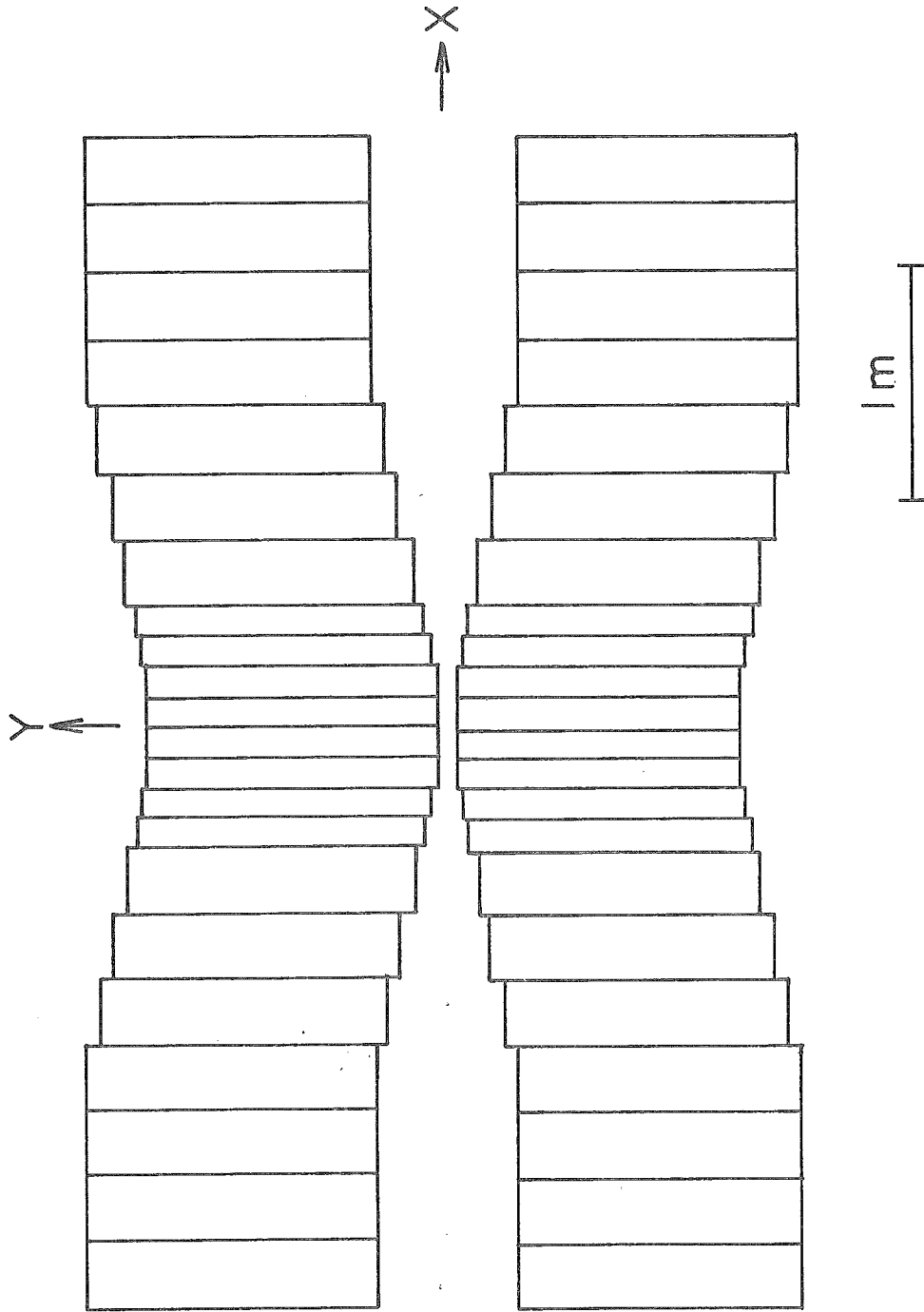


Figure 2.5. The M hodoscope.

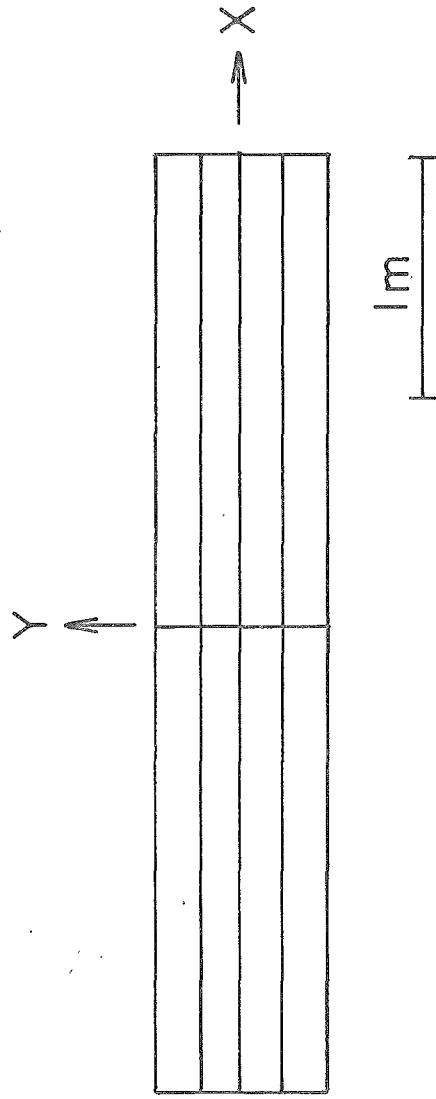


Figure 2.6. The M' hodoscope.

2.7 Lead Glass

Photons were detected by means of a lead glass-proportional tube assembly. As this part of the equipment was not used in the present analysis, the reader is referred to the thesis of S. Hahn (Hahn, 1983) for a complete description.

2.8 The Cherenkov Counter

The multicell Cherenkov counter furnished a means of discriminating between kaons and pions in the 8-21 GeV/c momentum band. The hardware and calibration aspects of the system are described in appendix A.

2.9 The Main Event Trigger

A description of the electronics used to form the dimuon trigger is found in Hahn (1983). The purpose of this section is to summarize the steps on the basis of which the decision to accept an event as a dimuon candidate is made.

The trigger was formed by requiring (in symbolic notation) (clean beam) · (interaction) · (H) · (2 μ) · (beam veto). Each of these conditions is considered separately below.

The clean beam requirement was imposed to ensure that one and only one beam particle would interact in the target within the livetime of the apparatus, and that no muons from decays-in-flight in the beamline were present to cause spurious triggers by firing the muon counters in the M hodoscope. Every beam hodoscope was required to have a single hit. If any particle incident on the apparatus from outside the beam region was detected by the veto counters, the event was rejected. Finally, no beam particles could be present in the RF buckets adjacent to the bucket containing the candidate beam particle. (The Fermilab proton synchrotron produces 400 GeV/c protons in bursts or "buckets" at a frequency of 53 MHz.)

An interaction was required in the target, based on the information from the target counters T0, T1, and T2. Each of the signals were discriminated directly (T0LO, T1LO, T2LO). The signals from the counters downstream of the target were also passed through adjustable attenuators and discriminated again (T1HI, T2HI). The attenuation on T1 and T2 was adjusted such that the rate $T0LO \cdot T1HI \cdot T2HI / T0LO \cdot T1LO \cdot T2LO$ corresponded to the fraction of interactions (~15%) expected for a 3" thickness of beryllium. With

these final attenuator settings, an interaction was defined as $T0LO \cdot T1HI \cdot T2HI$.

At least one element of the H hodoscope had to have been hit.

The event was required to have hits in opposite quadrants of the M hodoscope (2μ). Furthermore, the counters in each quadrant were successively numbered, and no more than one even and one odd numbered counter in a given quadrant could have fired. This served to discriminate against events in which a hadron shower emerged from the steel, thus giving hits in a group of adjacent M counters.

The beam veto rejected any events which had tracks leaving the steel in the beam region, by requiring that the beam veto counter (a small scintillation counter on the beamline downstream of the steel) had not fired.

In addition to the dimuon trigger, other test triggers could be formed by changing the logic. Of particular interest for this work is the "charged-K" trigger, formed by $(\text{clean beam}) \cdot (\text{interaction}) \cdot (2K)$. The 2K requirement involved the Cherenkov counter, and will be discussed in appendix C.

2.10 Data Logging

The online system consisted of a PDP 11/45 computer, with a slaved LSI 11. Upon receiving a trigger, the data was recovered from the CAMAC system and written to tape. The online program MULTI permitted the limited processing of the data (e.g. histogramming) for diagnostic purposes while data acquisition was in progress. A complete account of the online hardware and software is found in Hahn (1983).

CHAPTER 3

PRELIMINARY DATA REDUCTION

3.1 Introduction

This chapter is devoted to a description of the process by which the raw data is converted into a form useful for the final physics analysis. This involves pattern recognition and momentum determination for the secondary charged particle tracks. A discussion of the transfer of track information and unpacked data to data summary tapes (DSTs) is included.

The track reconstruction itself was divided into several stages. The intersection of the beam track with the midplane of the target was used as a crude approximation to the primary vertex, which in turn was used as input to a better vertex finding scheme.

Straight line tracks were then found in the section of the spectrometer upstream of the magnet, independently in the x-z and y-z planes. Finally, the upstream tracks were extended into the field of the CCM, and the x and y tracks were linked. More detailed accounts of the trackfinding can be found in Budd (1983) and Hossain (1981).

3.2 Upstream Track Reconstruction

The first step in trackfinding was to locate the primary vertex. A fast algorithm for finding only four-point tracks (four x- or four y-planes) in the 80 cm chambers was developed. Using pairs of hits in different planes, a road 0.4 cm wide was formed, and confirming hits sought in the remaining two planes of that view. In order to save time, no road was considered unless its extrapolated position at the target was within 5.0 cm of the intersection of the beam track with the target midplane. Once four hits were found within the road, the track was fit to a straight line, and the used hits were flagged to remove them from consideration as being associated with any subsequent track.

The mean of the intersection of all four-point tracks in a given view with the midplane of the target was then taken as the vertex position. Once the transverse coordinates of the primary vertex were determined, the trackfinding proper could proceed.

The vertex was used to convert 80 cm chamber x and y hits and U of I chamber y hits into angles formed by the straight line from the vertex to the point hit. The x and y views were processed independently. Taking the hit with the largest negative angle, a search was made in the remaining planes of that view for confirming hits within a 3.0 mr angular road. If at least two additional hits in

the y view or one in the x view were found within the road, the track was fit, including the vertex as a point on the straight track. The routine then looked at the next most negative angle, and so on until all angles had been examined.

Using all tracks found in this fashion, the vertex was recalculated. If the new vertex position deviated from the starting value by more than 4.0 mm, the vertex was assumed to be unstable, and the trackfinding was repeated using the new vertex coordinates as input.

This algorithm was chosen for its speed, but had the disadvantage that it strongly favored tracks associated with the primary vertex. This eliminated most of the tracks from neutral ν_0 decays, and so for that analysis (Appendix B), another upstream trackfinder was used which did not depend on a primary vertex position as input.

At this point we had sets of upstream tracks in the x and y views. We then proceeded to match x tracks with corresponding y tracks, and to determine the momenta and downstream track slopes and intercepts.

3.3 Tracks in the CCM

The reconstruction of bending tracks inside the field of the CCM was the most difficult aspect of trackfinding in this spectrometer. The information available for x view tracking was limited to the ten u-v MWPC planes inside the magnet gap. In addition, noise in the chambers would frequently produce "light-ups", in which large numbers of adjacent wires in one or more planes would fire. An algorithm for removing these clusters of hits was developed, which however did not always work perfectly, leaving some random noise hits behind.

As planned originally, the upstream x and y tracks were to be matched using hits in the tilted 80 cm chamber and the first U of I chamber, before any attempt was made to reconstruct the tracks through the CCM field. This idea had to be abandoned because of the low efficiency of the tilted 80 cm planes and the high level of noise remaining in the first U of I chamber even after the removal of light-ups.

Instead, all x-y track pairs were tested as possible space track candidates. For a given upstream x-y pair, all u-v combinations in the last three U of I chambers were tested as "seed" points, beginning in the fifth chamber and proceeding upstream. The extrapolated position of the y view track was required to be within 1.0 cm of the y coordinate calculated from the u and v coordinates of the seed point.

If this condition was satisfied, a road in x through the remaining U of I chambers was predicted from the seed point and the upstream x track. A search was then made for confirming hits along this road. The width of the road varied from 1.2 to 5.0 cm as the distance over which the extrapolation was made increased.

If $< 70\%$ of the maximum possible number of planes through which the track could have passed are found to have confirming hits, the seed point is rejected, and the next seed point is tried. This process was continued until all x - y track combinations and all seed points had been tested.

To determine the momentum of the track, the (x, z) coordinates of the points found in the U of I chambers were fit to a circle. The radius R and the magnitude B of the "hardedge" field used for the fit were determined by setting $R=R_0/k$ and $B=B_0/k$. R_0 and B_0 are the nominal radius and magnitude of the hardedge field, and the constant k appropriate for the initial plane used had been found by minimizing the disagreement between the hardedge field predictions of trajectories and those calculated numerically using the map of the CCM field. Finally, B_0 was adjusted by $+0.8\%$ to give the correct mass to the ψ . The full procedure is detailed in Hahn (1983).

The pattern recognition process tended to produce multiple copies of the same track. For example, chamber noise could result in false points adjacent to a real seed point, resulting in a cluster of tracks, of which only one was real.

The rejection of false tracks was known generically as "weeding". This involved identifying pairs of same-sign tracks with almost identical trajectories, and flagging as bad the track with fewer associated U or I chamber hits, or larger χ^2 . (Here χ^2 is defined as the sum of the squares of the deviations of the fit track from the measured points.)

The weeding algorithms were usually tailored to the specific process being studied. We will return to this discussion in the context of the charged-K and dimuon analyses.

3.4 The Drift Chamber Vernier

As mentioned previously, the problems with the drift chamber delay lines and the resulting large two- and fourfold ambiguities made even two-point downstream trackfinding ineffective. Instead, the drift chambers were used essentially as fine-grained hodoscopes. The information present was used to correct the track momenta and downstream x slopes and intercepts for tracks already reconstructed in

the magnet portion of the spectrometer by means of the U of I chambers. The resolution in x was 0.066 cm, adequate for a significant reduction of the momentum error.

The upstream tracks were extrapolated into the drift chambers using the optimized hardedge approximation of the CCM field. The vernier was accomplished in two stages. First, the extrapolated track was corrected using the the closest hit present within a tolerance of 1.6 cm in the farthest upstream drift chamber. A search was made through the remaining two chambers for hits within tolerance of the corrected track. A fit was then performed for the downstream track parameters using the associated drift chamber hits plus the downstream impact parameter coordinates as calculated from the upstream track information. (The impact parameter of a track entering or leaving the CCM is simply its distance from the center of the field, projected on the x - z plane. The azimuthal symmetry of the CCM field implies equality of the upstream and downstream impact parameters. The impact parameter coordinates are those of the point of the distance of closest approach of the extrapolated x track to the center of the field.) Finally, the momentum was recalculated, using the bend angle between the upstream (80 cm chamber x) track and the new downstream track.

The rationale behind the two step correction algorithm is that a track extrapolated downstream of the CCM will deviate more from the true trajectory the farther downstream it is projected. Since all ambiguities are resolved by taking the closest drift chamber hit to the extrapolated track, it is more likely that the ambiguity will be resolved correctly in the first chamber that has a hit associated with the given upstream track.

The use of the drift chamber vernier has a considerable effect on the mass resolution. The measured FWHM of the ψ , for example, is improved by $70 \text{ MeV}/c^2$, from 190 to $120 \text{ MeV}/c^2$. The improvement is due to the reduction in momentum error associated with the large lever arm afforded by the drift chambers.

3.5 Trackfitting

Once all the MWPC and drift chamber information is extracted for a given track, it is desirable to perform a global fit to all points simultaneously. In addition, at this stage a model of the CCM field more closely corresponding to reality than the hardedge approximation can be used.

A track is defined by the vector $\vec{T}=(A_x, B_x, q, A_y, B_y)$, where A_x (A_y) is the x (y) intercept of the upstream track in the $z = 0$ plane, B_x (B_y) is the upstream x (y) slope, and $q=1/p$ is the reciprocal of the (signed) momentum. The problem is to minimize

$$\chi^2 = \sum_i \left[\left(\frac{x_p^i(\vec{T}) - x_m^i}{\sigma_x^i} \right)^2 + \left(\frac{y_p^i(\vec{T}) - y_m^i}{\sigma_y^i} \right)^2 \right]$$

with respect to the track parameters \vec{T} . Here x_m^i (y_m^i) is the measured x (y) point, x_p^i (y_p^i) is the predicted x (y) point in chamber i , and σ_x^i (σ_y^i) is the x (y) resolution (standard deviation) of chamber i . (For simplicity, we will from this point on subsume the resolutions into the definitions of the x and y .) Minimization of the χ^2 gives a nonlinear system of equations in this case. The problem is linearized by expanding x_p^i and y_p^i about the approximate track parameters $\vec{T}_0=(A_x^0, B_x^0, q^0, A_y^0, B_y^0)$ given by the circle fit and the drift chamber vernier. Then

$$\begin{aligned} x_p^i(\vec{T}) &\cong x_p^i(\vec{T}_0) + \delta x^i \\ y_p^i(\vec{T}) &\cong y_p^i(\vec{T}_0) + \delta y^i, \end{aligned}$$

with

$$\begin{aligned} \delta x^i &= \sum_j \frac{\partial x_p^i}{\partial T_j} \delta T_j \\ \delta y^i &= \sum_j \frac{\partial y_p^i}{\partial T_j} \delta T_j. \end{aligned}$$

The problem is now reduced to the minimization of

$$\chi^2 \cong \sum_i \left[(r_x^i + \delta x^i)^2 + (r_y^i + \delta y^i)^2 \right]$$

to obtain $\delta \vec{T}$, the corrections to the starting values of the track parameters \vec{T}_0 . The quantities $r_x^i = x_p^i(\vec{T}_0) - x_m^i$ and $r_y^i = y_p^i(\vec{T}_0) - y_m^i$ are the residuals of the measured points with respect to the track defined by the starting parameters.

The derivatives have a simple analytical form only in the region upstream of the CCM. Elsewhere the derivatives are obtained numerically—in the drift chambers from the hardedge model, and in the U or I chambers from the corrected field as given by CYMOM. (This is a set of routines which approximate the true CCM field based on the actual field map. Further details are found in Hahn (1983).)

The linearized χ^2 given above is then differentiated with respect to the corrections $\delta \vec{T}$, and the derivatives set equal to zero to obtain the values of $\delta \vec{T}$ which minimize the χ^2 . This yields the 5 x 5 linear system

$$\sum_K A_{jK} \delta T_K = C_j$$

with

$$A_{jK} \equiv \sum_i \left(\frac{\partial x_p^i}{\partial T_j} \frac{\partial x_p^i}{\partial T_K} + \frac{\partial y_p^i}{\partial T_j} \frac{\partial y_p^i}{\partial T_K} \right)$$

and

$$C_K \equiv - \sum_i \left(r_x^i \frac{\partial x_p^i}{\partial T_K} + r_y^i \frac{\partial y_p^i}{\partial T_K} \right)$$

which is readily soluble for $\vec{\delta T}$, using standard numerical matrix inversion techniques.

In principle the procedure can be iterated, but one application was found to be sufficient. A marked improvement in the FWHM of the ψ is observed (90 MeV/c² compared to 120 MeV/c² with the drift chamber vernier alone) when the global fit is performed on the muon tracks. This is important for the physics analysis of events associated with $\psi \Rightarrow \mu^+ \mu^-$ decays, as the background under any peak is proportional to its width.

3.6 Extracting the Dimuon Sample

The amount of computer time required to unpack the raw data and reconstruct the charged tracks was approximately 110 ms/event. In order to avoid processing the same events repeatedly, data summary tapes were used to store this information for future use.

The actual DST information for a single event consisted of two parts. One, the track common /TFRSH/, contained all tracks found (including the beam), pointers between tracks of different types (e.g. upstream x to upstream y), χ^2 of the tracks, and pointers to the MWPC hits used to form the tracks.

The second part included all the unpacked data for the event--- MWPC hit coordinates, drift times, hodoscope TDC times and latches, Cherenkov and lead-glass pulse heights, etc. In short, the DST contained all the information necessary to proceed to the next stages of the analysis, such as K^\pm identification and gamma finding.

Fewer than 10% of all events in the dimuon trigger sample actually had two reconstructible opposite-sign muons. Since these were the only events of interest, a pass was made through the data to extract and write to DSTs the true dimuon events.

Some rapid filtering of events was possible. About 10% could be rejected as not having the quadrant requirement satisfied in the M hodoscope, but for the remainder of the events it was necessary to perform the full trackfinding in order to decide whether a dimuon was present.

Considerable time was saved at no cost in the efficiency of muon finding by imposing a $6.0 \text{ GeV}/c$ lower limit inside the trackfinder on all track momenta. The DST would have enough information to reconstruct tracks of lower momentum if desired.

This set of dimuon DSTs was then used to perform the analysis described in the subsequent chapters. In addition to the dimuon trigger data, the charged-K and interaction trigger data were also processed and written to DSTs. For these, the amount of data was small enough so that all events could be saved, without any filtering.

CHAPTER 4

THEORY AND PHENOMENOLOGY

4.1 Quarks and Hadron Spectroscopy

Current understanding of the strong interaction is based on the idea of hadrons as composites of more fundamental entities, the quarks (Gell Mann, 1964; Zweig, 1964). These objects are assumed to be pointlike fermions, possessing the quantum numbers given in table 4.1. Five types (flavors) of quarks are needed to describe all known hadrons, but a sixth quark is expected on theoretical grounds (Kobayashi and Maskawa, 1973).

We are concerned here with the physics of light quark hadron resonances (those composed of u, d, s quarks and antiquarks). The $u, d,$ and s quark fields can be considered as forming a fundamental (triplet) representation of $SU(3)$, the group of 3×3 unitary unimodular matrices. Mesons, formed from quark-antiquark pairs, belong to the singlet and octet representations of $SU(3)$. (Symbolically, $\underline{3} \times \underline{3}^* = \underline{8} + \underline{1}$.) A general account of the applications of unitary symmetry ideas in particle physics is found in Lichtenberg (1978).

	I	I_3	Q	S	C	B
u	1/2	1/2	2/3	0	0	0
d	1/2	-1/2	-1/3	0	0	0
s	0	0	-1/3	-1	0	0
c	0	0	2/3	0	1	0
b	0	0	-1/3	0	0	1

Table 4.1. The quarks and their quantum numbers.

I — isospin

I_3 — z-component of isospin

Q — charge

S — strangeness

C — charm

B — beauty

All quarks have spin 1/2 and baryon number 1/3.

The vector ($J = 1$) and tensor ($J = 2$) meson multiplets are depicted in figure 4.1. This SU(3) classification of hadrons plays a role in high energy physics analogous to that of Mendeleev's periodic table in chemistry.

Table 4.2 gives the SU(3) wavefunctions for the vector and tensor mesons. The physical $I=0$, $I_3=0$ particles in each nonet are mixtures of the SU(3) eigenstates with the same quantum numbers. The ω (783) is observed to decay predominantly to 3π , the ϕ (1020) to $K\bar{K}$. This is not expected if the ω and ϕ correspond to the SU(3) eigenstates ω_8 and ω_1 . Rather, the decay channels indicate that the ω_8 and ω_1 mix to form the physical ω and ϕ , with the ϕ predominantly $s\bar{s}$, the ω $u\bar{u} + d\bar{d}$. This phenomenon is known as ideal mixing (Sakurai, 1962; Okubo, 1977) and is also observed in the $f(1270) - f'(1520)$ system.

Quark spins are incorporated naturally into the model by extending the symmetry group to SU(6). The quark flavors and spins form a fundamental sextet representation. The mesons then belong to the $\underline{1} + \underline{35}$ ($= \underline{6} \times \underline{6}^*$) representations. Both the pseudoscalar and vector meson octets are contained in the $\underline{35}$.

Finally, the orbital angular momentum of quarks is accounted for by the inclusion of O(3), the three-dimensional orthogonal group. The representation of O(3) is specified by the orbital angular momentum L. The governing symmetry group of the light hadrons is then

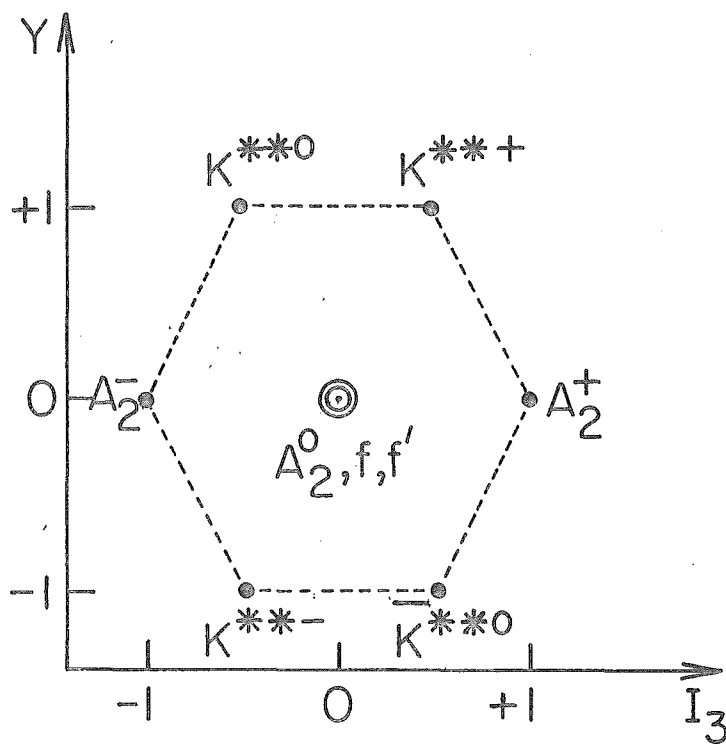
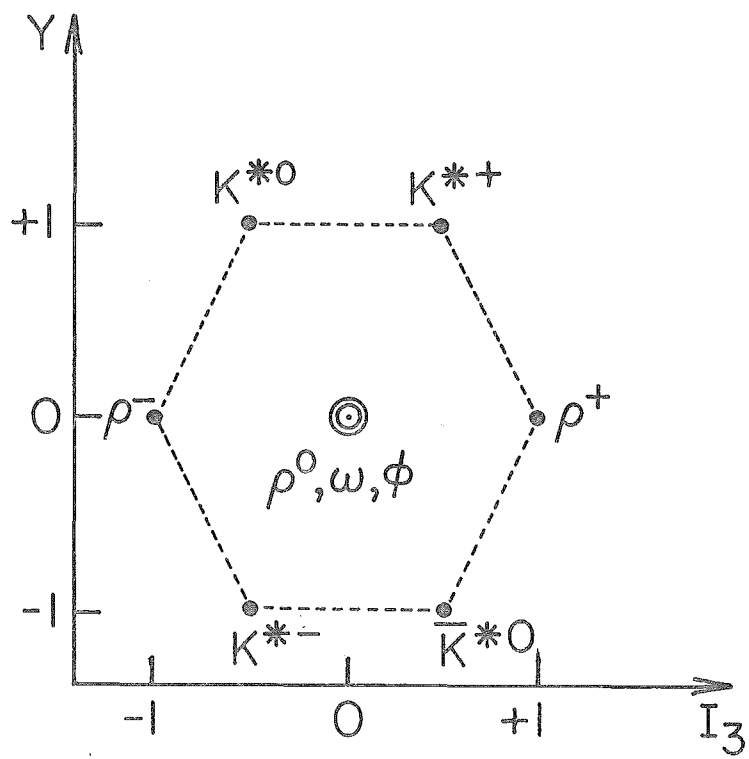


Figure 4.1. The vector and tensor meson nonets.

<u>MESON</u>	<u>WAVEFUNCTION</u>
$\rho^+(A_2^+)$	$-u\bar{d}$
$\rho^0(A_2^0)$	$(u\bar{u}-d\bar{d})/\sqrt{2}$
$\rho^-(A_2^-)$	$d\bar{u}$
$\omega_8(f_8)$	$(u\bar{u}+d\bar{d}-2s\bar{s})/\sqrt{6}$
$\omega_1(f_1)$	$(u\bar{u}+d\bar{d}+s\bar{s})/\sqrt{3}$
$K^{*+}(K^{**+})$	$u\bar{s}$
$K^{*0}(K^{**0})$	$d\bar{s}$
$\overline{K}^{*0}(\overline{K}^{**0})$	$-s\bar{d}$
$K^{*-}(K^{**-})$	$s\bar{u}$

Table 4.2. SU(3) wavefunctions for the vector (tensor) mesons.

$SU(6) \times O(3)$.

Quarks, being fermions, are expected to obey the Pauli exclusion principle. In the $SU(6) \times O(3)$ picture, difficulties arise with the symmetry properties of baryon wavefunctions, which are symmetric rather than antisymmetric as expected for an object composed of three fermions. An additional degree of freedom, color, is introduced to remedy this condition. Each quark is assumed to come in three colors, with the governing symmetry group $SU(3)_{\text{COLOR}}$, which is not related to the $SU(3)_{\text{FLAVOR}}$ discussed previously. Unlike $SU(3)_{\text{FLAVOR}}$, $SU(3)_{\text{COLOR}}$ is, so far as is known, an exact symmetry. All physical hadron states are color singlets. The color part of the wavefunction restores the antisymmetry demanded by the Pauli exclusion principle.

The existence of color has direct observational consequences as well. The calculated and measured values of the ratio $R = \sigma(e^+e^- \Rightarrow \text{hadrons}) / \sigma(e^+e^- \Rightarrow \mu^+\mu^-)$ are in serious disagreement unless three colors of quarks are assumed (Schwitters and Strauch, 1976). Another indication of color arises in the theoretical value of $\Gamma(\pi^0 \Rightarrow \gamma\gamma)$, which again is in agreement with experiment only if color is introduced (Adler, 1969; Bell and Jackiw, 1969).

4.2 Quark Dynamics

The candidate theory for the interactions of quarks is quantum chromodynamics (QCD). In it, color plays the same role as electric charge in quantum electrodynamics (QED). The strong interaction is mediated by vector quanta called gluons.

In its present state QCD has not been successfully applied to the production of light hadron resonances. It is straightforward in perturbative QCD to calculate (for example) the cross section for quark-antiquark annihilation $q\bar{q} \rightarrow q'\bar{q}'$, treating the initial and final state quarks and antiquarks as free particles (an assumption strictly true only in the infinite momentum limit). Difficulties arise, however, in "dressing" the $q'\bar{q}'$ pair, that is, determining the probability of forming a given hadron from the $q'\bar{q}'$ pair. (Quarks are apparently confined in hadrons-- no evidence for free quark production has been observed.)

We will therefore attempt to apply a simple phenomenological model of hadron production. Use is made of elementary symmetry and statistical considerations to predict the relative yields of particles produced in hadronic interactions.

4.3 Hadron Production and the Additive Quark Model

The particular model to be considered here is the additive quark model of the Leningrad group (Anisovich and Shekhter, 1973; Shekhter and Shcheglova, 1978). The authors themselves refer to their work as "quark combinatorics".

The assumptions of this model are relatively straightforward. A "gas" of quarks and antiquarks is formed in the collision, from which the hadrons in the central region materialize. The relative yields of hadrons produced in the central region are independent of the beam and target hadrons, and the total energy of the collision. Yields in the beam and target fragmentation regions are expected to depend strongly on spectator quark effects; thus the assumption of beam and target independence is not expected to hold there.

Within a given $(35, L)$ of $SU(6) \times O(3)$, the relative probability of producing a particle of total spin J is $2J+1$, if there is no symmetry breaking. To accommodate the observed breaking of $SU(6)$, the production of strange quarks is assumed to be suppressed with respect to u and d quarks by a factor $\lambda < 1$, which should also be independent of the incident hadrons and the total energy.

In comparing the yields of two members of the $L=0$ multiplet, such as, for example, ω and ϕ , it is necessary to allow for "feed-down" contributions from multiplets of $L \gg 1$. An additional phenomenological factor α is included to describe the production rate of $(\underline{35}, L=1)$ states relative to the $(\underline{35}, L=0)$. Any contributions from $L > 1$ states are neglected, although in principle one could define additional suppression factors for these higher orbital angular momentum states. One difficulty here is the paucity of experimental data on $L > 1$ mesons.

Table 4.3 summarizes the predictions of the model for centrally produced mesons. For $L=0$ states two processes contribute. The direct term gives the yield of directly produced states, while the indirect term accounts for "feed-down" from decays of $L=1$ mesons. The latter term is calculated from the experimental branching ratios of the $L=1$ states into $L=0$ states.

Thus, to take the example of interest for this analysis, the relative yield of $\phi(1020)$ is proportional to $3\lambda^2$. No feed-down term is included, because no $L=1$ meson decays involving the ϕ are known.

The relative direct $\omega(783)$ yield is 3. The indirect yield is given by

$$\sum_M (2I_M + 1)(2J_M + 1) BR(M \Rightarrow \omega X) \lambda^{N_M^S} \alpha.$$

<u>MESON</u>	<u>DIRECT</u>	<u>INDIRECT</u>
J=1, L=0: ρ (769)	3	$(6.5+2.4\lambda)\alpha$
ω (783)	3	$(10.6+2.2\lambda)\alpha$
ϕ (1020)	$3\lambda^2$	-----
K^* (890)	3λ	$4.5\lambda\alpha$
J=2, L=1: A (1320)	5α	-----
f (1270)	5α	-----
f' (1515)	$5\lambda^2\alpha$	-----
K^{**} (1430)	$5\lambda\alpha$	-----

Table 4.3. Relative yields of vector and tensor mesons in the central region.

The sum is over all of the $L=1$ mesons M which can decay to ω . I_M and J_M are the isospin and spin of M , respectively. $BR(M \Rightarrow \omega X)$ is the branching ratio of M into the final state containing the ω , and N_M^S is the number of strange + antistrange valence quarks in M . The indirect ω yield is found to be $(10.6+2.2\lambda)\alpha$, representing contributions from the decays $B(1235) \Rightarrow \omega\pi$, $A_2(1320) \Rightarrow \omega\pi\pi$, $K^{*0}(1430) \Rightarrow \omega K$, and $\rho(1280) \Rightarrow \omega K$. (The indirect yields given here and in table 4.3 differ slightly from those of Shekhter and Shcheglova. We have reevaluated these terms, using the latest (1982) PDG values of the branching ratios as input.)

One test of the predictions of this model is to measure λ using the observed ratio of ϕ to ω production. The value obtained can then be compared with that obtained by other experiments using different hadron pairs, initial hadrons, and total energies.

In addition, the relative yields of ϕ and $f'(1520)$ provide a means of measuring α . This again can be compared to the existing data from other experiments.

4.4 Strangeness Suppression in Other Processes

The suppression of strange quarks with respect to lighter quarks is not of course limited to hadron-hadron collisions. A systematic analysis of the world data has been performed (Malhotra and Orava, 1983), and the strange quark suppression factor λ has also been extracted from $\psi \Rightarrow$ hadrons, $e^+e^- \Rightarrow$ hadrons, and $\nu N \Rightarrow$ hadrons. We will discuss these results in the final chapter, when we compare our value of λ with the existing data.

CHAPTER 5
FINAL DATA ANALYSIS AND RESULTS

5.1 The Dimuon Spectrum

The basic signature of a muon in the E610 spectrometer is a charged track which fires an element of the M hodoscope. Because of the large background in the low mass region of the dimuon spectrum, it was desirable to impose some additional straightforward cuts on muon track quality, with the aim of improving the signal-to-noise for the ω and ϕ .

First of all, every muon track was required to have at least one associated drift chamber hit. This served a dual purpose: as an additional item of track information in a system as low in redundancy as ours, and also to improve the track momentum resolution (see section 3.4).

Each track was required to have an efficiency of greater than 70%, i.e. that 70% of the total number of u-v planes through which the track could have passed had associated hits. Again, this helped to eliminate bogus tracks.

A weeding was performed on muon tracks passing the drift chamber and efficiency requirements. All pairs of same-sign muons in a given event were compared. If the opening angle of the pair was less than 2.4 mr, or if the momenta of the two tracks differed by less than 0.1% of their average momentum, the pair was flagged as being the manifestation of a doubly found track. (These cuts were determined on the basis of histograms of the opening angles and momentum differences for all same sign dimuon pairs.) In this case one of the two was rejected, by examining the number of hits per track and eliminating the one with fewer hits. If both tracks had the same number of hits, the track with the larger χ^2 was rejected.

The appropriate M hodoscope element for each muon was required to have been latched and also digitized as recorded by the TDCs. (This was an additional check that the muon candidate was in time with the interaction.) Finally, only opposite sign dimuon pairs satisfying the quadrant requirement in the M hodoscope were used.

Figure 5.1 shows the resulting dimuon mass spectrum. Clear ω , ϕ and ψ peaks are visible. The mass resolution is sufficient to separate the ω from any ρ^0 peak present. The ρ^0 itself is so broad (FWHM = 154 MeV/c²) that it could not be distinguished from the background at the statistical level of this experiment.

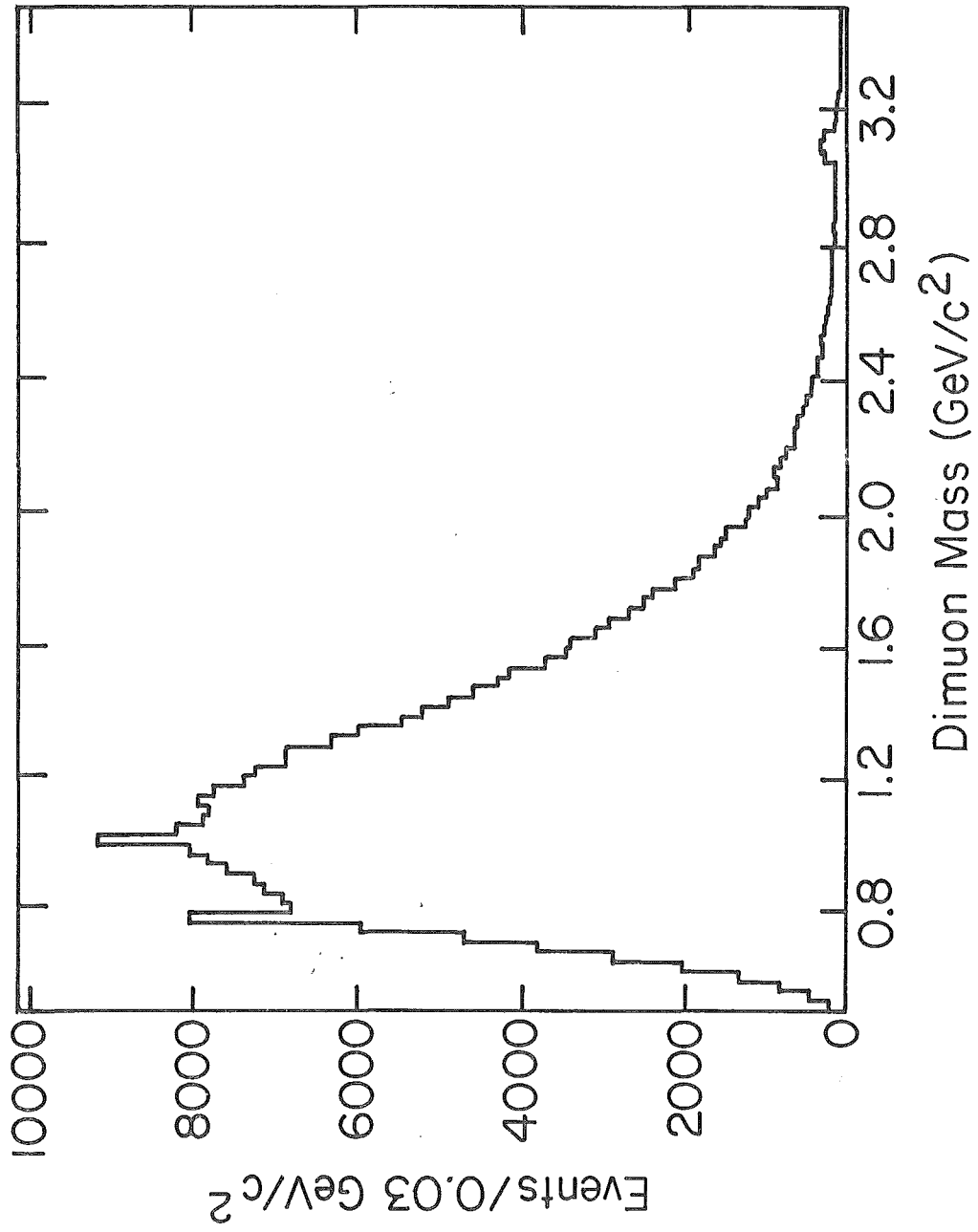


Figure 5.1. The full dimuon mass spectrum.

The high mass (ψ) region of the spectrum will not be considered any further here. Exhaustive accounts of the ψ physics are found in the other E610 theses (Hahn, 1983; Budd, 1983; Hossain, 1981). Instead, we now turn our attention to the low mass region of the spectrum, to the physics of ω and ϕ production.

Figure 5.2 shows the dimuon spectrum between 500 and 1500 MeV/c^2 . The large background under the ω and ϕ results from pion and kaon decays in flight, and punch-through (hadrons which manage to penetrate the steel absorber).

In order to obtain the yields of ω and ϕ , the spectra are fit to quadratic polynomial backgrounds plus Gaussian peaks. The yields, based on approximately 300 000 fully reconstructed dimuon events, are found to be 3400 ± 240 ω and 1700 ± 230 ϕ events, with a FWHM of $39 \text{ MeV}/c^2$ and $30 \text{ MeV}/c^2$ respectively. The corresponding masses are found to be $784 \pm 1 \text{ MeV}/c^2$ and $1023 \pm 1 \text{ MeV}/c^2$, in reasonable agreement with the Particle Data Group (PDG) values (Roos, 1982). The ω and ϕ mass regions with the fit curve superposed are shown in figures 5.3 and 5.4, and the corresponding background subtracted signals in figures 5.5 and 5.6. (In each case the fit was performed over the mass range shown in the histogram.)

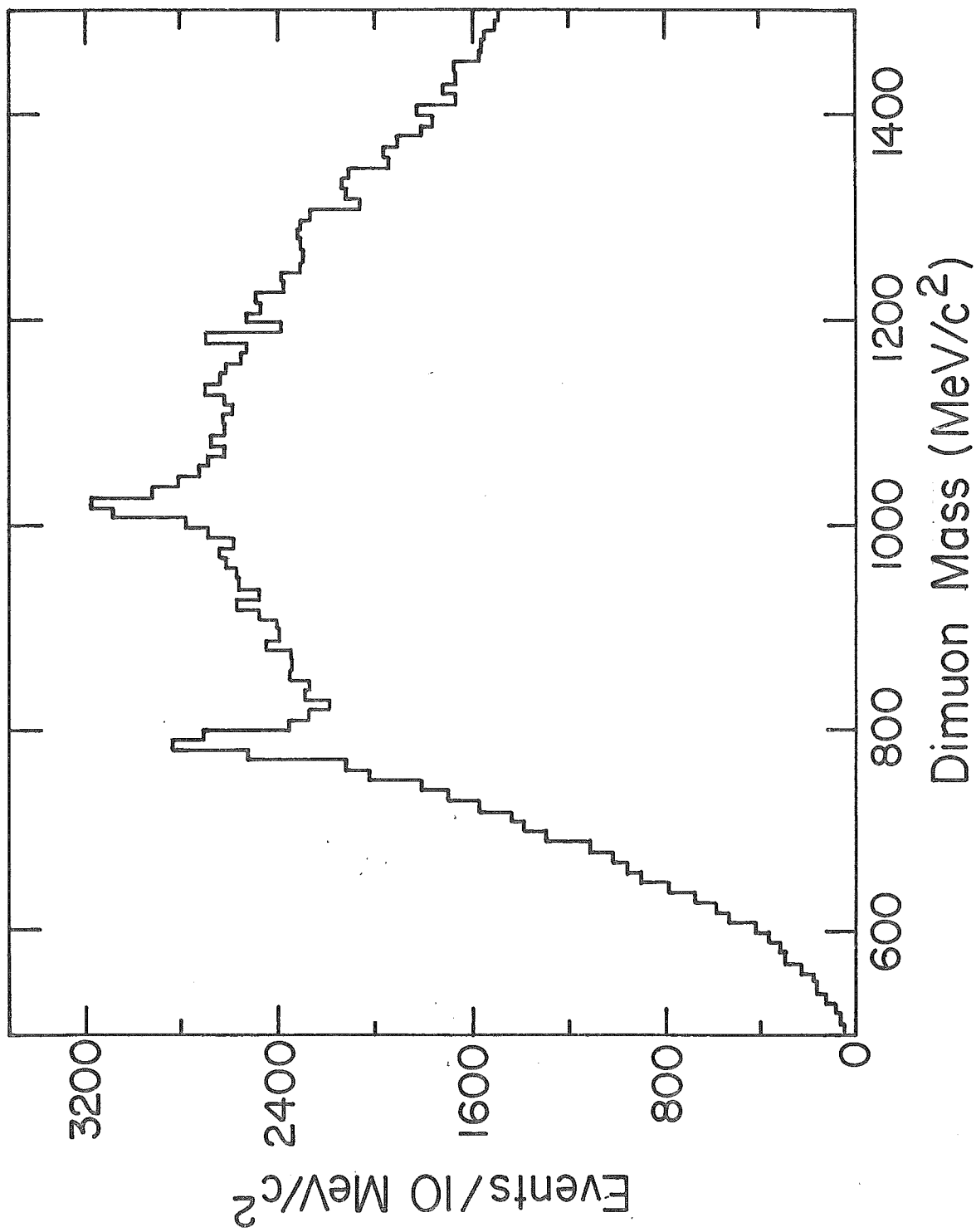


Figure 5.2. The dimuon mass spectrum, $\omega - \phi$ region.

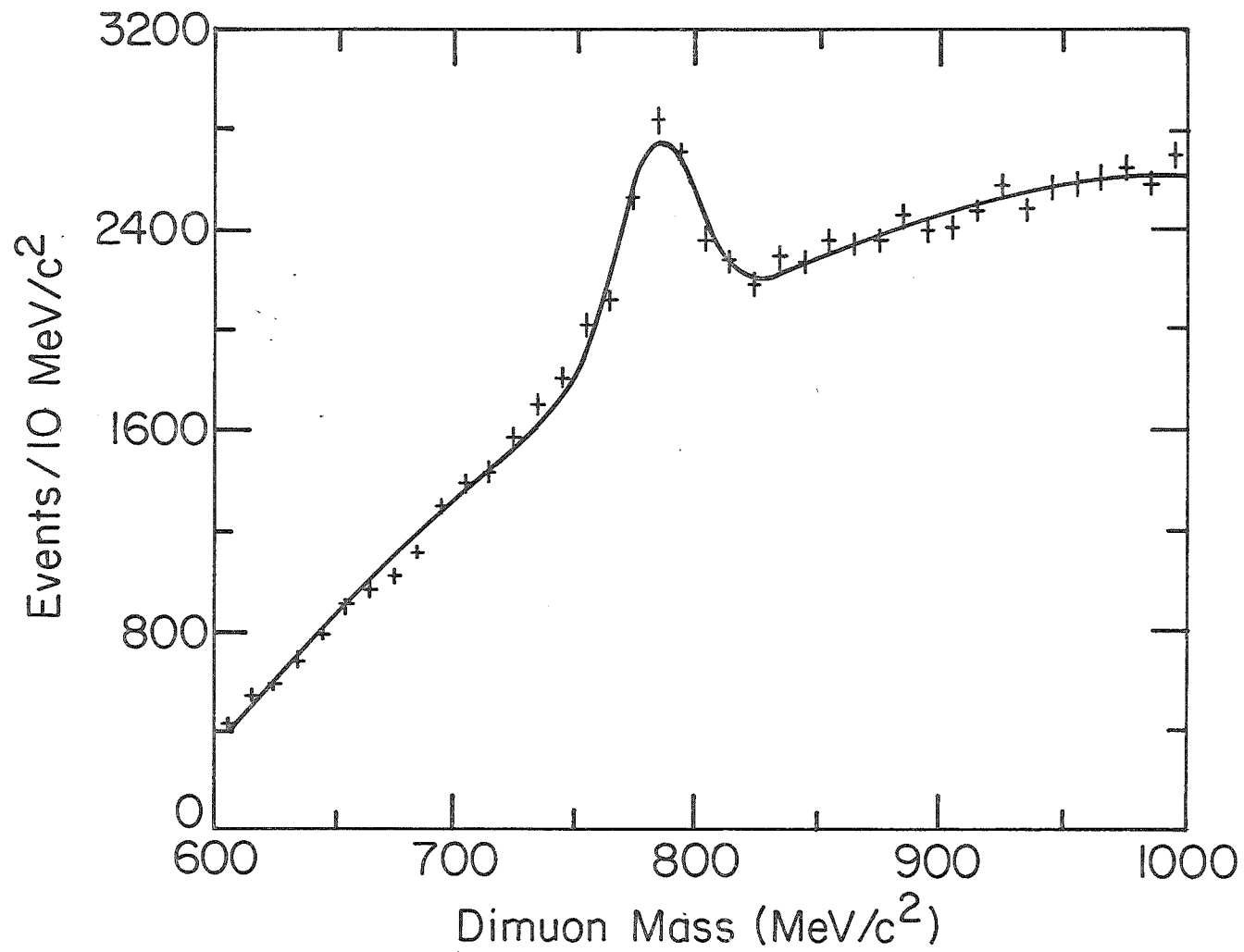


Figure 5.3. The $\omega \Rightarrow \mu^+\mu^-$ signal. The curve is a least squares fit to a Gaussian plus quadratic background.

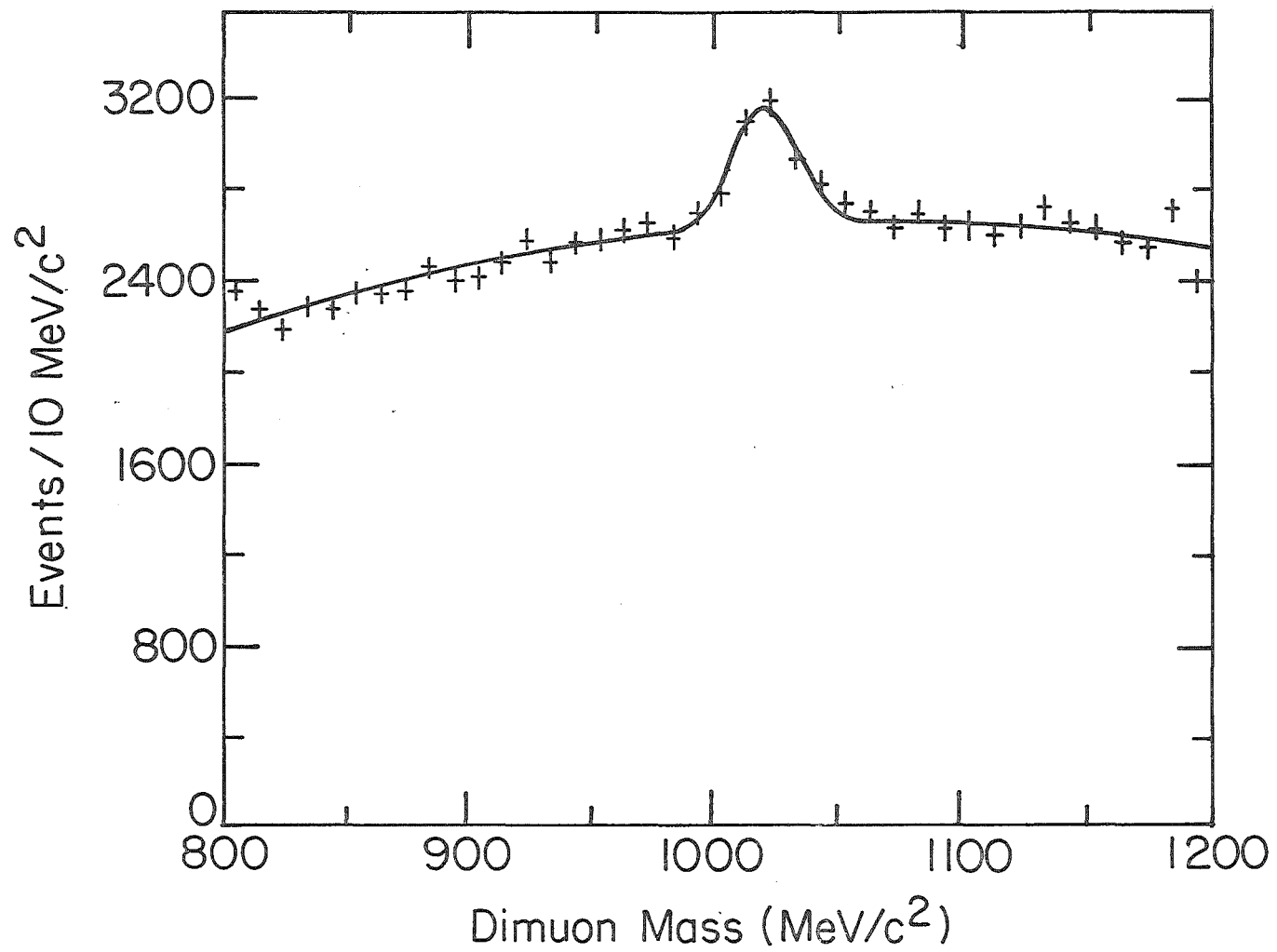


Figure 5.4. The $\phi \Rightarrow \mu^+\mu^-$ signal. The curve is a least squares fit to a Gaussian plus quadratic background.

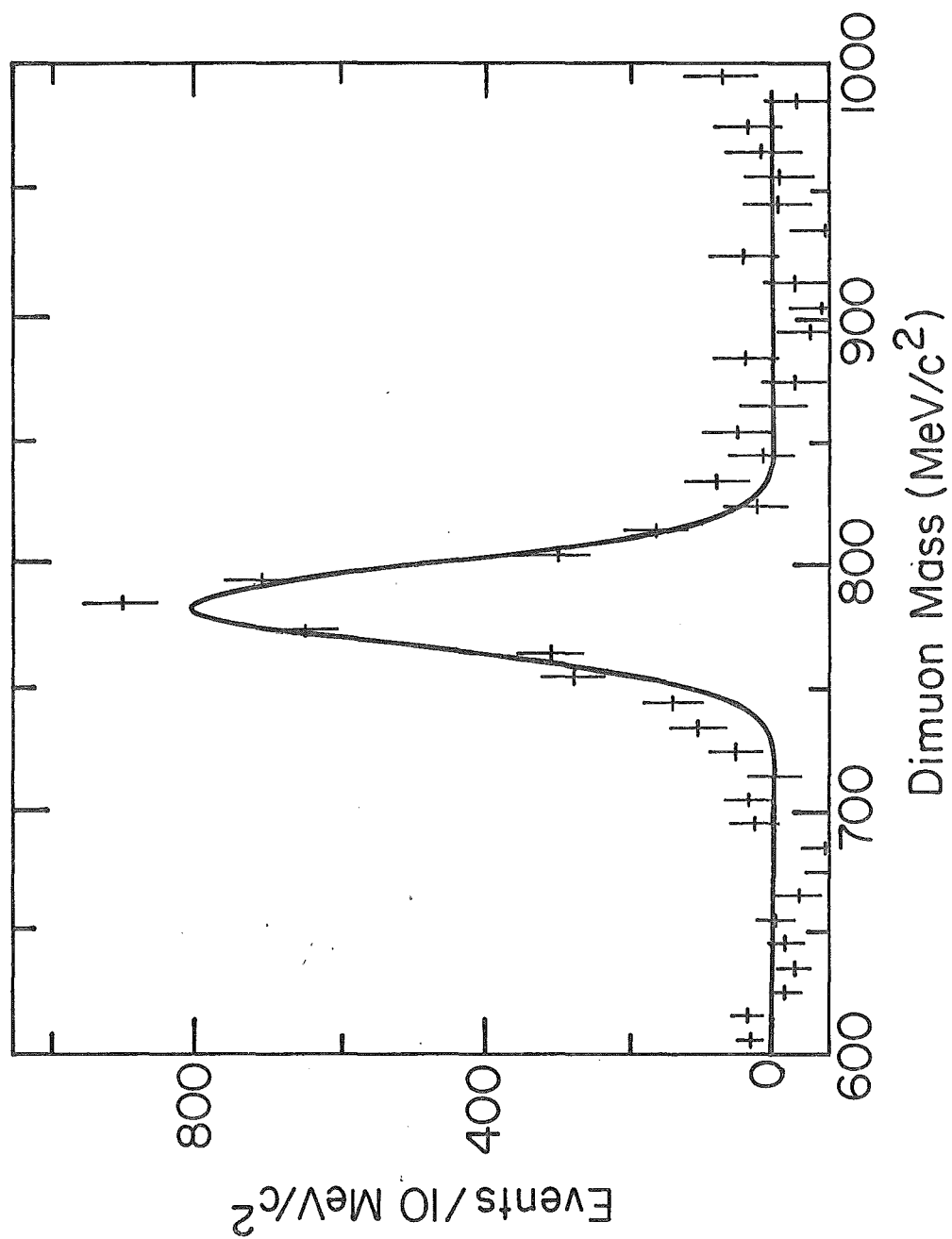


Figure 5.5 The background subtracted ω signal.

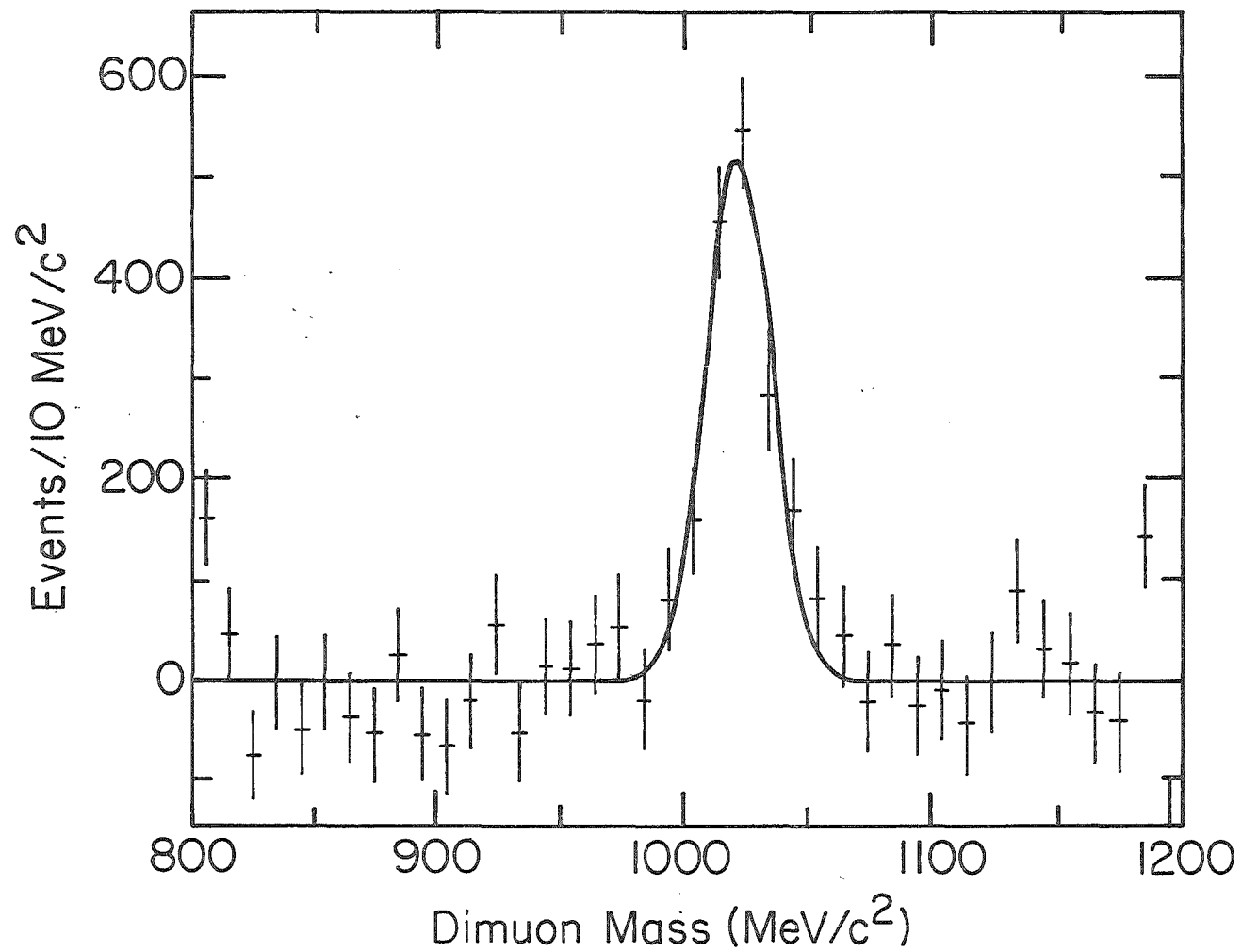


Figure 5.6. The background subtracted ϕ signal.

5.2 Kaon Identification and the $K^+ K^-$ Spectrum

The multicell Cherenkov counter is described in appendix A. We will be concerned here with the use of the Cherenkov counter as a means of distinguishing between charged kaons and pions.

The existence of a velocity threshold effects the usefulness of Cherenkov radiation for particle identification. Figure 5.7 is a plot of the yield of Cherenkov photoelectrons (relative to a $\beta = 1$ particle) for the various secondary particles of interest, in N_2 at atmospheric pressure (the medium used in our apparatus). The threshold for pions is 6 GeV/c, and 21 GeV/c for kaons.

The actual momentum range for π -K discrimination was taken as 8 GeV/c - 21 GeV/c. The lower momentum limit corresponds to the half-light ($\bar{n}/\bar{n}(\beta=1) = 0.5$) momentum for pions.

All charged tracks in this momentum band were projected downstream to the plane of the Cherenkov mirrors ($Z = 700$ cm). Except for identified muons, all tracks were tested under the pion or kaon hypothesis. The size of the Cherenkov disk was calculated for each track in turn as a pion. The cells to which the track could have contributed light were then determined. If the ADC pulse height for each of these cells was in the pedestal region (consistent with there being no associated Cherenkov light), the track was called a kaon.

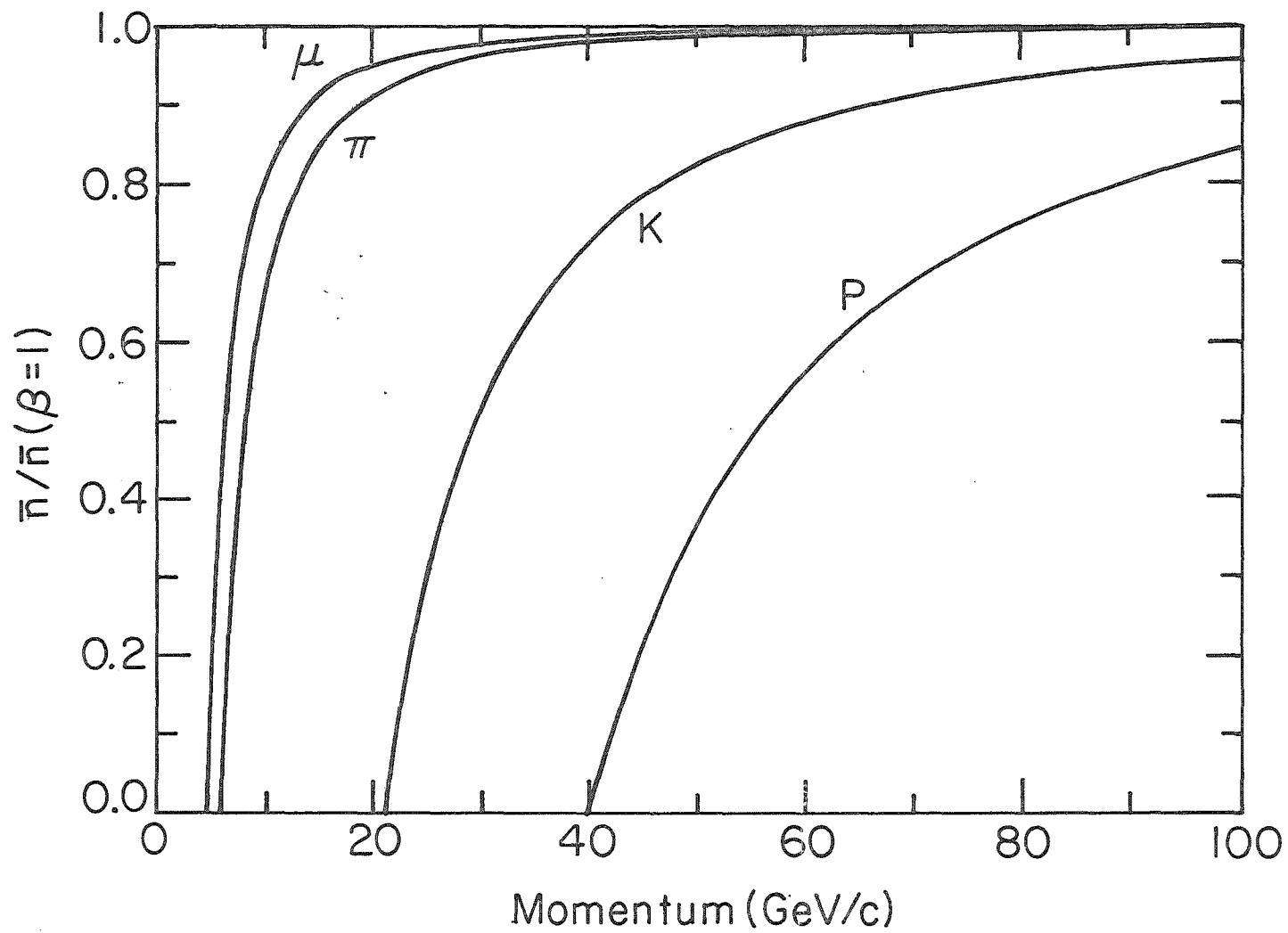


Figure 5.7. Cherenkov light output (relative to that from a $\beta = 1$ particle) as a function of momentum.

Because the kaon identification is based on the absence of Cherenkov light, any spurious track in the 8-21 GeV/c momentum band would have been identified as a kaon. As in the muon case, cuts on track quality are applied to the kaon candidates. The method used in rejecting bogus tracks is similar to that described in the previous section for muon tracks.

The K^+K^- mass spectrum from the charged-K trigger sample is shown in figure 5.8. A ϕ peak is seen. The background was fit to the form

$$C_1 (\pi - m_{TH})^{C_2} \exp(-C_3 (\pi - m_{TH}))$$

where the C_i are allowed to float, and $m_{TH} = 2m_K$. The function is more complicated than the simple polynomial used to fit the dimuon backgrounds because of the need to describe the threshold behavior of the K^+K^- spectrum. The ϕ peak was fit to a Gaussian. The area of the peak is 220 ± 30 events, with a FWHM = $10 \text{ MeV}/c^2$, and a mass of $1019 \pm 1 \text{ MeV}/c^2$. The χ^2/DOF of the fit is $65/(50-6)$.

5.3 Acceptances

We are concerned in this work primarily with the processes $\omega \Rightarrow \mu^+\mu^-$, $\phi \Rightarrow \mu^+\mu^-$, $\phi \Rightarrow K^+K^-$ and $f' \Rightarrow K^+K^-$. In order to convert the observed yields into absolute yields, we need to correct for the

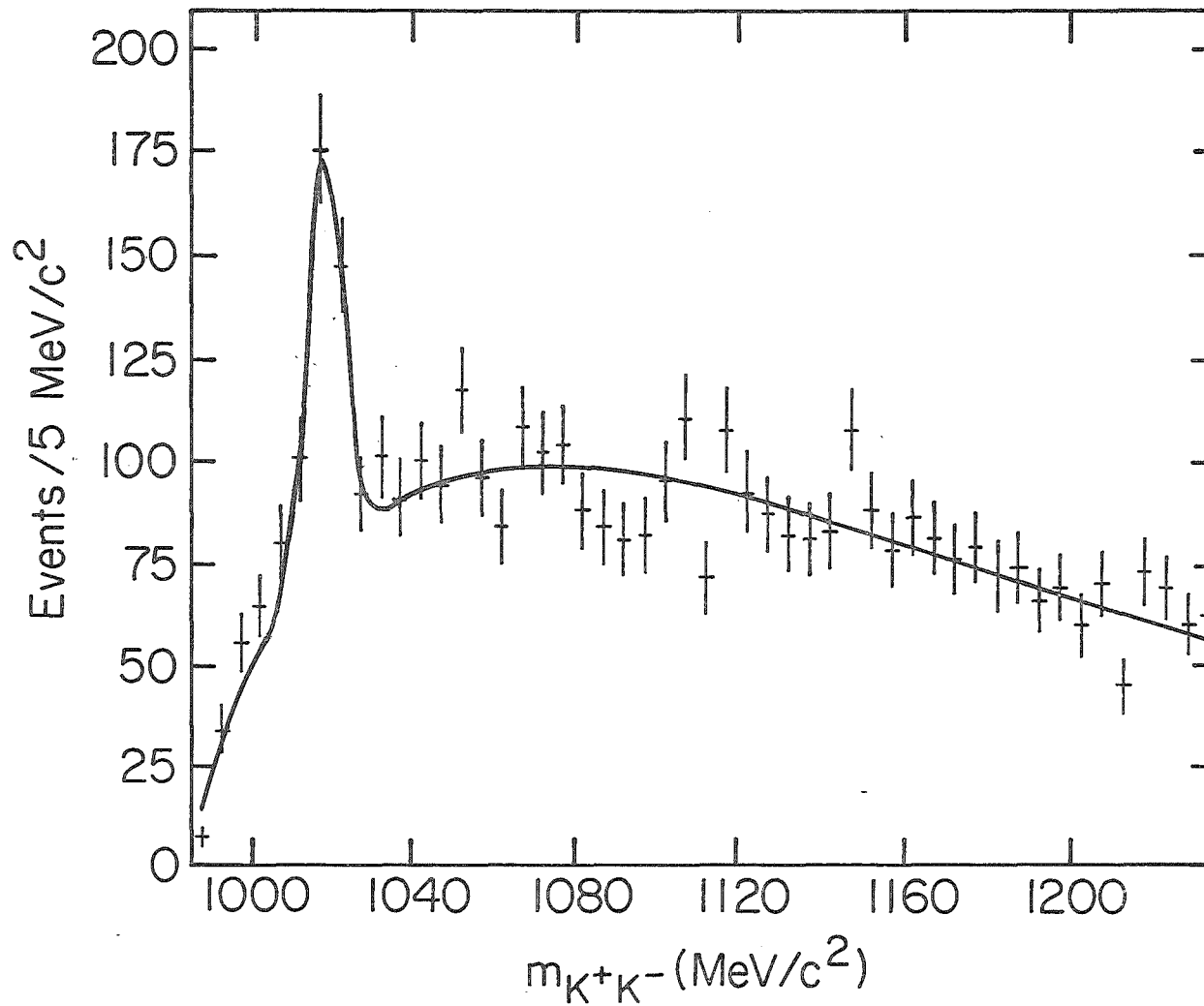


Figure 5.8. The K^+K^- mass spectrum. The curve is the result of the fit described in the text.

acceptance of the apparatus. This was done through the use of the Monte Carlo method.

Since all the processes of interest involve two-body decays, the general principles applied to all the acceptance calculations were rather similar. The calculation of the dimuon acceptances will be considered first.

The particle of interest was generated according to the distribution $E d^3\sigma/dp^3 \sim (1-x_F)^A e^{-Bp_T}$, as parametrized in Branson (1977). In this experiment the constants A and B were measured as a function of dimuon mass, using a very similar experimental setup to our own.

The particle was allowed to decay isotropically in its rest frame. (We will see later that this assumption is not critical to the main result.) The decay muons were tracked through a realistic simulation of the spectrometer, with the efficiency of each drift chamber and MWPC plane taken into account, as well as the overall geometry. Track cuts identical to those required in the analysis of the data were imposed. If the two muons in the generated event satisfied all the track requirements, the intersection of the tracks with the M hodoscope was checked. If the quadrant requirement was fulfilled, the event was accepted. The acceptance as a function of dimuon mass is plotted in figure 5.9.

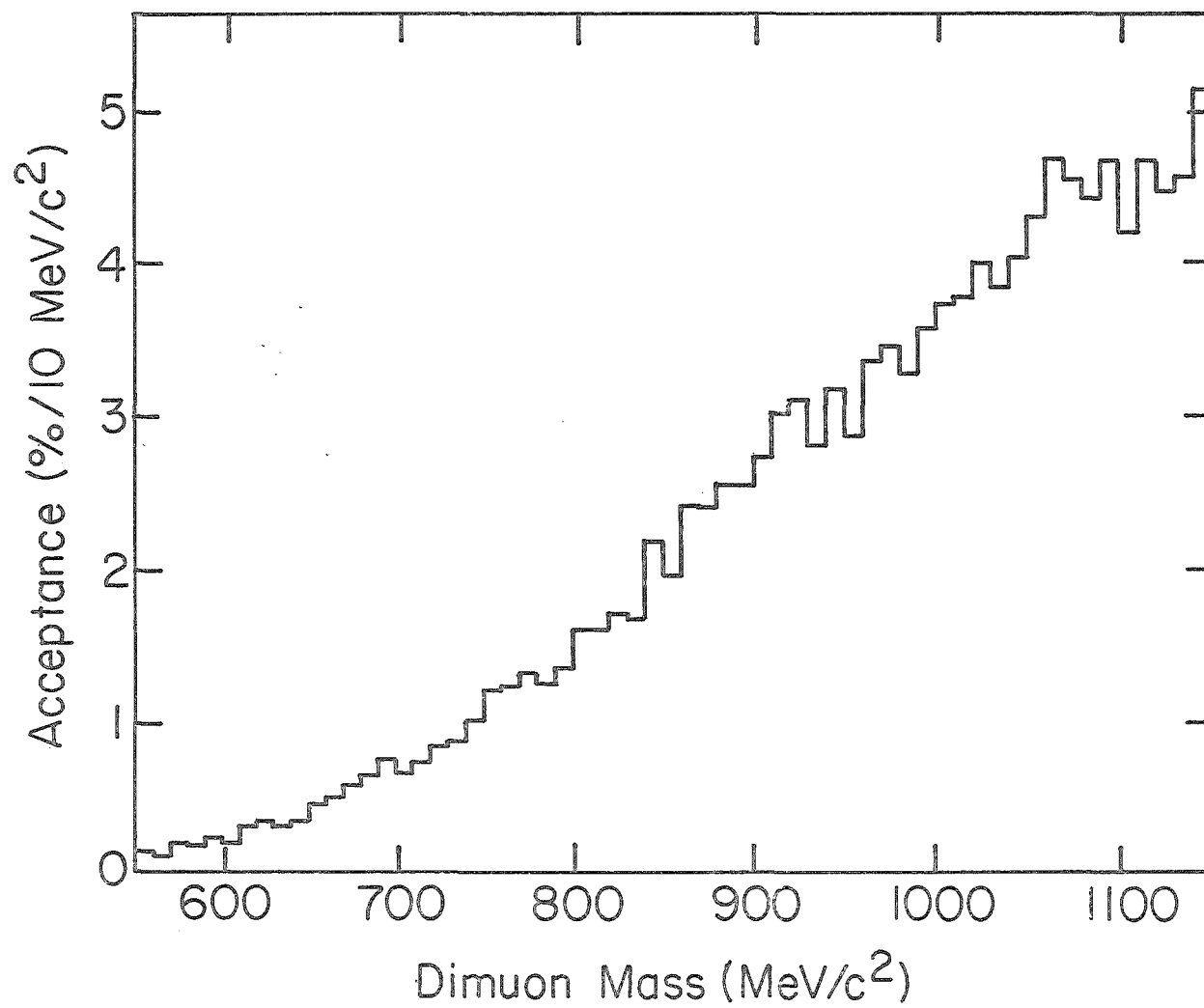


Figure 5.9. Acceptance as a function of the dimuon mass.

For the ω and ϕ , the parameters used were $A = 0.92$, $B = 3.81 \text{ (GeV/c)}^{-1}$ and $A = 1.60$, $B = 3.51 \text{ (GeV/c)}^{-1}$ respectively. The acceptances in x_F for the ω and ϕ are shown in figures 5.10 and 5.11. The difference in the shapes of the ω and ϕ acceptance curves is the result of the M hodoscope requirement in the trigger.

Calculation of the $K^+ K^-$ acceptances proceeded in a similar fashion, except that the requirement that both tracks have momenta in the 8-21 GeV/c range, and that both intersect the detection area of the Cherenkov counter, was substituted for the M hodoscope conditions. The ϕ was generated with the same A and B parameters as in the $\mu^+ \mu^-$ case. The corresponding parameters for the f' have not been measured. It was decided, in the absence of any other information, to use the same production parameters as for the ϕ . The $\phi \Rightarrow K^+ K^-$ integrated acceptance is then found to be 0.103, and the $f' \Rightarrow K^+ K^-$ integrated acceptance 0.073.

5.4 Search for the $f'(1515)$

As discussed in the previous chapter, the production of $L=1$ mesons is assumed to be suppressed relative to those with $L=0$. The parameter α , which measures the suppression, is assumed to be independent of the hadronic system from which the secondary particles

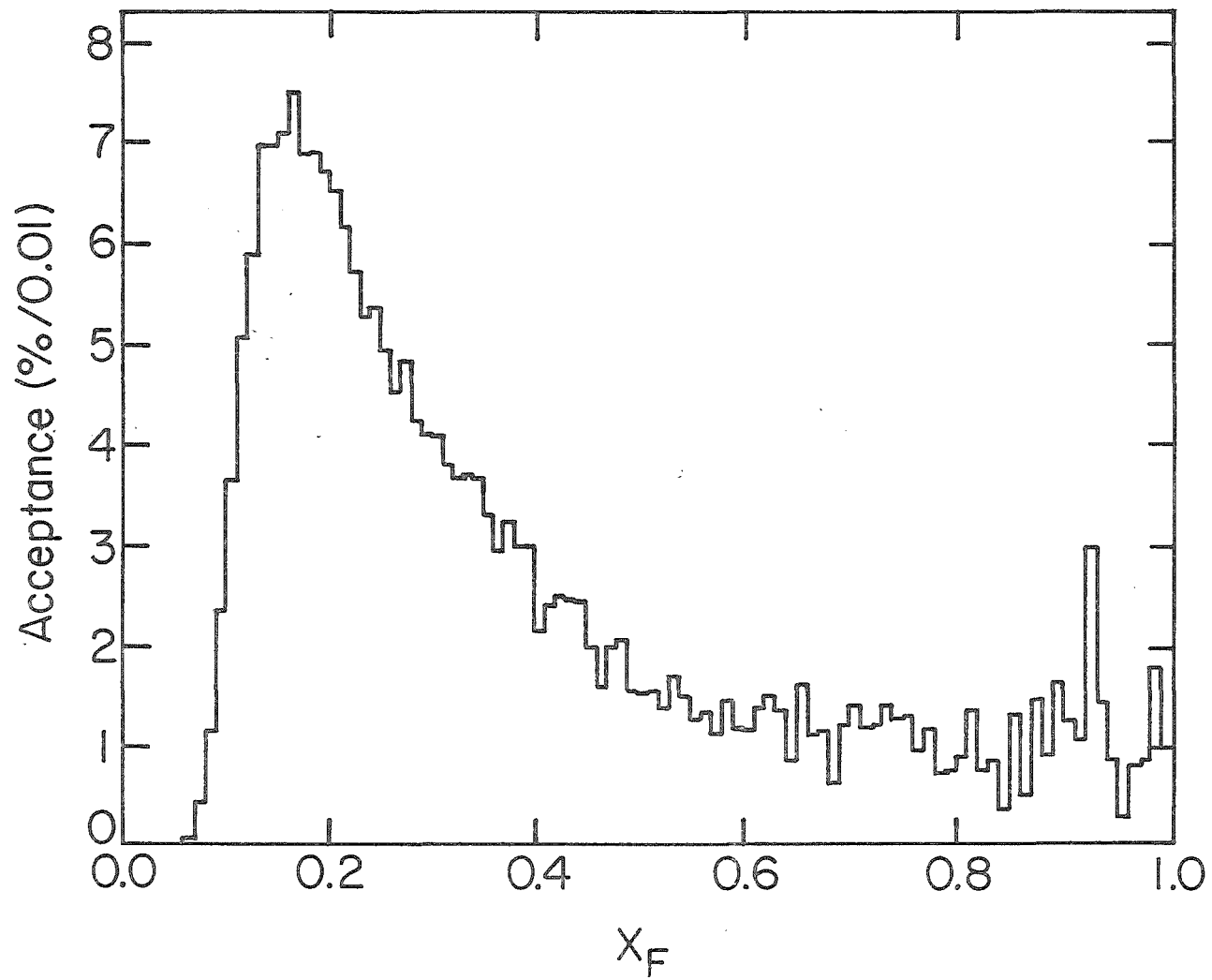


Figure 5.10. ω acceptance as a function of x_F .

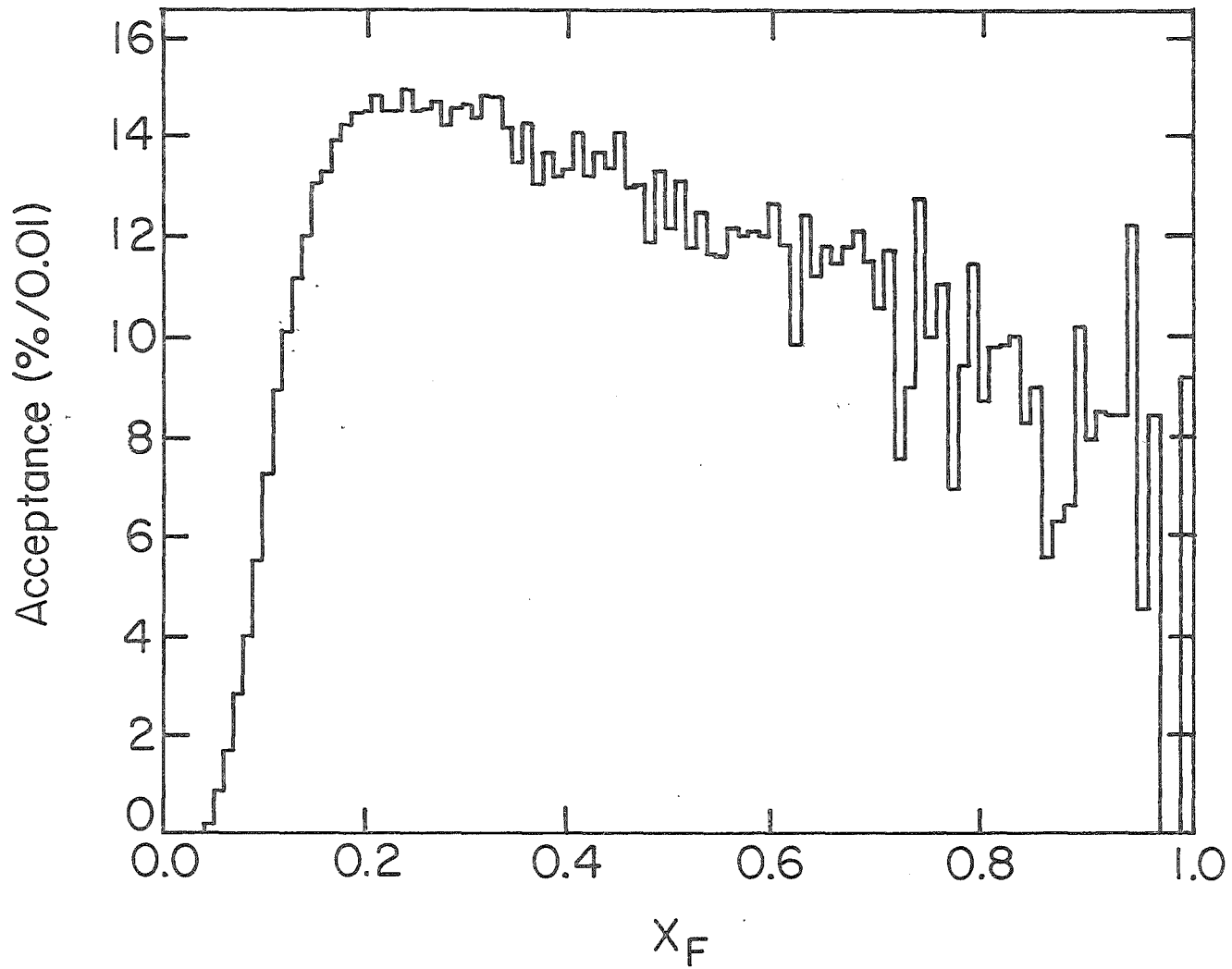


Figure 5.11. ϕ acceptance as a function of x_F .

are formed. From data on the relative production of $f(1270)/\rho(769)$ and $K^{*0}(1430)/K^{*0}(890)$, α has been determined to be 0.13 ± 0.03 (Shekhter and Shcheglova, 1978).

The basis for the introduction of α as a universal constant is not as firm as that for λ , which reflects the fundamental breaking of SU(3) symmetry. We have attempted a measurement of α using the relative production of $\phi \Rightarrow K^+ K^-$ and $f' \Rightarrow K^+ K^-$, which should be found in the ratio $f'/\phi = 5\alpha/3$ (table 4.3).

Figure 5.12 is the $K^+ K^-$ mass spectrum between 1150 and 1950 MeV/c². No evidence of a peak at the f' mass is found. We can, however, compute the expected f' yield based on the observed ϕ yield and the assumption that $\alpha = 0.13$.

The systematic errors here were somewhat difficult to deal with. The acceptance for the f' was calculated (section 5.3) using a model in which the f' was produced with the same x_F and p_{\perp} distributions as the ϕ . To compound the difficulty, the branching ratio for $f' \Rightarrow K^+ K^-$ has not been determined. The PDG tables (Roos, 1982) do state, however, that $f' \Rightarrow K^0 \bar{K}^0$ is dominant. We have taken $BR(f' \Rightarrow K^+ K^-) = 0.5$ as an upper limit.

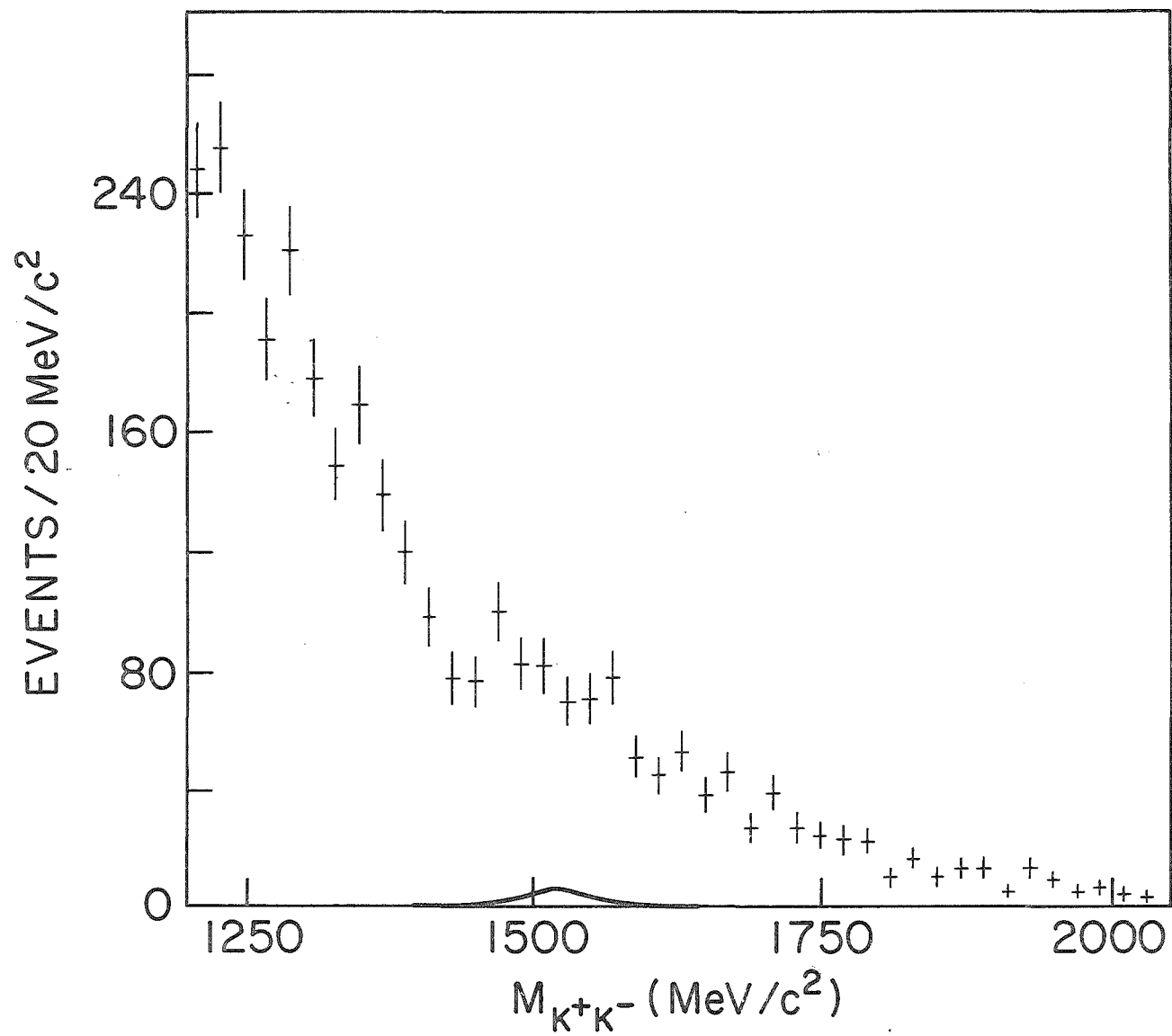


Figure 5.12. K^+K^- mass spectrum, f' region. The curve is the yield of $f' \Rightarrow K^+K^-$ predicted if $\alpha = 0.13$. (See text.)

Using these ingredients, the expected yield of f' is 34 events. A Breit-Wigner curve with this area and the PDG values for the FWHM ($75 \text{ MeV}/c^2$) and mass ($1520 \text{ MeV}/c^2$) of the f' is drawn in figure 5.12. The predicted yield is in agreement with the statistical errors on our data points, although the problems with the systematics suggest that this result be taken cum grano salis.

5.5 Measurement of λ

As discussed in chapter 4, the strangeness suppression constant λ can be measured from the central production ratio of ϕ to ω . The first problem to be addressed, then, is to define the central region in terms of the kinematic variables of the ω and ϕ .

Operationally, the central region of a hadronic collision is characterized by the absence of spectator quark effects. A hadron is produced centrally if it is not formed from spectator quarks (non-interacting valence quarks from either the beam or target particles). We will be concerned primarily with the effects of beam fragmentation. Target fragmentation effects become important only in the backward hemisphere, where the spectrometer has no acceptance for either ω or ϕ .

As in the nucleon, the quarks in the pion carry about half of the total momentum (Stroynowski, 1981). If the two valence quarks of the pion together carry half the pion momentum, it is reasonable to assume (conservatively) that any final state hadron with $x_F > 0.25$ is associated with a beam spectator quark.

Since the acceptance for the ω and ϕ begins to overlap for $x_F \geq 0.1$ (cf. figures 5.10 and 5.11), we take as centrally produced those events with $0.1 \leq x_F \leq 0.25$. Imposing this cut, we find 1940 ± 200 ω and 820 ± 170 ϕ events. (We will see later that the final result is rather insensitive to the precise x_F limits used to define the central region.)

An indication of the importance of spectator quark effects at larger values of x_F is obtained by comparison of ϕ production by pions and kaons. Figure 5.13 shows data taken by the ABCCCLW collaboration (Sixel, 1982). The shapes of $d\sigma/dx_F$ for pions and kaons are very similar for small x_F , but for $x_F > 0.2-0.25$ the distributions begin to diverge, with more ϕ production being observed from kaons in the large x_F region. This is taken as an indication that the fast forward ϕ 's are produced from the strange spectator quark of the kaon.

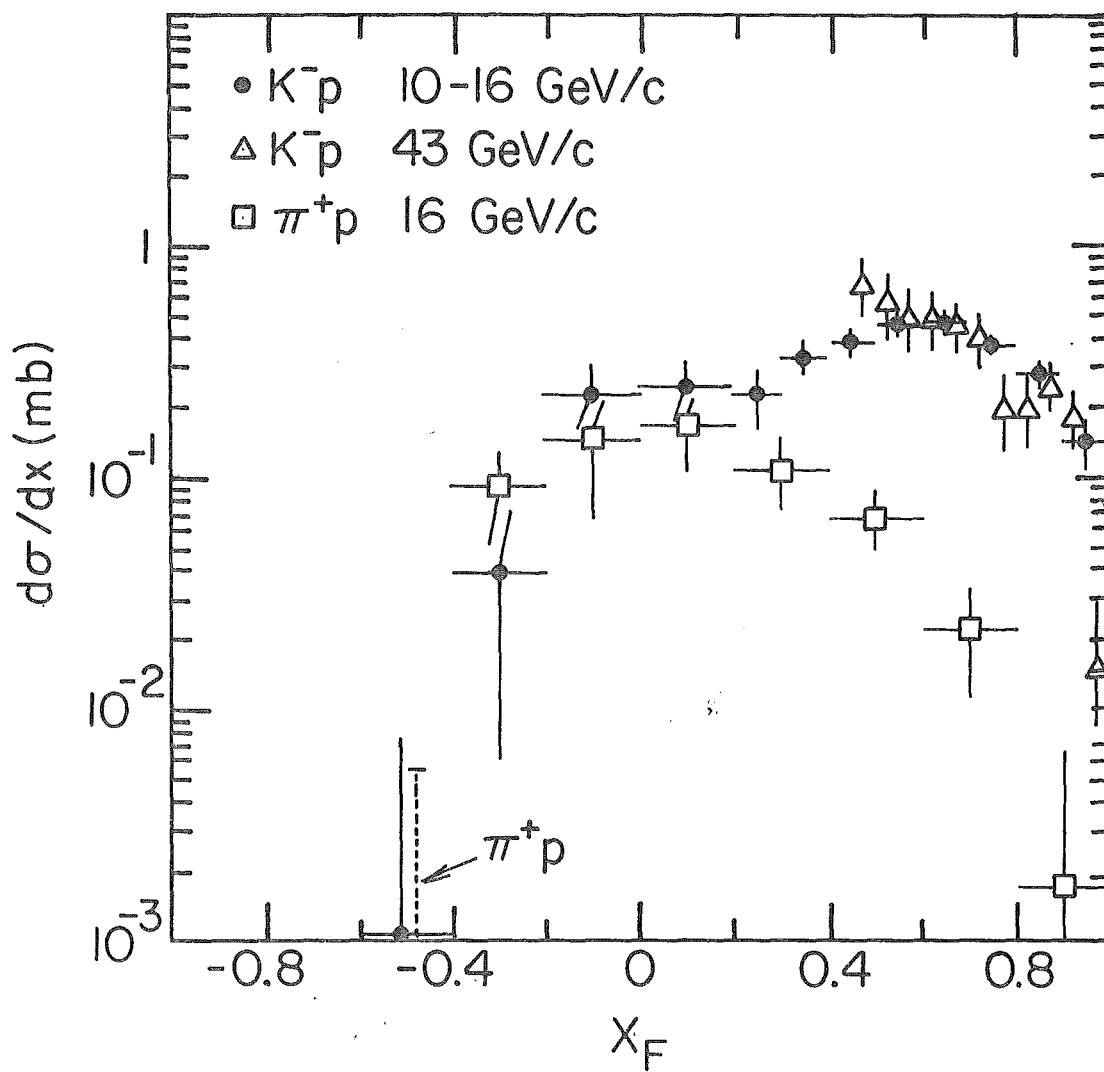


Figure 5.13. $d\sigma/dx_F$ for ϕ 's produced from incident pions and kaons. (Reproduced from Sixel (1982).)

Using the assumption of isotropic decays in the rest frame of the ω and ϕ in the Monte Carlo described in section 5.3, the ω/ϕ acceptance ratio in the $0.1-0.25 x_F$ band is found to be 0.50. Tentative indications of a possible $1 + \cos^2\theta_{GJ}$ angular dependence (where θ_{GJ} is the Gottfried-Jackson angle (Gottfried and Jackson, 1964)) have been reported for the ω and ϕ decays (Abolins, 1978). We find, however, that the ω/ϕ acceptance ratio does not change significantly ($< 0.2\%$) when a $1 + \cos^2\theta_{GJ}$ angular distribution is assumed simultaneously for the ω and ϕ .

The possibility that the feed-down and direct ω 's have different angular distributions was also considered. Based on this assumption, and on the uncertainties in the measurement of the positions of the M counters, the worst-case error on the ω/ϕ acceptance ratio was determined to be $\pm 8\%$.

A value for the branching ratio of $\omega \Rightarrow \mu^+\mu^-$ is not currently listed by the PDG. $BR(\omega \Rightarrow e^+e^-)$ is known, however, and is given as $0.0072 \pm 0.0007\%$. The assumption of $e-\mu$ universality, that the muon and electron couple identically to the photon, provides a relationship between the $\mu^+\mu^-$ and e^+e^- decays, the difference arising only in the phase space of the two decay channels. Using the calculations of Van Royen and Weisskopf (1967) we find $BR(\omega \Rightarrow \mu^+\mu^-) = 0.9979 \cdot BR(\omega \Rightarrow e^+e^-)$, or essentially no difference in the two

branching ratios.

° Taking into account, then, the branching ratios of $\omega \Rightarrow \mu^+\mu^-$, $\phi \Rightarrow \mu^+\mu^-$, the ω/ϕ acceptance ratio, and the ω and ϕ yields in the central region, we obtain $(\phi/\omega)_{CENTRAL} = 0.061 \pm 0.018$. We then solve for λ in the equation

$$(\phi/\omega)_{CENTRAL} = \frac{3\lambda^2}{3 + (10.6 + 2.2\lambda)\alpha}$$

using the relationship between the relative central ω and ϕ yields discussed in section 4.2. We use the value $\alpha = 0.13 \pm 0.03$ for the $L=1$ suppression, as discussed in section 5.4. We obtain, finally, $\lambda = 0.31 \pm 0.05$.

We have seen that assuming a non-isotropic angular distribution does not change this result. The value of λ is also rather insensitive to the x_F values used to define the central region. To take an extreme case, requiring that $0.1 \leq x_F \leq 0.5$ does not change λ within the error quoted above.

A more serious complication is the effect of possible $\rho^0 - \omega$ interference on the area of the ω peak. Using a simplified model, we have calculated the contribution of an interference term to the measured ω yield (appendix D). We find that in the worst case, the effect of interference could change our value of λ by $+0.03/-0.05$, i.e. $+10\%/-16\%$ of the value derived above.

Now that a value of λ has been obtained, we need to compare it with the world data on strangeness suppression. This is the subject of the next chapter.

CHAPTER 6

DISCUSSION AND CONCLUSIONS

We have derived a value for the strangeness suppression factor λ from our data using the methodology suggested by the model discussed in chapter 4. The measurement of λ described here is unique insofar as it is the first to have been performed using the ϕ/ω production ratio.

The model predicts that λ is independent of the hadronic system from which the strange quarks are produced. In this chapter we compare our value with those obtained in a variety of other experiments, as another test of the universality of λ .

Table 6.1 is a compilation of the world data on λ as measured in hadron-hadron inclusive processes. (The values in tables 6.1 and 6.2 are taken from the survey article of Malhotra and Orava, 1983.) The quantity λ' is defined as the strangeness suppression factor obtained if the feed-down contributions are ignored, i.e. as if all particles measured were directly produced. This is included as an indication of the size of the correction, typically 10-20%. The last line of the table refers to the present experiment.

<u>METHOD</u>	<u>\sqrt{s} (GeV)</u>	<u>λ'</u>	<u>λ</u>
pp \Rightarrow K^*/ρ	4.9	0.12 ± 0.02	0.13 ± 0.02
pp \Rightarrow K^*/ρ	6.8	0.15 ± 0.02	0.16 ± 0.02
pp \Rightarrow K^*/ρ	11.4	0.28 ± 0.12	0.31 ± 0.12
pp \Rightarrow K^*/ρ	19.7	0.18 ± 0.11	0.20 ± 0.11
pN \Rightarrow $\Lambda \bar{\Lambda} / p \bar{p}$	21.3	0.25 ± 0.04	0.25 ± 0.04
pp \Rightarrow K^*/ρ	27.6	0.31 ± 0.08	0.34 ± 0.08
pp \Rightarrow K^{*0}/f	52.5	0.30 ± 0.10	0.30 ± 0.10
pp \Rightarrow K^*/ρ	52.5	---	0.35 ± 0.12
pp \Rightarrow ϕ / K^*	52.5	0.30 ± 0.11	0.36 ± 0.13
pp \Rightarrow K^*/ρ	63.0	0.29 ± 0.05	0.32 ± 0.06
pp \Rightarrow K^*/ϕ	63.0	0.30 ± 0.07	0.36 ± 0.08
pp \Rightarrow ϕ / ρ	63.0	0.30 ± 0.03	0.32 ± 0.03
$\pi^+p \Rightarrow$ K^*/ρ	5.6	0.26 ± 0.08	0.29 ± 0.09
$\pi^+p \Rightarrow$ K^*/ρ	5.6	0.26 ± 0.10	0.29 ± 0.11
$K^-p \Rightarrow$ ϕ / K^*	4.5	0.17 ± 0.03	0.20 ± 0.04
$K^-p \Rightarrow$ ϕ / K^*	5.6	0.17 ± 0.04	0.20 ± 0.05
$K^-p \Rightarrow$ ϕ / \bar{K}^{*0}	7.8	0.29 ± 0.09	0.35 ± 0.06
$K^+p \Rightarrow$ ϕ / K^*	7.8	0.20 ± 0.05	0.24 ± 0.06
$\pi^-N \Rightarrow$ ϕ / ω	20.6	0.25 ± 0.04	0.31 ± 0.05

Table 6.1. λ as measured in inclusive hadron-hadron interactions.

The results in table 6.1 are in reasonable agreement, with a weighted mean (excluding our measurement) of 0.30 ± 0.02 . No energy dependence is apparent (except possibly at very low energies), as can be seen from figure 6.1, a plot of λ vs \sqrt{s} for the values in table 6.1.

There is some question as to whether \sqrt{s} is the correct variable to consider in discussions of the energy dependence of λ . In particular, Malhotra and Orava suggest that the effective energy $\sqrt{s_{EFF}}$ of the parton-parton subprocess producing the mesons of interest, rather than the total center of mass energy \sqrt{s} is the quantity which is important here.

The problem is that any definition of effective energy would depend on the model used to extract λ . For the assumption of central hadron production from a quark-antiquark gas the energy of the gas would seem to be the appropriate quantity. It is not at all clear, however, without additional assumptions, how to obtain $\sqrt{s_{EFF}}$ in this case.

Strange quark suppression is observed in other processes as well. Table 6.2 is a compendium of values of λ as deduced from particles produced in $e^+ e^-$ and lepton-nucleon collisions, and from the ratio $BR(\psi \Rightarrow K \bar{K}^* + \bar{K} K^*) / BR(\psi \Rightarrow \rho \pi)$. Again, a general agreement is found, without any significant energy dependence. The overall mean

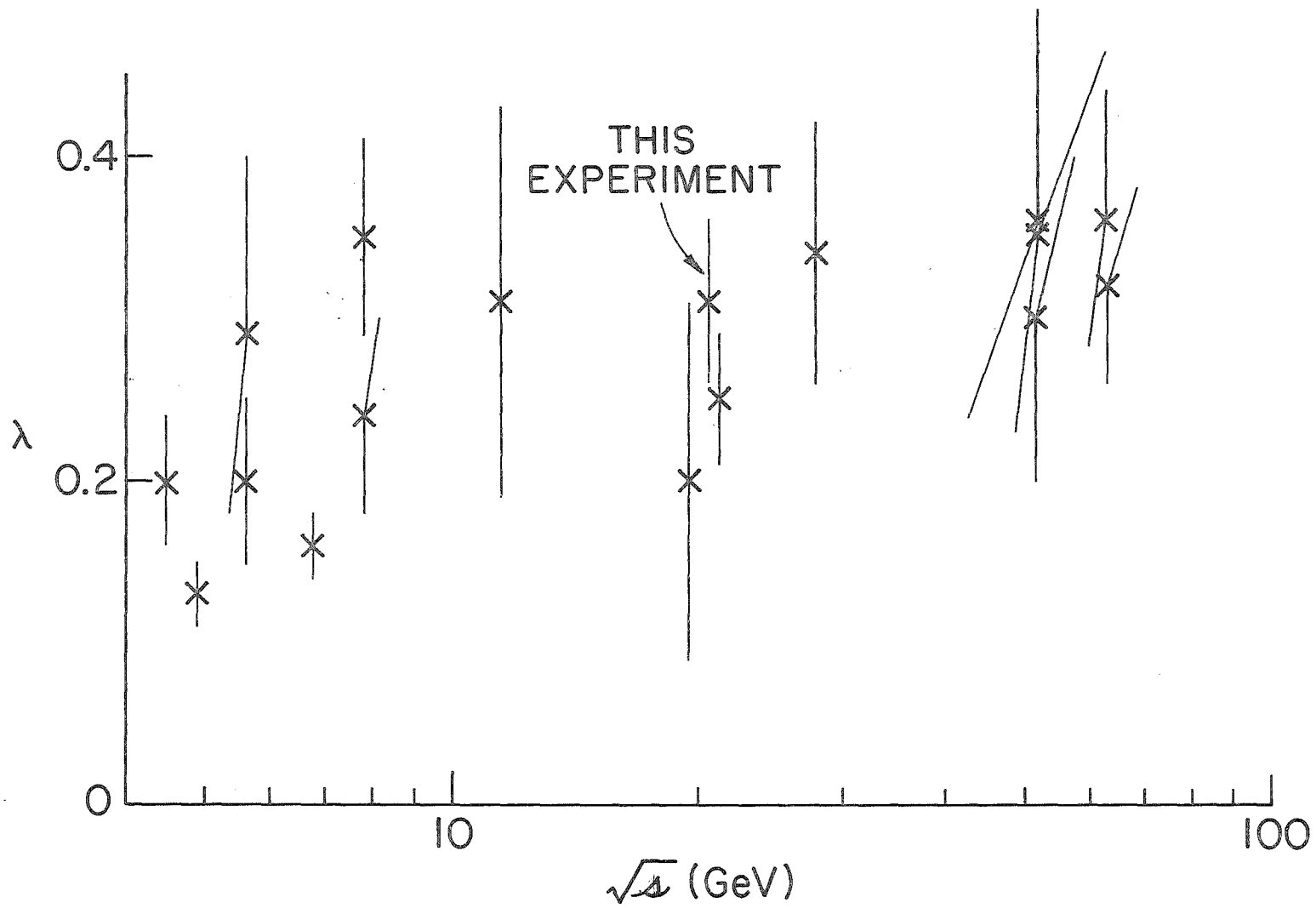


Figure 6.1. The strange quark suppression factor λ vs \sqrt{s} as derived from hadron-hadron interactions.

<u>METHOD</u>	<u>\sqrt{s} (GeV)</u>	<u>λ</u>
$e^+ e^- \Rightarrow K / \pi$	5.0	0.38 ± 0.08
$e^+ e^- \Rightarrow K / \pi$	33.0	0.30 ± 0.10
$e^+ e^- \Rightarrow K / \pi$	34.0	0.33 ± 0.12
$e^+ e^- \Rightarrow \Lambda \bar{\Lambda} / p \bar{p}$	6.6	0.18 ± 0.13
$e^+ e^- \Rightarrow \Lambda \bar{\Lambda} / p \bar{p}$	29.0	0.19 ± 0.10
$e^+ e^- \Rightarrow \Lambda \bar{\Lambda} / p \bar{p}$	33.0	0.27 ± 0.14
$e^+ e^- \Rightarrow \Lambda \bar{\Lambda} / p \bar{p}$	34.0	0.18 ± 0.12
$e N \Rightarrow K / \pi$	4.6	0.26 ± 0.04
$\bar{\nu} N \Rightarrow K / \pi$	5.0	0.27 ± 0.04
$\psi \Rightarrow K^* K / \rho \pi$	3.1	0.36 ± 0.14

Table 6.2. λ as measured by methods other than hadron-hadron interactions.

value of λ computed from the data in tables 6.1 and 6.2 is 0.29 ± 0.02 , compared with our value of 0.31 ± 0.05 .

To conclude, then, the value of the strangeness suppression constant λ measured in this experiment is in good agreement with the world data. Further work needs to be done in this field-- in particular, on the universality of the tensor meson suppression factor α , and the refinement of the measured branching ratios used in determining the feed-down corrections. Progress in this area has been hampered by the difficulties involved in the study of inclusive hadronic tensor and pseudovector meson production. Nevertheless, it is clear that overall, the data are in agreement with simple quark model predictions which assume a universal strange quark suppression factor.

APPENDIX A
THE CHERENKOV COUNTER

A.1 Introduction

The Cherenkov counter operates on the basis of the effect discovered by P. A. Cherenkov (Cherenkov, 1934) and subsequently interpreted theoretically by I. M. Frank and I. E. Tamm (Frank and Tamm, 1937). A charged particle moving in a transparent medium with a velocity larger than the phase velocity of light in that medium radiates along a conical wavefront. The angle θ_c of emission of the radiation with respect to the path of the particle is given by the relation

$$\cos \theta_c = 1/\mu\beta$$

where μ is the index of refraction of the medium, and $\beta = v/c$ is the usual Lorentz parameter of the radiating particle. The energy radiated per unit path length by a particle of unit charge is

$$\frac{dE}{ds} = \frac{e^2}{c^2} \int_{\mu\beta > 1} \left(1 - \frac{1}{\mu^2\beta^2}\right) \omega d\omega .$$

The property of Cherenkov radiation that is exploited here as a means of particle identification is the dependence of θ_c and dE/ds on the velocity but not the mass of the particle. The momenta of charged tracks are determined from the track reconstruction; thus, the β dependence of the radiation can in principle be used to distinguish between particles of equal momenta but different masses.

The relationship between the angle of emission and the velocity is of particular significance. Since $\cos \theta_c < 1$, it implies that a particle radiates only for $\beta > 1/\mu$. Thus in a given medium a momentum threshold exists

$$p^{TH} = m(\mu^2 - 1)^{-1/2}$$

below which a particle of mass m does not radiate. This property can be used to choose between differing mass hypotheses m_1, m_2 ($m_2 > m_1$) for a given track of momentum p , provided $p_1^{TH} < p < p_2^{TH}$. It is this principle which is employed in the threshold Cherenkov counter.

A.2 The E610 Cherenkov Counter

The Cherenkov counter used in E610 was originally built by Oxford University for the E398 muon collaboration. The existing system was upgraded and modified for E610 by the University of Illinois. The radiator path was doubled, and a new LED-pulser system for calibration

and gain monitoring was implemented. In addition, the mirrors were reconfigured to provide a vertical gap through which noninteracting beam particles could pass, and a complete realignment of the mirror optics was performed.

A more complete description of the Cherenkov counter is found in the thesis of J. Proudfoot (Proudfoot, 1978). What follows is a summary of its configuration, with attention given to the changes made for E610.

The physical layout of the Cherenkov counter is shown in figure A.1. A steel frame was covered on the four sides parallel to the beam by sheet aluminum, while the upstream and downstream windows were opaque mylar of thickness 0.5 mm. The overall dimensions of the box were 600 cm (x) x 250 cm (y) x 300 cm (z). A hatch on the side made access possible. The box was made gas- and light-tight by caulking all joints with RTV silicone rubber sealant, and the interior was painted flat black to eliminate stray reflections.

The Cherenkov light was collected by eighteen spherical mirrors mounted in two rows of nine at the downstream end of the box, as shown in figure 2.4. The mirror plane was located at $z = +700$ cm, and the total length of the radiator (distance between the upstream wall and the mirror plane) was then approximately 260 cm. The mirrors were 6 mm cast lucite sheets of dimensions 60 cm x 110 cm, with a 200 cm

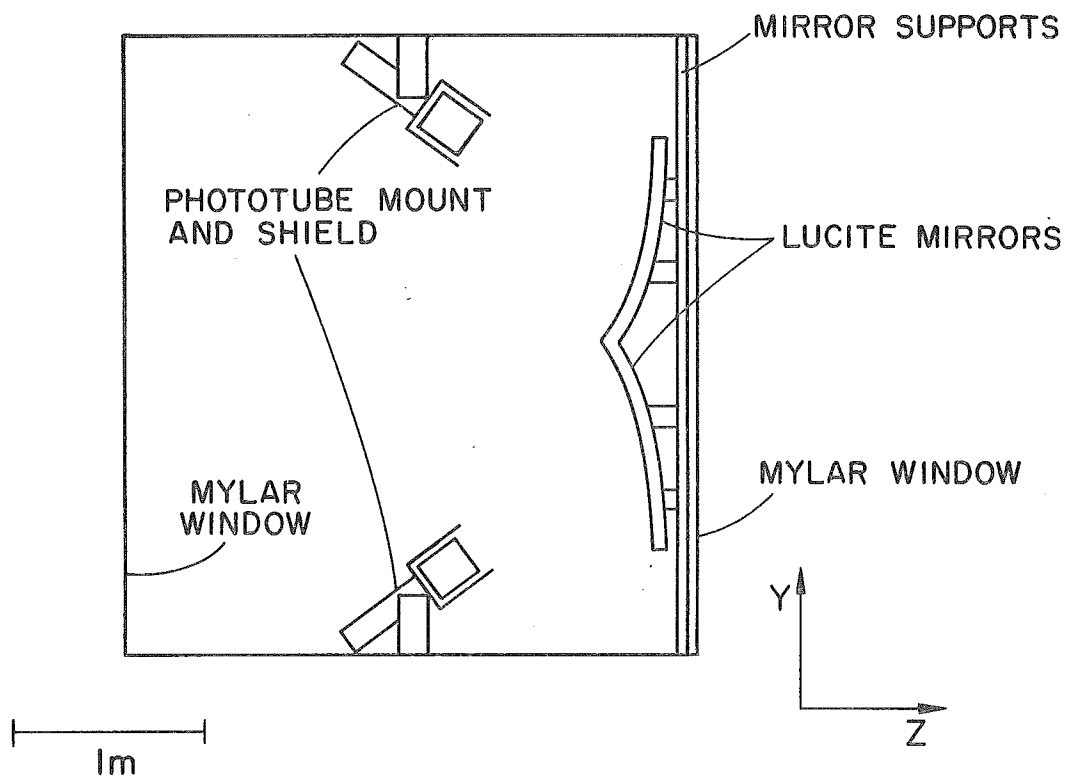


Figure A.1. The E610 Cherenkov counter.

radius of curvature, and with a thin film of aluminum deposited on the front surface. The mirror reflectivities were measured to be $> 90\%$ at 6238 \AA .

The light incident on each mirror was focussed onto a RCA 4522 photomultiplier tube mounted at the apex of a 30° Winston cone. The photomultiplier bases were simple Zener-regulated resistive chains.

The optical alignment of the mirrors presented no particular difficulties. In the y-z (nonbending) plane, tracks originate from a point source at the target, while in the bending (x-z) view, the secondaries appear to originate from an extended source at the center of the magnet.

A theodolite-mounted laser was placed at the center of the CCM. The point source in y was simulated by adjusting the angle and elevation of the laser. The alignment was then effected by sweeping the laser beam across the top, center and bottom of each mirror and adjusting the mirror position until all the reflected light was observed to be incident on the photocathode of that cell's photomultiplier.

To facilitate the high voltage and bucking current settings, as well as to provide continuous gain monitoring during the data acquisition, a reference light source was used. Colloquially known as

"Hydras", each consisted of three green LEDs feeding nine fiber optic light guides, which in turn were placed inside the Winston cones. The two hydras were driven by the E398 Daresbury avalanche pulser, which delivered a 30 V, 12.5 ns wide pulse to each Hydra.

The fringe field of the CCM presented a problem for photomultiplier operation even as far downstream as the lead glass array. To alleviate this, a three-part shielding system was used in the Cherenkov counter. A cylinder of mu-metal 6 mm thick surrounded the Winston cone and photocathode. Around this in turn was mounted a cylinder of "conetic" shielding (Perfection Mica, 1976). By themselves these provided insufficient protection; the residual fringe field as measured by a Hall probe was ~ 1 G. The shielding was completed by a 1000 turn bucking coil surrounding the photocathode and dynodes. The bucking current could be adjusted separately for each cell-- the correct settings were arrived at by observing on an oscilloscope the current which maximized the LED signal from each cell.

The signal from each of the phototubes was read out by a LRS 2249A 10 bit analog-to-digital converter (ADC). The ADC added a reference level (pedestal) to the current pulse from the photomultiplier, and integrated over the 60 ns gate supplied by the trigger. This charge, in units of 0.25 pc, was recorded on tape for

each cell. In the case of the eight central cells, the signal was first passively split in order that a test trigger ("charged-K") could be formed.

The ADC pedestals were set in the 10-40 channel range. Most pedestals had a width of 2-3 channels, except for cells 14-15, which demonstrated an intensity dependent pedestal broadening. Apparently the transverse spread of the beam was larger than originally anticipated, so that light from beam particles was also being picked up, tending to saturate the bases at the high intensities used for the dimuon data acquisition.

The high voltage in each cell was set by observing the pulse height distribution produced by the Hydra pulses. Since the light output of the fibers was small, nearly all the pulses above pedestal were due to one photoelectron, and the approximation

$$\langle A \rangle = \text{MEAN} - \text{PED}$$

could be used. Here $\langle A \rangle$ is the mean gain (channels/photoelectron), MEAN is the mean of the distribution of pulses above pedestal, and PED is the channel number of the pedestal. For the cells which demonstrated a one photoelectron peak the gain was determined directly from the position of the peak. The voltage was set such that $\langle A \rangle$ was in the range 20-40 channels/photoelectron. The cell voltages were in the 2300-2600 V range, with values for the central eight larger to

compensate for the splitting of the signal to the charged-K trigger.

The Cherenkov medium used was dry nitrogen at atmospheric pressure, with index of refraction $\mu = 1.00028$. The counter was purged with three volumes of N_1 , after which a trickle flow of gas was left on to replace losses from residual leaks.

A.3 Alignment and Calibration

The rough positions of the Cherenkov mirror boundaries were found by a survey at the time of the optical alignment of the mirrors. The accurate location of each mirror relative to the chambers, however, was determined in the analysis by the inefficiency scan method. For the x edges, tracks were used which fell within a software window about the nominal mirror position as shown in figure A.2a. This ensured that all the Cherenkov light from tracks falling within the window was contained inside the vertical boundaries of the cell. (6.0 cm is the radius of the $\beta = 1$ Cherenkov circle.) The mean inefficiency (counts in pedestal/total counts) in 1.0 cm vertical bands was plotted vs x for all tracks falling within the window. (The momentum cutoff of the CCM is approximately the same as the pion threshold in the Cherenkov (6 GeV/c) and since for alignment purposes only the relative efficiency across the cell is of interest, no momentum cut was made. The tracks were required to have associated drift chamber hits,

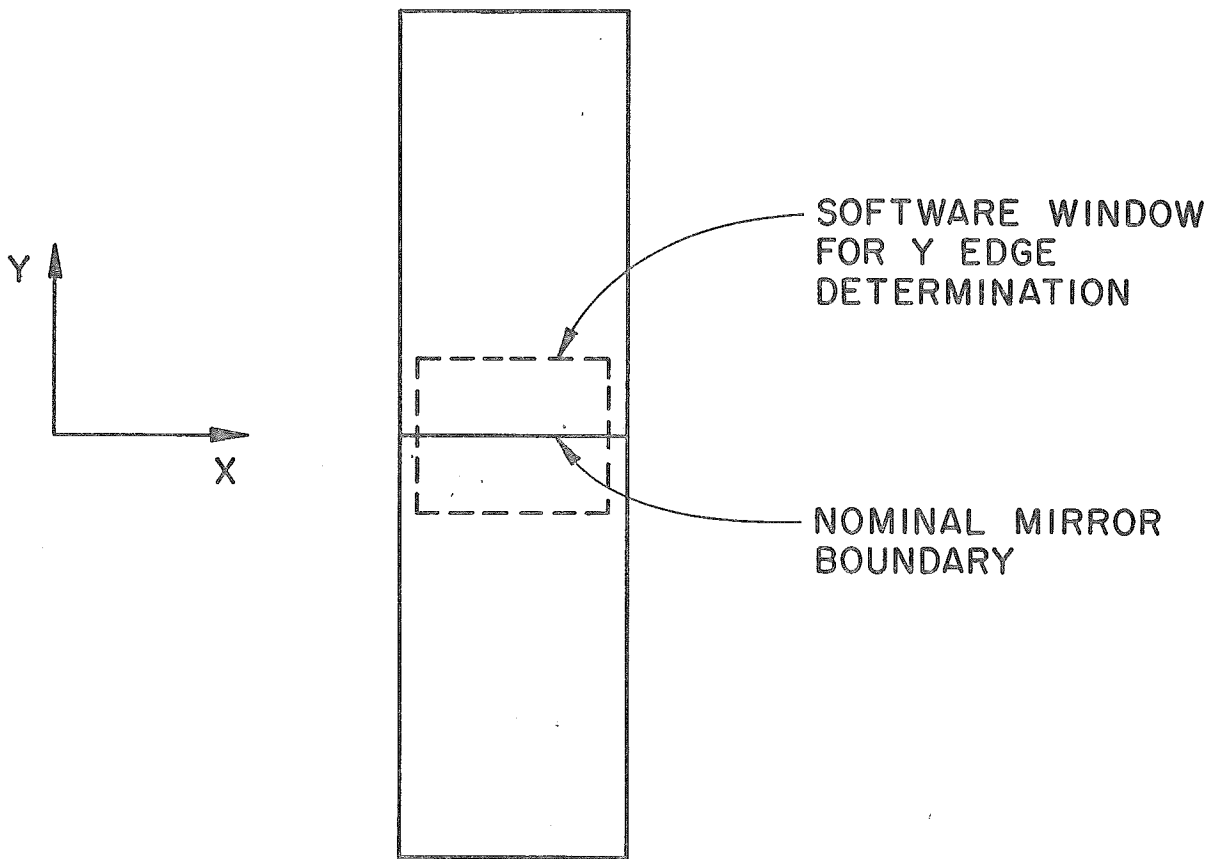
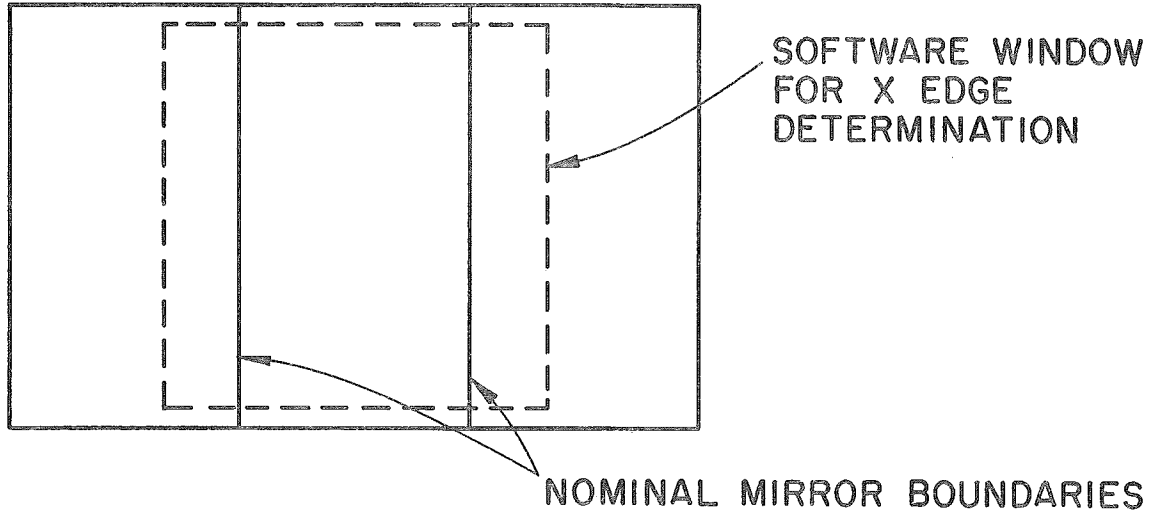


Figure A.2. Determination of cell boundaries in (a) x and (b) y.

however, thereby improving the accuracy of the extrapolated downstream track.) The y edges were determined in a similar fashion, using the window as in figure A.2b.

Results for a typical cell are shown in figure A.3. The mirror edges are clearly delineated. (The half-depth position is taken as the cell edge.) The method works for determining the x boundaries of all but the four outermost cells, where most tracks miss the drift chambers. The y edges farthest from the center are also not determined, again because of the incomplete drift chamber coverage. In this case, the extreme y edge was found from the position of the edge closest to the center and the nominal length (110 cm) of the mirror.

The low intensity of Cherenkov radiation means that in considering the relationship between the observed pulse height y and the intensity of the incident radiation, it is necessary to also take into account the statistics of the photomultiplication process (Sard and Smith, 1978). This relation is governed by two independent stochastic variables: n, the number of photoelectrons, and A_i , the gain for each photoelectron. Then

$$y = A_1 + A_2 + \dots + A_n \quad \text{for } n > 0$$

$$y = 0 \quad \text{for } n = 0$$

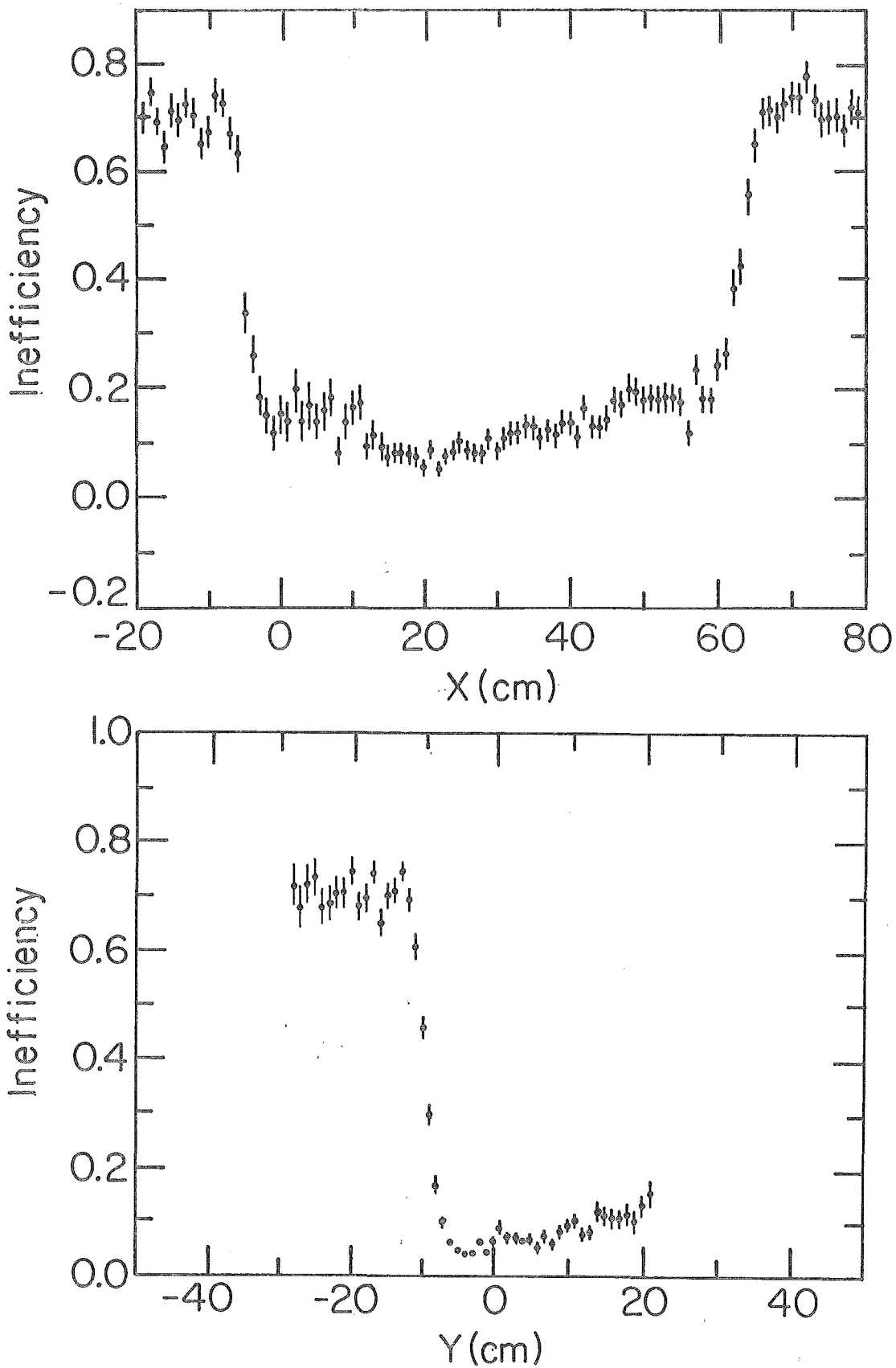


Figure A.3. Boundaries in (a) x and (b) y of a typical Cherenkov mirror as determined from the dimuon data.

The distribution of n is Poissonian, with mean value \bar{n} . The mean number of photoelectrons depends only on the intensity of the incident radiation at the photocathode. The statistics of A_i are somewhat more complicated, depending on the characteristics of the photomultiplier, the residual fringe field, and the electronics, but not on the incident intensity. The fluctuation of the gain is expected to be large (Allen, 1950) and must also be considered.

At this point it is useful to introduce a heuristic model of the response of the phototube. The distribution of A_i is approximated by a Gaussian, with mean $\langle A \rangle$ and standard deviation σ_A . The probability of measuring a pulse height between y and $y+dy$ given \bar{n} , $\langle A \rangle$, σ_A is then

$$P_{ROB}(y) dy = \sum_{n=1}^{\infty} e^{-\bar{n}} \frac{\bar{n}^n}{n!} \frac{1}{\sqrt{2\pi n \sigma_A^2}} \exp\left[-\frac{(y - n\langle A \rangle)^2}{2n \sigma_A^2}\right] dy.$$

This formula is due to Joel Butler (Sard and Smith, 1978; Avery, 1980).

The parameters $\langle A \rangle$, σ_A are treated as constants for a given cell. The mean number of photoelectrons \bar{n} will vary depending on the intensity of the incident light from event to event. For Cherenkov radiation, the Frank-Tamm intensity formula gives \bar{n} as a function of

μ , β , and $\bar{n}(\beta=1)$, the asymptotic value for extreme relativistic particles:

$$\bar{n}(\beta) = \bar{n}(\beta=1) (1 - 1/\mu^2 \beta^2) / (1 - 1/\mu^2).$$

By considering only light from single high momentum tracks, these parameters can be determined for each cell.

Pulse height distributions were produced for tracks satisfying the geometrical cut (light from the track completely contained in the cell, and no other tracks contributing light to that cell). In addition, the tracks were restricted to be muons, or hadrons with $p > 30$ GeV/c. Except for a small proton contamination (estimated to be $< 1\%$) these are effectively $\beta=1$ particles.

The observed pulse height distributions were fit to the Butler formula. Figure A.4 shows the fitted function superposed on the data for one cell. Typical values of $\bar{n}(\beta=1)$ are 5-7 photoelectrons (corresponding to efficiencies $(1 - e^{-\bar{n}})$ of $> 99\%$), while the values of $\langle A \rangle$ are in the range 20-40 channels/photoelectron.

At this point we are finally ready to use the Cherenkov counter for particle identification. The method is described in chapter 5.

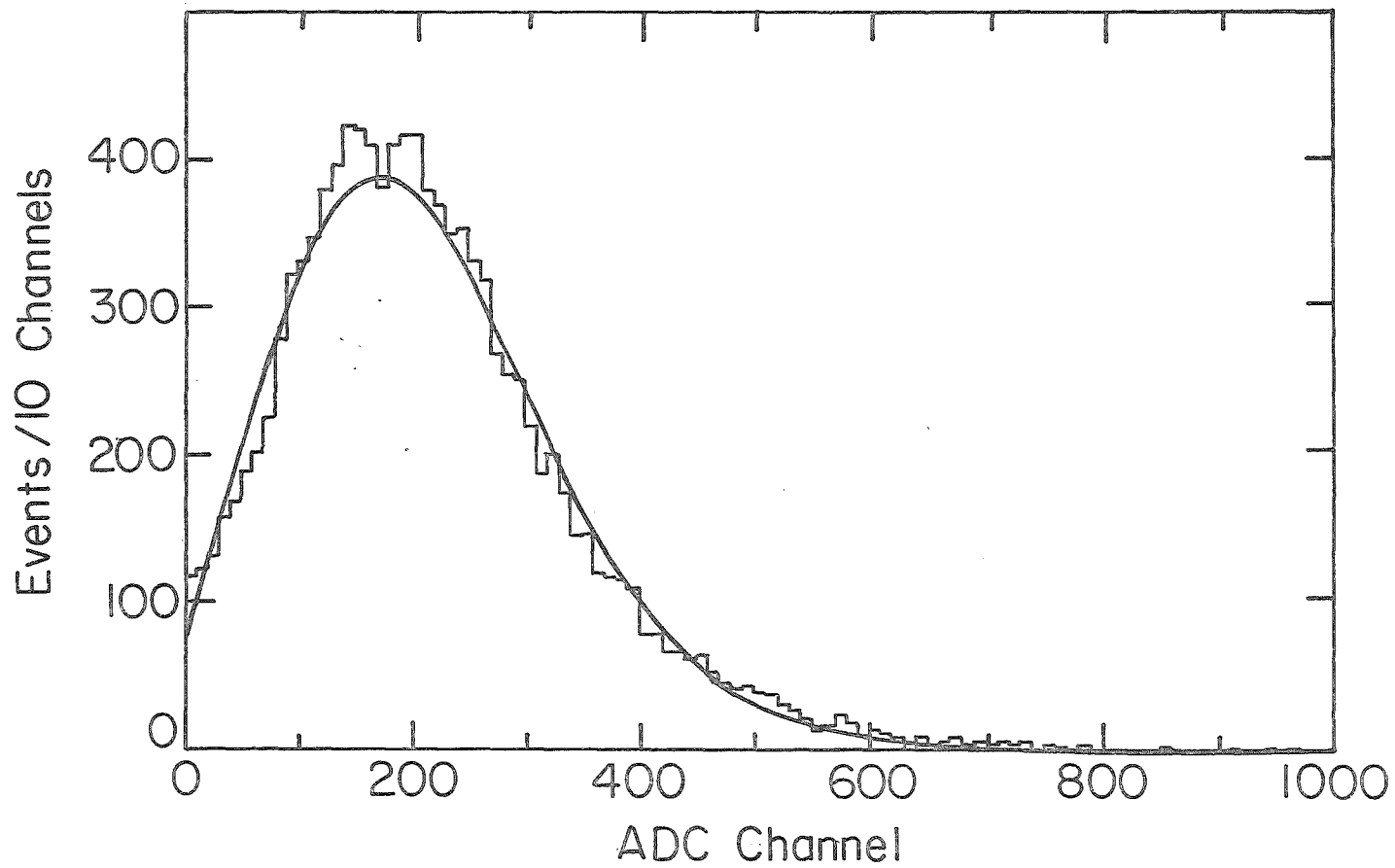


Figure A.4. Pulse height distribution for $\beta = 1$ tracks in a typical Cherenkov cell. The curve is a fit to the Butler formula (see text).

APPENDIX B
NEUTRAL STRANGE PARTICLES

B.1 Trackfinding

As described in chapter 3, the upstream track reconstruction was strongly biased towards tracks originating at the primary vertex. While this algorithm had the advantage of being quick, it was not useful for finding tracks from neutral vee decays (decays of neutral particles-- mainly K_S^0 , Λ and $\bar{\Lambda}$ -- into two charged tracks downstream of the target).

Although this decay signature is a means which Nature has provided for strange particle identification, the principal utility of this analysis is as a check on the magnet calibration, by comparison of our measurement of the K_S^0 mass with the accepted value. The Λ and $\bar{\Lambda}$ samples were small, and thus have been combined for the purposes of this appendix.

The first step, then, involved reconstructing upstream tracks in a manner independent of the primary vertex. This was done at the DST level, since, as described previously, all the MWPC information was already present in an unpacked form on the DST. Only three- and four-point tracks in the 80 cm chambers were reconstructed.

(Two-point tracks were considered reliable only if consistent with the primary vertex, and so were not used here.) The 80 cm y tracks were used as roads into the U of I y planes to pick up additional hits, and were refit if any were found. The new set of upstream tracks was then fed to the main upstream trackfinder, as detailed in section 3.3. Finally, the global fit (section 3.5) was performed on the fully reconstructed tracks.

B.2 Neutral Vee Reconstruction

The identification of secondary neutral vertices (oppositely signed pairs of tracks with common spatial origins) was relatively straightforward once the tracks had been found. The distance of closest approach (DCA) of all oppositely charged pairs of tracks was calculated, along with the spatial coordinates of the neutral vertex (XV, YV, ZV). Figures B.1 and B.2 show the distributions of ZV and DCA. (All results in this appendix are from the UHI trigger sample.) The peak in figure B.1 corresponds to the position of the target.

The signature of a neutral vee is a neutral vertex of non-zero opening angle occurring downstream of the primary vertex. As is clear from figure B.1, most neutral pairs are target associated, in the sense that they could come from an interaction in the target. We

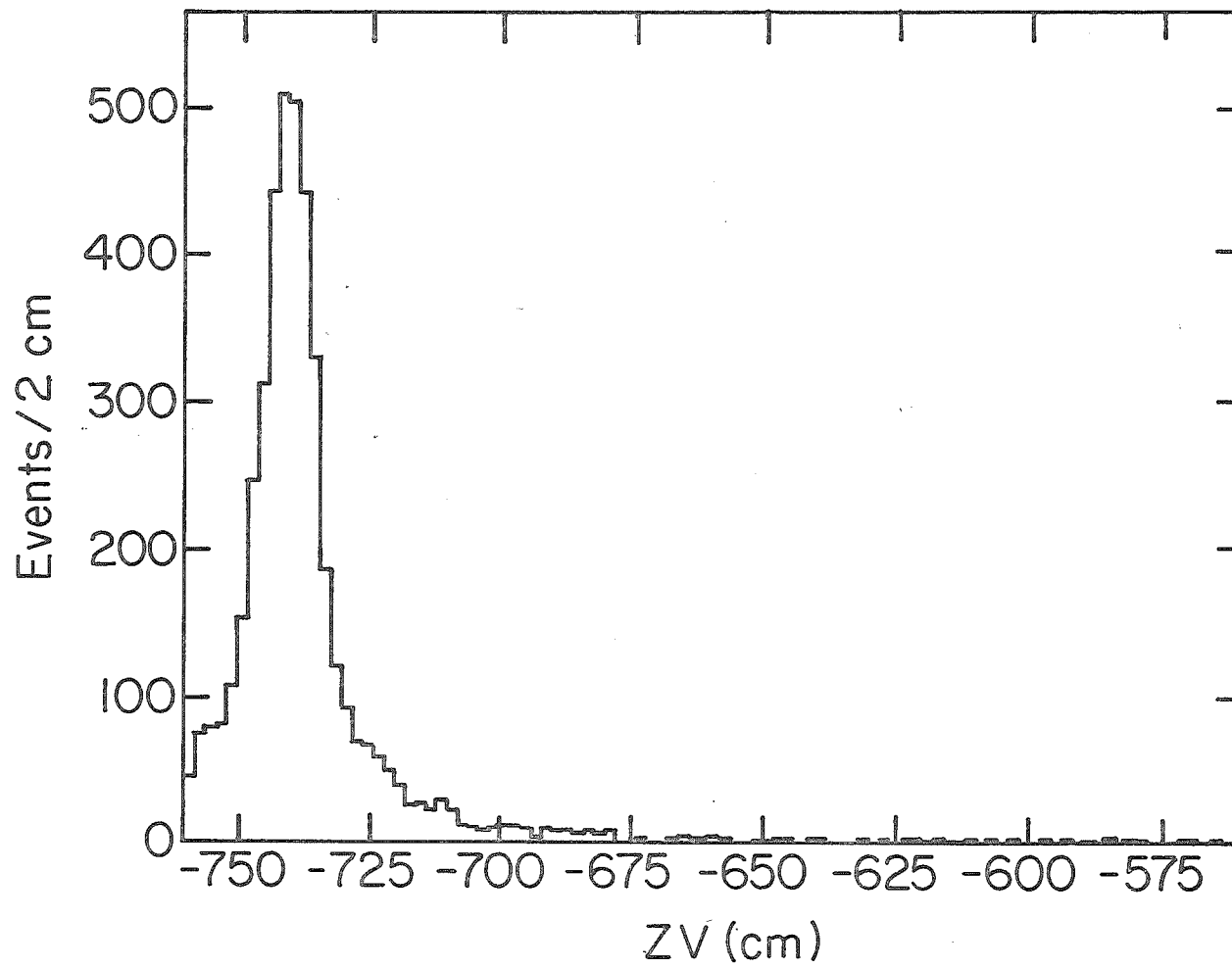


Figure B.1. Vertex distribution of neutral pairs.

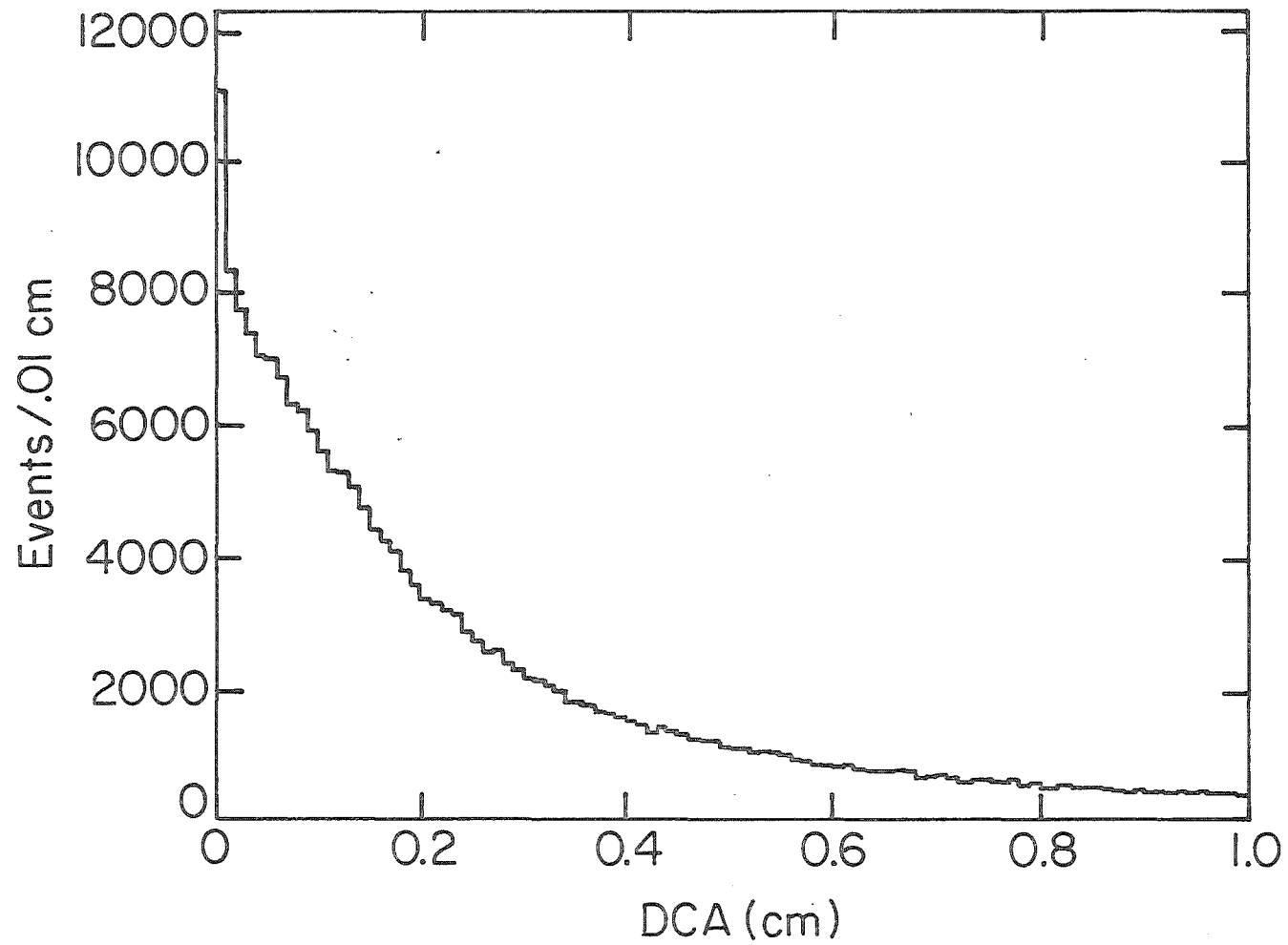


Figure B.2. Distance of closest approach for neutral pairs.

require that the neutral vertex be at least 10cm downstream of the target center to be considered a neutral vee candidate.

The DCA is required to be $< 1\text{cm}$. This is a relatively weak cut, since all pairs from the primary vertex will have a small DCA. The principal utility of this cut is to eliminate spurious vees resulting from halo muons or secondary interactions.

Finally, the momentum of the pair was required to point back to within 0.55 cm of the primary vertex, to ensure that the two-body decay candidate did indeed originate there. The resultant momentum vector was drawn through the presumed decay point, and extrapolated back into the target. Figure B.3 shows the distribution of the square of the distance from the primary vertex of the extrapolated momentum, for vees satisfying the DCA and ZV cuts.

Figure B.4 is the resulting mass spectrum, under the hypothesis that each prong of the neutral vee is a pion. A clear K_S^0 signal is apparent. Fitting to a Gaussian plus exponential background, we find the mass of the K_S^0 to be $497.5 \pm 0.4 \text{ MeV}/c^2$, with a FWHM of $13.7 \pm 0.1 \text{ MeV}/c^2$. This is in good agreement with the PDG mass value of $497.67 \pm 0.13 \text{ MeV}/c^2$.

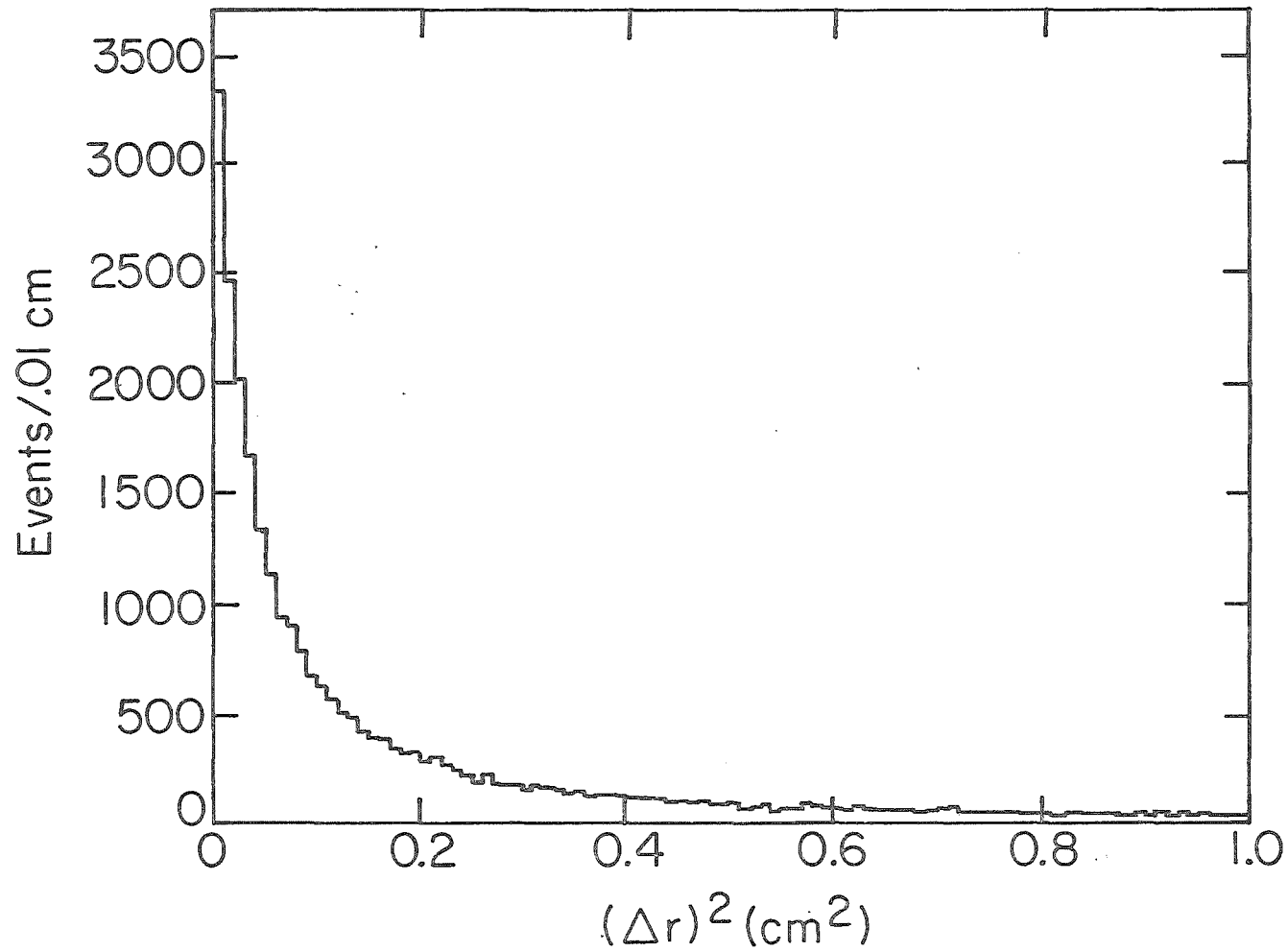


Figure B.3. Squared deviation of extrapolated neutral pair momentum to primary vertex.

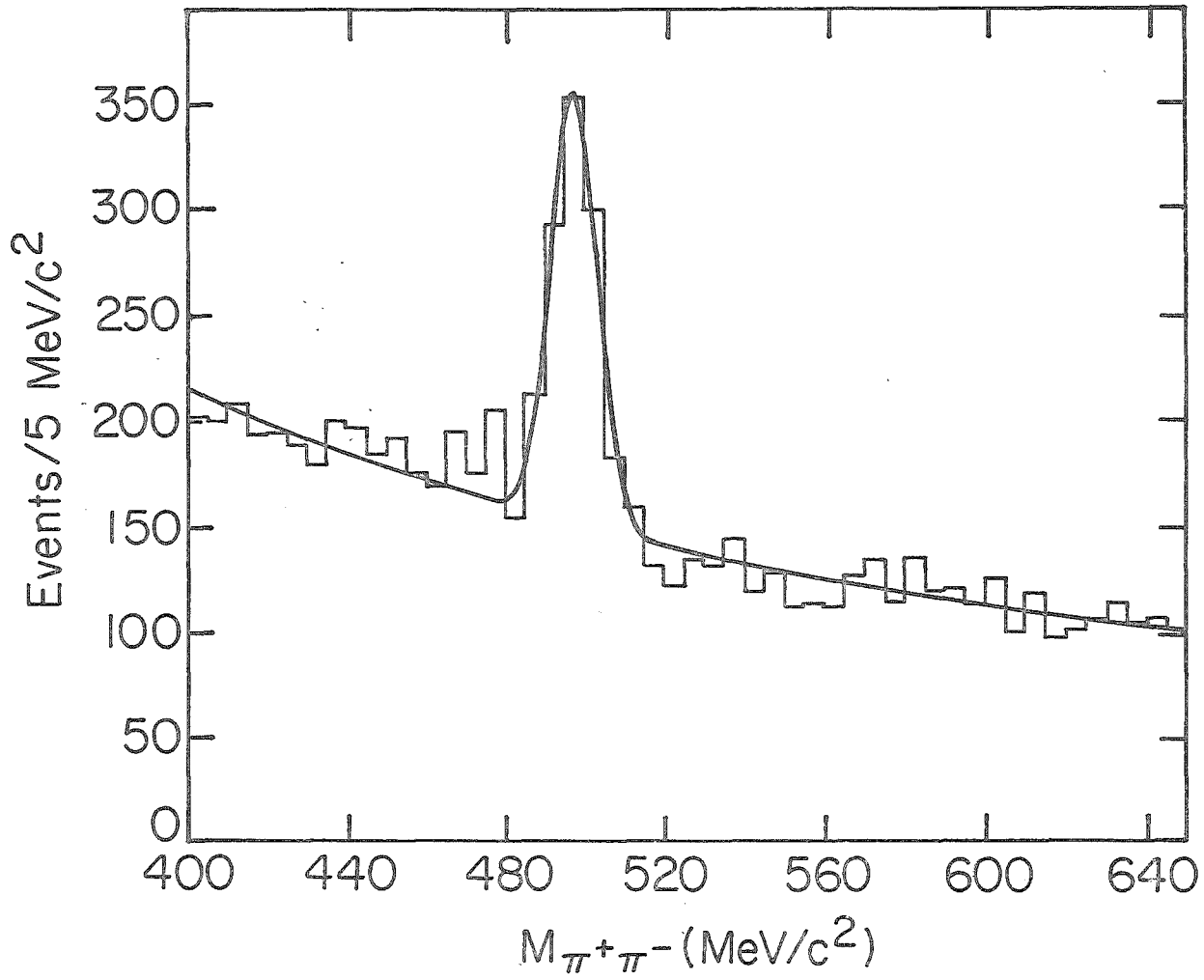


Figure B.4. Neutral vee mass spectrum, $\pi^+\pi^-$ hypothesis.

Assigning the proton mass to the track in each pair with the largest momentum, the combined $p\pi^-$ and $\bar{p}\pi^+$ spectra are shown in figure B.5. The $\Lambda/\bar{\Lambda}$ peak occurs at a mass of about $1115 \text{ MeV}/c^2$.

In both figure B.4 and B.5, events were removed which were possible kinematic reflections. These were vees which lay in the K_S^0 or Λ mass region for the alternative mass hypothesis.

A variety of cuts were tried in order to improve the signal-to-noise (S/N) of the K_S^0 and Λ . The most efficacious was simply to tighten the cut on the z position of the neutral vertex downstream of the target. Figure B.6 shows the effect on the K_S^0 of requiring $ZV > -721 \text{ cm}$ (20 cm downstream of the target). The S/N is improved by 120%, although 16% of the events in the peak are lost. Similar results are obtained for the Λ (figure B.7).

B.3 Efficiencies and Yields

The K_S^0 acceptance was calculated by generating neutral kaon decays according to $d^3\sigma/dp^3 \sim (1-x_F)^A e^{-B p_{\perp}}$. The parameters $A=8.0$, $B=4.6 \text{ (GeV}/c)^{-1}$ were chosen to reproduce the x_F and p_{\perp} distributions measured in $147 \text{ GeV}/c \pi^-p$ interactions (Brick, 1979). The calculated acceptance is in fact relatively insensitive to the precise values chosen for A and B. The acceptance for the $K_S^0 \Rightarrow \pi^+\pi^-$ decay was

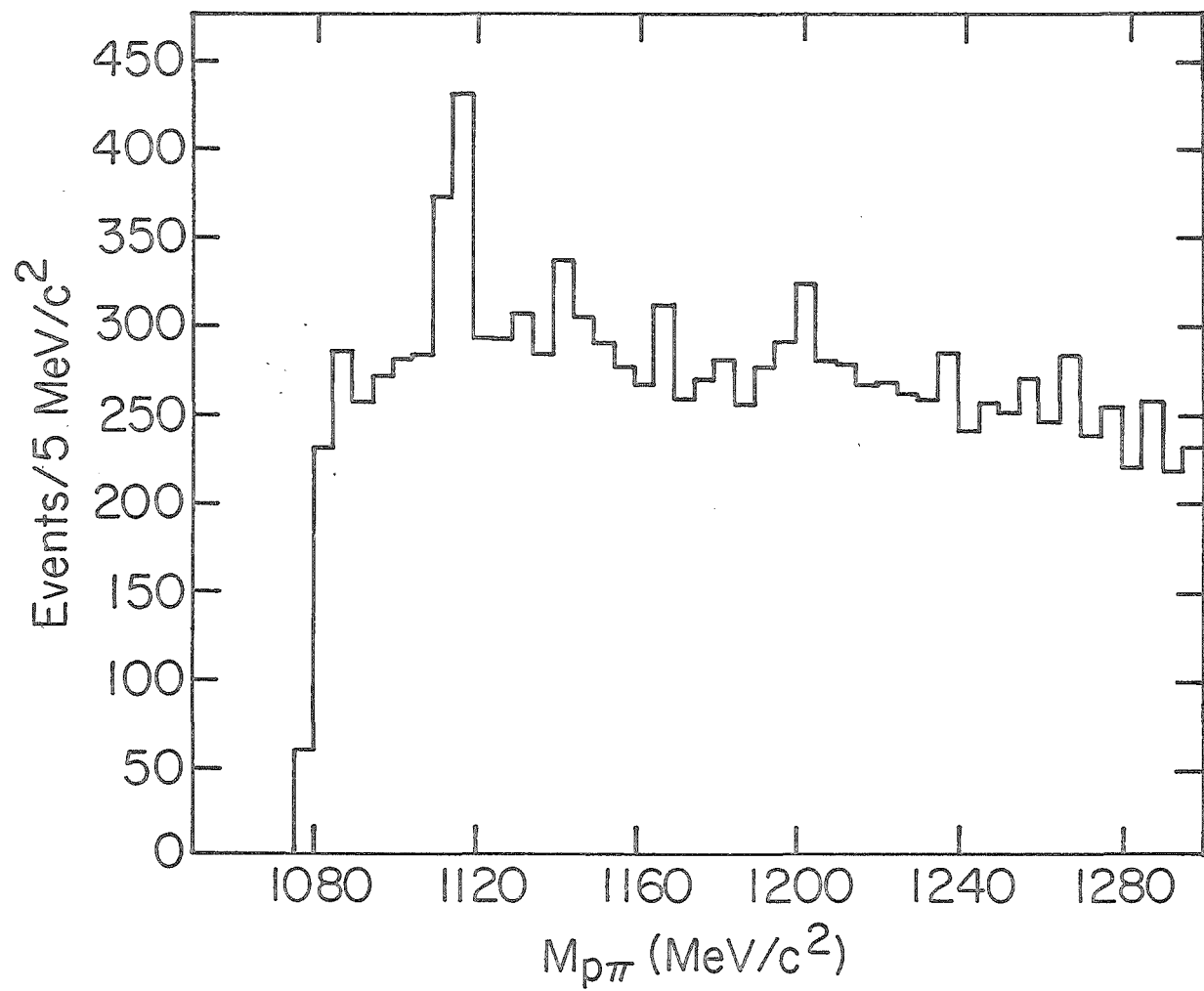


Figure B.5. Neutral vee mass spectrum, τp hypothesis.

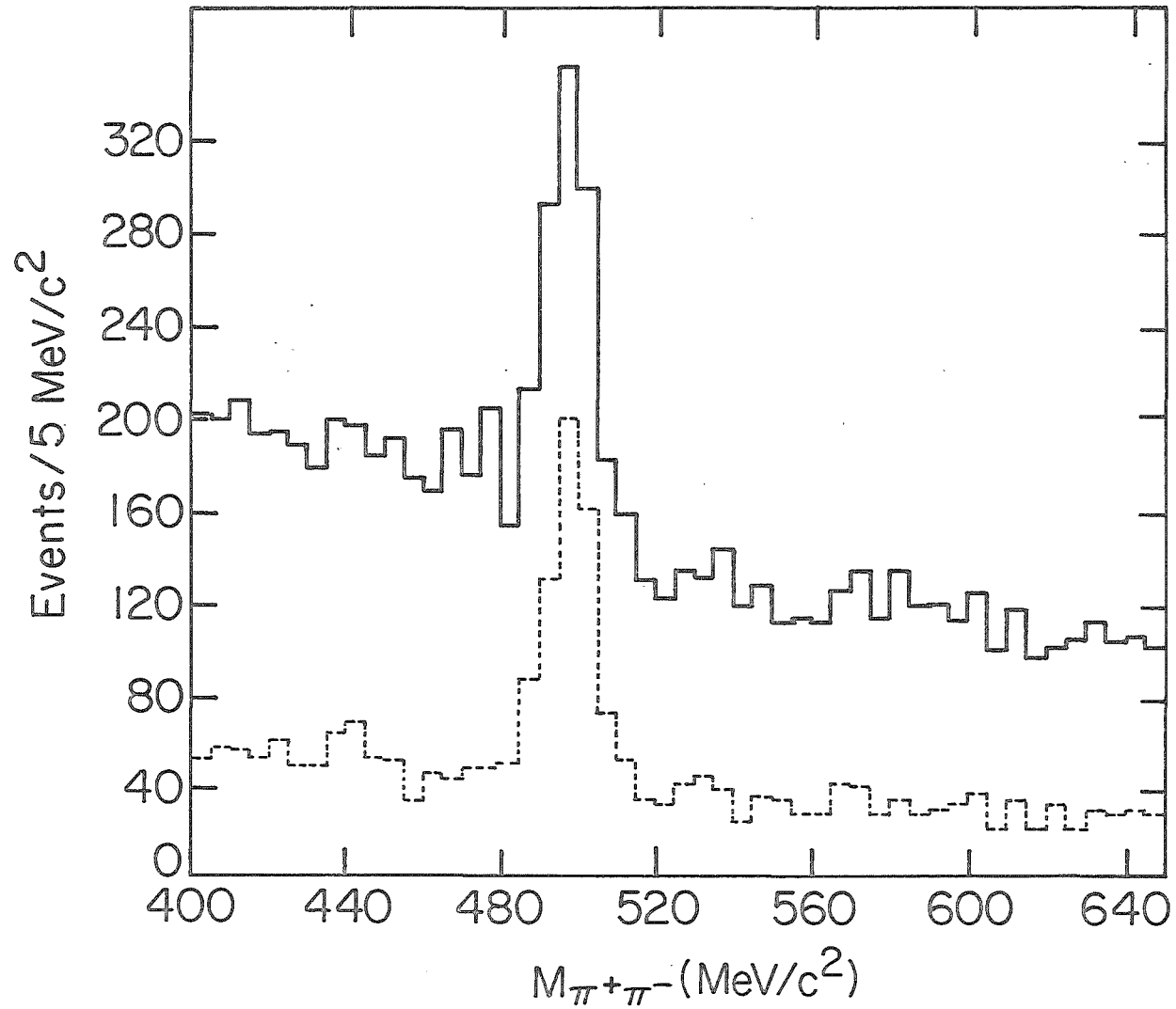


Figure B.6. Effect of vertex cut on K_S^0 signal. Solid curve: $ZV > -731 \text{ cm}$. Dashed curve: $ZV > -721 \text{ cm}$.

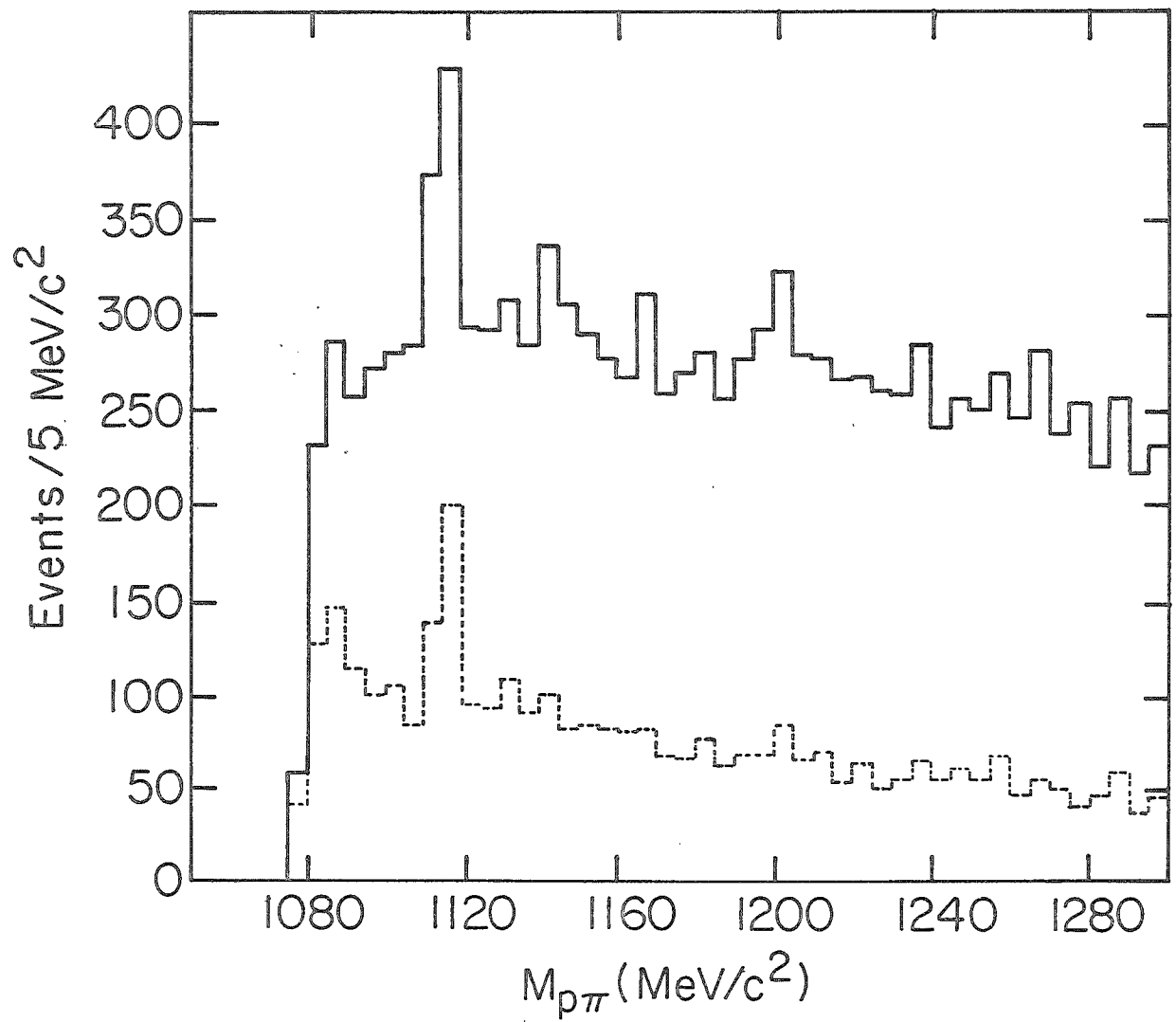


Figure B.7. Effect of vertex cut on Λ signal. Solid curve: $ZV > -731$ cm. Dashed curve: $ZV > -721$ cm.

found to be 0.26.

The inclusive cross section for K_S^0 production in 205 GeV/c π^-p interactions is 3.74 ± 0.24 mb (Ljung, 1977). The K_S^0 yield, predicted on the basis of this cross section and the acceptance determined above, was compared with that observed in the UHI (interaction trigger) data. Assuming that any short fall is due to loss in reconstruction, we find a reconstruction efficiency of about 80%.

B.4 K_S^0 and Λ Lifetimes

Another check on the neutral vee reconstruction algorithm is the measurement of the K_S^0 and Λ lifetimes. Again, UHI data were used.

The distribution of proper decay lengths x^{**} ($=c\tau^{**}$, with τ^{**} the proper lifetime of the neutral vee) was produced for events in the signal region of the mass spectrum, and the background from events in adjacent control bands was subtracted. The resulting distributions were corrected for acceptance and fit to the form $\exp(-x^{**}/x_0^{**})$, with x_0^{**} the mean proper decay length. These are shown in figures B.8 and B.9 for the K_S^0 and Λ respectively.

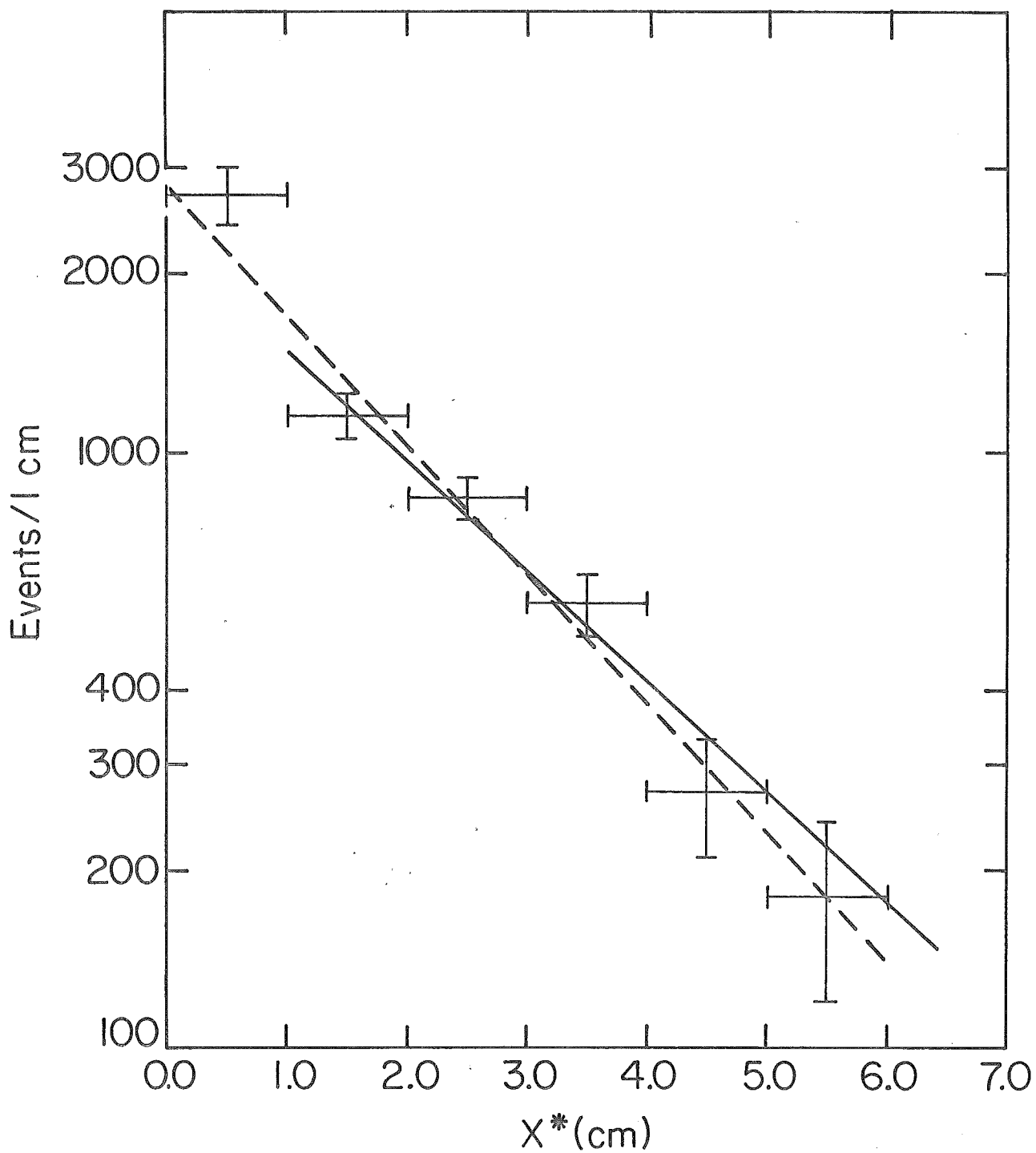


Figure B.8. K_S^0 proper decay length distribution.
Dashed line: fit to all points. Solid line: fit for $x^* > 1$ cm. See text for discussion.

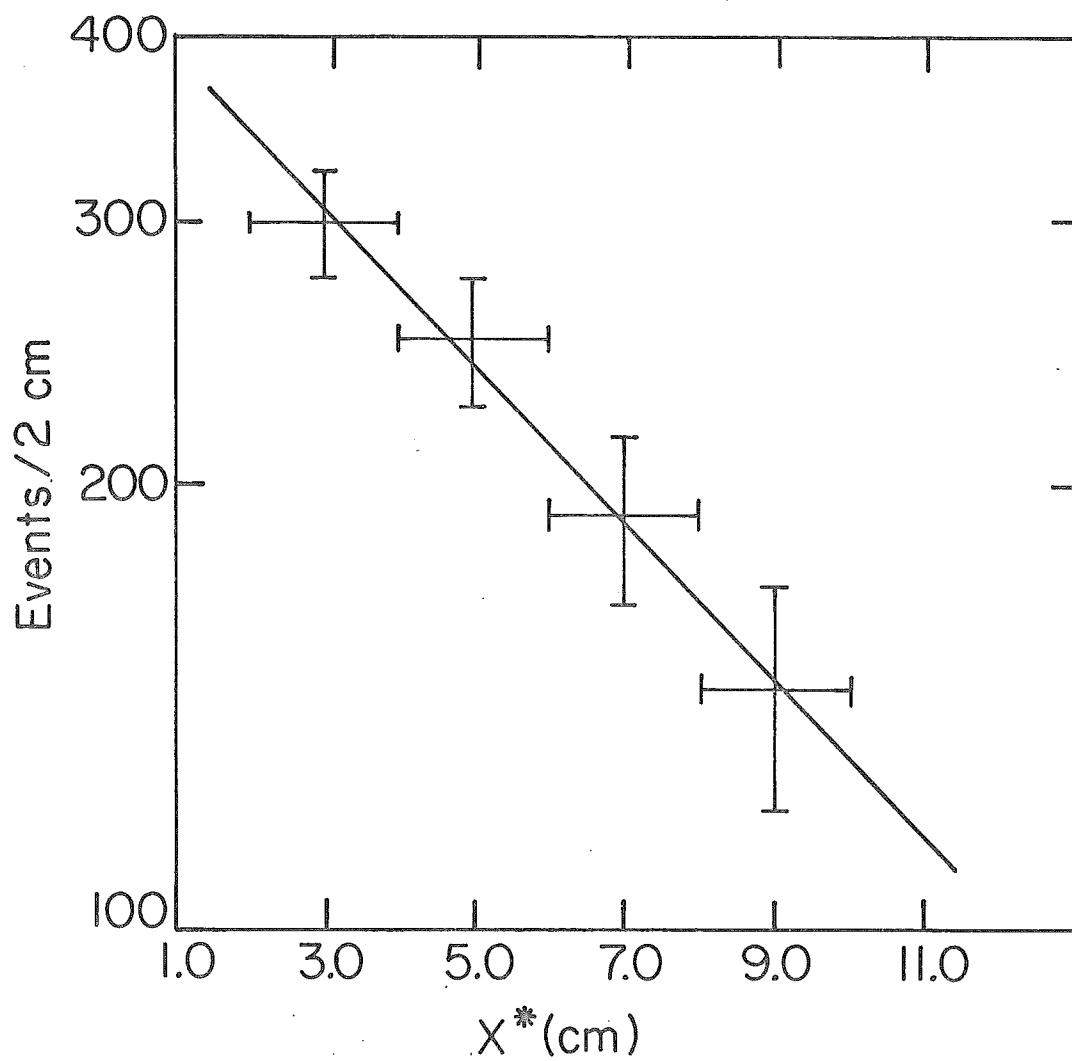


Figure B.9. Λ proper decay length distribution.

The PDG gives $x_0^*(K_S^0) = 2.675\text{cm}$, compared to our value of $2.00 \pm 0.15\text{ cm}$. A better fit to the data (χ^2/DOF of 3.2/3 as compared to 9.5/4) was obtained by restricting the fit to the region $x^* > 1\text{cm}$. This gives $x_0^*(K_S^0) = 2.35 \pm 0.25\text{ cm}$, in much better agreement with the accepted value. This improvement suggests some residual contamination of the K_S^0 sample.

The mean decay length for the Λ (PDG) is 7.89cm. We find $x_0^*(\Lambda) = 8.2 \pm 1.8\text{ cm}$.

APPENDIX C
THE CHARGED-KAON TRIGGER

The main trigger for this experiment was the dimuon trigger described in chapter 2. In order to search for potentially interesting $K^+ K^-$ states, an additional trigger (charged-K) was implemented. Unfortunately, because of the limited running time available, only 140 000 events were taken in this mode. Results on $\phi \Rightarrow K^+ K^-$ from this data sample are given in chapter 5. We concentrate here on the design of the trigger itself.

As discussed in appendix A, the utility of Cherenkov radiation for π -K discrimination arises from its threshold property, that is, the existence of a momentum band in which pions radiate but kaons do not. Thus, the K identification algorithm used in chapter 5 looks for tracks in the 8-21 GeV/c range with no associated Cherenkov light.

For the purposes of an event trigger, however, this procedure could not be used, since no on-line track reconstruction was performed. Thus we are left with the problem of using the signals from the hardware directly to select events containing a $K^+ K^-$ pair.

Figure 2.4 shows the relative placement of the Cherenkov counter mirrors and the elements of the H hodoscope. The H counters completely subtended the twelve central Cherenkov cells. In this way the basic "kaon" signature was produced-- a hit in one of the three H counters behind a given cell, coincident with no light in that cell. The counters covering the cell boundaries were not included, to avoid the necessity of considering light sharing between adjacent mirrors at the trigger stage.

Since a slow pion would also trigger as a kaon, a crude momentum selection was performed by limiting the trigger to the eight central Cherenkov cells. This decision was made on the basis of E154 30" bubble chamber data ($147 \text{ GeV}/c \pi^- p$) (Cooper, 1979), from which it was found that for the spatial region covered by these cells the slow ($< 8 \text{ GeV}/c$) pion / fast pion ratio was $< 10\%$.

Finally, the trigger was completed by requiring kaon hits in the four cells on both sides of the beam gap, to ensure that the two kaons were of opposite sign. Figure C.1 shows the logic for the charged-K trigger.

Like its cousin the dimuon trigger, the charged-K trigger was an imperfect selector of events. The fraction of events containing a fully reconstructible $K^+ K^-$ pair was 4.7%. In contrast, the UHI (minimum bias) trigger data was found to have $K^+ K^-$ pairs in only

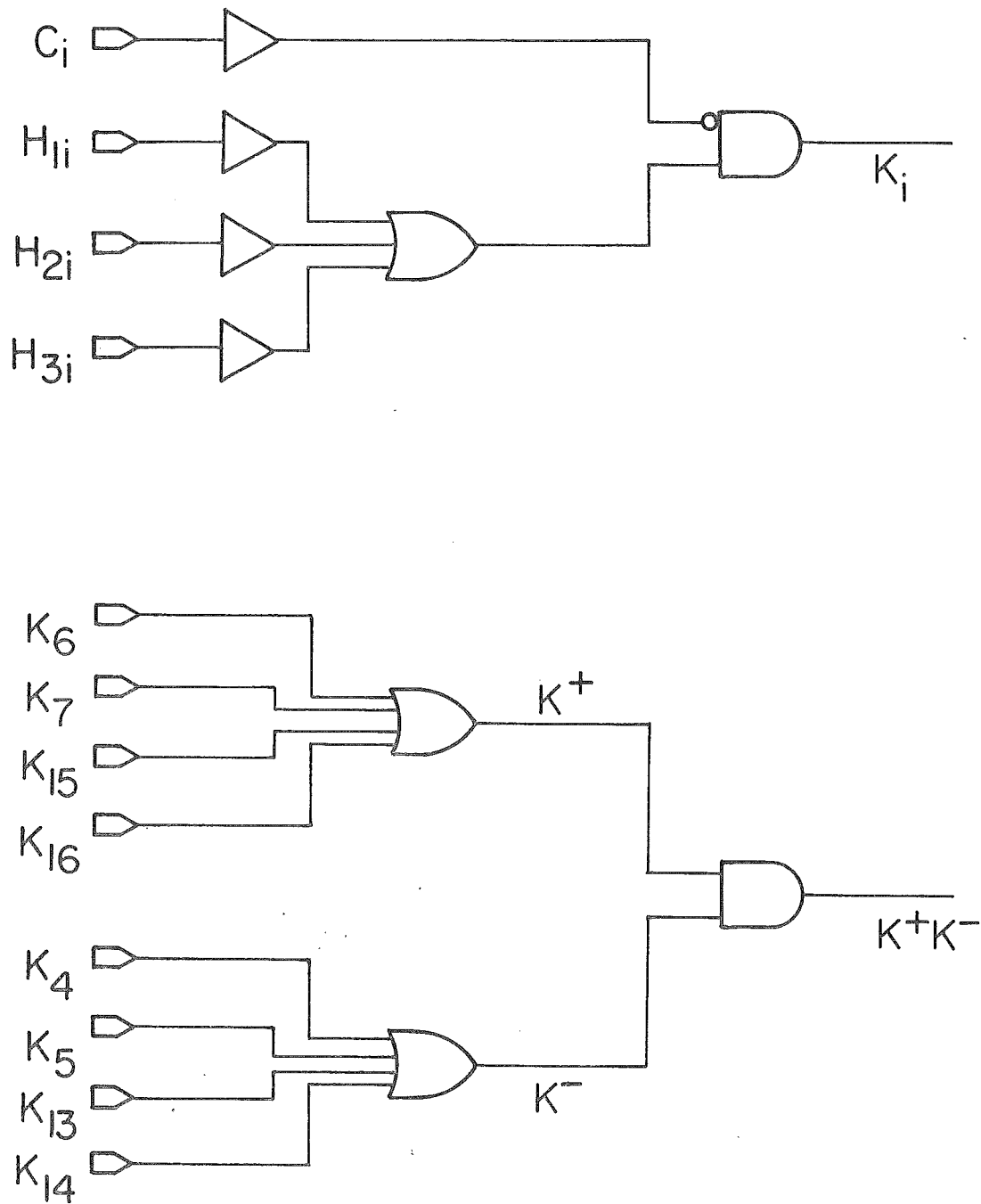


Figure C.1. Charged-K trigger logic. (a) Formation of the single kaon signature K_i for cell i . (b) Formation of the $K^+ K^-$ signature from the K_i .

1.5% of the events. Thus, the $K^+ K^-$ detection rate was enhanced in the charged-K trigger data by a factor of 3.1 over the rate from the pure interaction trigger sample.

APPENDIX D

 ρ^0 - ω INTERFERENCE

The ρ^0 as well as the ω decays into $\mu^+\mu^-$. Because of the proximity in masses, some interference between the two would be expected. The large background and rapidly varying mass acceptance (figures 5.1 and 5.9) in the low mass region precluded the observation of a ρ^0 peak in this experiment. Thus, the relative sizes and shapes of the ρ^0 and ω peaks could not be used to measure the phase of the interference, and hence the contribution of an interference term to the area of the ω peak. Instead of this approach, we have calculated the maximum possible effect of ρ^0 - ω interference on the observed yield.

The amplitude for producing a dimuon pair of mass m from the process $q\bar{q} \Rightarrow V \Rightarrow \mu^+\mu^-$ ($V = \rho^0, \omega$) was taken as a simple Breit-Wigner

$$T_V = \frac{1}{2} \frac{g_\rho^V g_{\mu\mu}^V}{m_V - m - i\Gamma_V/2}$$

(This is the so-called s -channel resonance picture (Perl, 1977).) Here g_ρ^V is a coupling constant characteristic of the production

vertex. We assumed $g_\rho^e = g_\rho^\omega$, in accord with the observation of equal hadronic production of ρ^0 and ω (Kirk, 1977). $g_{\mu\mu}^V$ is the coupling constant at the decay vertex of V , and is thus proportional to $\sqrt{\Gamma_{\mu\mu}^V}$, where $\Gamma_{\mu\mu}^V$ is the partial width of $V \Rightarrow \mu^+\mu^-$. Since this has not been measured for $V = \omega$, we make the further assumption (section 5.5) that $\Gamma_{\mu\mu}^V = \Gamma_{ee}^V$, consistent with $e-\mu$ universality. (The possible discrepancy is discussed in PDG, footnote d, p. 14.) m_V is the mass of V , and Γ_V its total width.

The probability of producing a dimuon pair of mass m is then

$$\begin{aligned}
 |T_\omega + e^{i\varphi} T_\rho|^2 &\sim \left| \frac{1}{2} \frac{\sqrt{\Gamma_{ee}^\omega}}{m_\omega - m - i\Gamma_\omega/2} + e^{i\varphi} \frac{1}{2} \frac{\sqrt{\Gamma_{ee}^\rho}}{m_\rho - m - i\Gamma_\rho/2} \right|^2 \\
 &= \frac{1}{4} \frac{\Gamma_{ee}^\rho}{(m_\rho - m)^2 + (\Gamma_\rho/2)^2} + \frac{1}{4} \frac{\Gamma_{ee}^\omega}{(m_\omega - m)^2 + (\Gamma_\omega/2)^2} \\
 &\quad + \frac{1}{2} \frac{\sqrt{\Gamma_{ee}^\rho} \sqrt{\Gamma_{ee}^\omega}}{\Gamma_{ee}^\rho \Gamma_{ee}^\omega} I(m, \varphi) \\
 &\equiv |T|^2.
 \end{aligned}$$

Here φ is the (unknown) phase of the $\rho^0 - \omega$ interference, and the interference term is

$$\begin{aligned}
 I(m, \varphi) &\equiv \left\{ [(m_\rho - m)(m_\omega - m) + \frac{1}{4} \Gamma_\rho \Gamma_\omega] \cos \varphi \right. \\
 &\quad \left. + \left[\frac{\Gamma_\omega}{2} (m_\rho - m) - \frac{\Gamma_\rho}{2} (m_\omega - m) \right] \sin \varphi \right\} / \left[[(m_\rho - m)^2 + (\Gamma_\rho/2)^2] [(m_\omega - m)^2 + (\Gamma_\omega/2)^2] \right].
 \end{aligned}$$

The cross section for the subprocess $q \bar{q} \Rightarrow V \Rightarrow \mu^+ \mu^-$ is then $\sigma_0(m) = |T|^2/m^2$, where the m^{-2} factor arises from the two-body phase space. (We have ignored constant factors in the above expressions, since we are ultimately interested only in the relative variation in the cross section as a function of the phase.)

We now convert $\sigma_0(m)$, the subprocess cross section, into the cross section for $\pi^- N \Rightarrow V+X$ by integrating $\sigma_0(m)$ over the distribution functions $F^i(x)$ ($\bar{F}^i(x)$) of the quarks (antiquarks) in the incident and target hadrons (Jones and Wyld, 1978). This gives

$$\begin{aligned} \frac{d\sigma}{dm} &\sim \frac{|T|^2}{m} \int_0^1 dx_1 \int_0^1 dx_2 \delta(m^2 - x_1 x_2 s) \\ &\quad \cdot \sum_i [F_{\pi}^i(x_1) \bar{F}_N^i(x_2) + \bar{F}_{\pi}^i(x_1) F_N^i(x_2)] \\ &\equiv \frac{|T|^2}{m} G(m) \end{aligned}$$

Here $G(m)$ is the excitation function, defined as

$$G(m) \equiv \int_{m^2/4}^1 \frac{dx}{x} \sum_i [F_{\pi}^i(x) \bar{F}_N^i(m^2/4x) + \bar{F}_{\pi}^i(x) F_N^i(m^2/4x)].$$

The relative ω yields N_ω as a function of the phase φ are obtained by numerical integration of $d\sigma/dm$ over the range $m_\omega - 3\Gamma_\omega/2.36, m_\omega + 3\Gamma_\omega/2.36$, corresponding to \pm three standard deviations from the ω mass.

We have used the quark distribution functions for the pion and proton as given in Badier (1979) and de Groot (1979) to evaluate $G(m)$. The results obtained here are ultimately insensitive to the $F'(x)$ used, since $G(m)$ varies little over the interval of integration.

Define N_ω^0 as the omega yield in the case of no interference— $I(m, \varphi) = 0$. Figure D.1 is a plot of $N_\omega(\varphi)/N_\omega^0$ vs φ . The worst case effect of the interference would change the true ω yield relative to N_ω^0 by $\pm 37\%$.

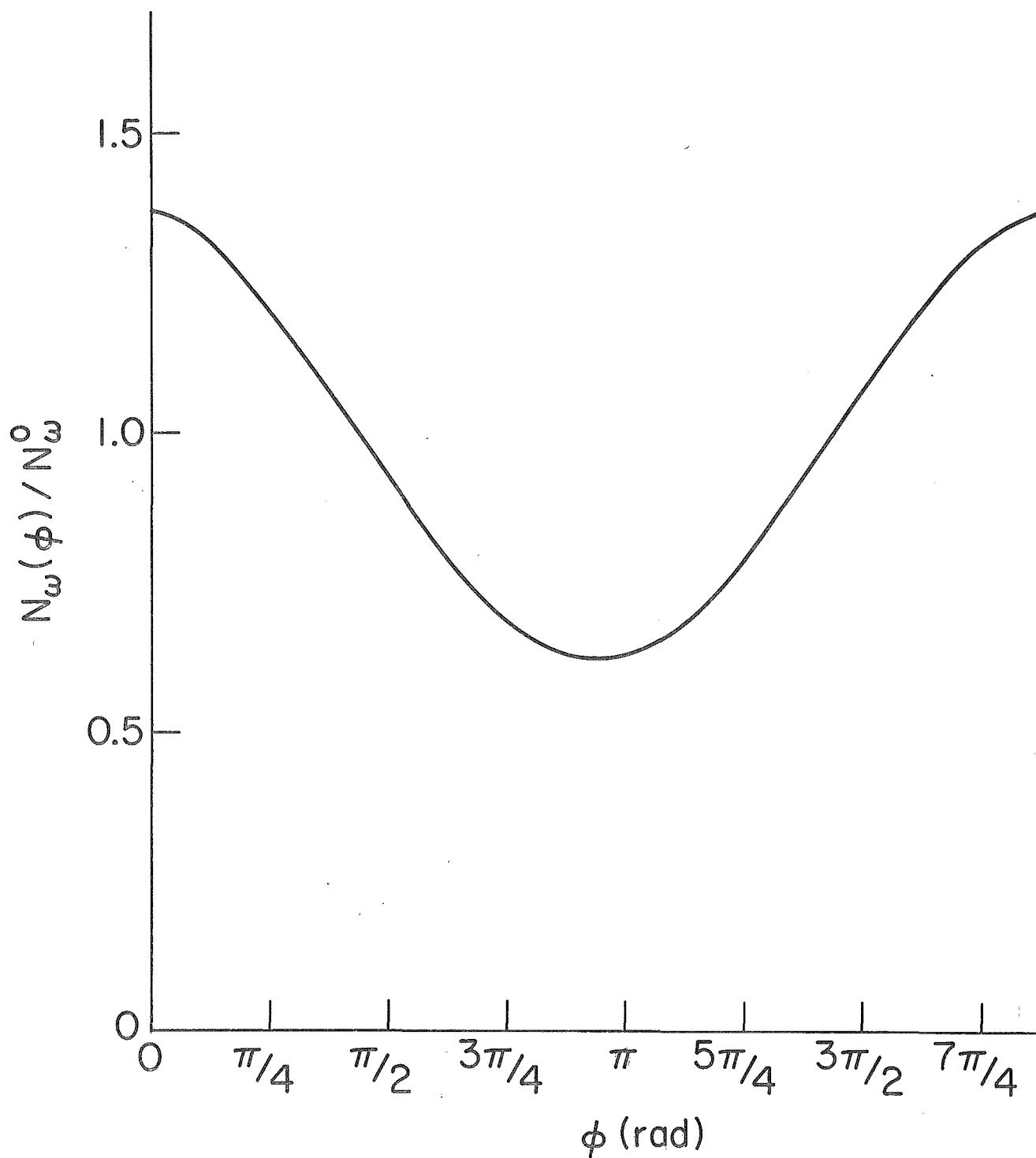


Figure D.1. Effect of $\rho^0 - \omega$ interference on the ω yield as function of the interference phase φ .

REFERENCES

- Abolins, M., et al., Saclay preprint D Ph P E 78-05 (1978)
- Adler, S., Phys. Rev. 177 2426 (1969)
- Allen, J., NRC Preliminary Report 10 (1950)
- Anisovich, V., and Shekhter, V., Nuc. Phys. B55 455 (1973)
- Atac, M., et al., Nucl. Inst. Meth. 140 461 (1977)
- Atac, M., and Urish, J., Nucl. Inst. Meth. 156 163 (1978)
- Avery, P., Thesis, University of Illinois, 1980
- Badier, J., et al., CERN preprint CERN/EP79-67 (1979)
- Bell, J., and Jackiw, R., Nuovo Cim. 51 47 (1969)
- Branson, J., et al., Phys. Rev. Lett. 38 1331 (1978)
- Brick, D., et al., Phys. Rev. D20 2123 (1979)
- Budd, H., Thesis, University of Illinois, 1983
- Cherenkov, P., Dokl. Akad. Nauk SSSR 2 451 (1934)
- Cooper, J., E610 memorandum, June 1979
- de Groot, J., et al., Z. Phys. C1 143 (1979)
- Gell Mann, M., Phys. Lett. 8 214 (1964)
- Gottfried, K., and Jackson, J., Nuovo Cim. 33 309 (1964)
- Hahn, S., Thesis, University of Illinois, 1983
- Hicks, R., Thesis, University of Illinois, 1978
- Hossain, S., Thesis, Tufts University, 1981
- Frank, I., and Tamm I., Dokl. Akad. Nauk SSSR 14 109 (1937)
- Jones, L., and Wyld, H., Phys. Rev. D17 1782 (1978)

- Kirk, H., et al., Nuc. Phys. B128 397 (1977)
- Kirk, T., Fermilab memorandum, December 1978
- Kobayashi, M., and Maskawa, T., Prog. Theor. Phys. 49 652 (1973)
- Lichtenberg, D., Unitary Symmetry and Elementary Particles
second edition, Academic Press, New York, 1978
- Ljung, D., et al., Phys. Rev. D15 3163 (1977)
- Malhotra, P., and Orava, R., Z. Phys. C17 85 (1983)
- Okubo, S., Phys. Rev. D16 2336 (1977)
- Perfection Mica Co., Magnetic Shield Division, Material
and Fabrication Guide, 1976
- Perl, M., High Energy Hadron Physics, J. Wiley and Sons,
New York, 1974
- Proudfoot, J., Thesis, Oxford University, 1978
- Roos, M., et al., Phys. Lett. 111B 9 (1982)
- Sakurai, J., Phys. Rev. Lett. 9 472 (1962)
- Sard, R., and Smith, E., E369 memorandum, June 1978
- Schwitters, R., and Strauch, K., Ann. Rev. Nuc. Sci. 26 89 (1969)
- Shekhter, V., and Shcheglova, L., Sov. J. Nuc. Phys. 29
567 (1978)
- Sixel, P., et al., CERN preprint CERN/EP 82-7 (1982)
- Stroynowski, R., Phys. Rep. 71 1 (1981)
- Van Royen, R., and Weisskopf, V., Nuovo Cim. 50 617 (1967)
- Zweig, G., CERN preprint 8419/TH 412 (1964)

VITA

[REDACTED]

[REDACTED]

[REDACTED], he studied physics at the University of Wisconsin-Milwaukee, graduating with distinction in 1976. A year spent at Rensselaer Polytechnic Institute was followed by his entry into the University of Illinois, where he obtained his M.S. in 1979, and his Ph.D. in 1983. He has held teaching assistantships at all the above-named institutions, as well as a research assistantship at the University of Illinois. He is a member of Phi Beta Kappa and Phi Kappa Phi.